Yang Liu, An Deng, and Mark Jaksa

Three-dimensional discrete-element modeling of geocell-reinforced ballast considering breakage

International Journal of Geomechanics, 2020; 20(4):04020032-1-04020032-21

Three-Dimensional Discrete Element Modeling of Geocell-Reinforced Ballast Considering Breakage

Yang Liu[1*], An Deng[2], Mark Jaksa[3]

[1] School of Civil, Environmental and Mining Engineering, the University of Adelaide, SA 5005, Australia

[*] Corresponding author

Dr. Yang Liu

E-mail: yang.liu03@adelaide.edu.au

Phone: (+61 8) 8313 0591

Facsimile: (+61 8) 8313 4359

[2] School of Civil, Environmental and Mining Engineering, the University of Adelaide, SA 5005, Australia.

Dr. An Deng

Lecture of Geotechnical Engineering

E-mail: an.deng@adelaide.edu.au

[3] School of Civil, Environmental and Mining Engineering, the University of Adelaide, SA 5005, Australia.

Prof. Mark Jaksa

Professor of Geotechnical Engineering

E-mail: mark.jaksa@adelaide.edu.au

ABSTRACT

This paper presents a 3-dimensional discrete element modeling (DEM) study examining the settlement and breakage behavior of geocell-reinforced ballast. The reinforced ballast chamber reproduces the geocell in configuration and the ballast particles in shape and breakage characteristics. The reinforced ballast chamber is subjected to monotonic and cyclic loads. Parametric studies are conducted on the geocell embedment depth and ballast shape. For each case, ballast settlement, geocell responses and ballast breakage behavior are evaluated. This study demonstrates that the geocell can effectively reduce settlement and ballast breakage. The geocell stiffens its embedded layer and reduces stress propagation into the underlying layer.

Keywords: discrete element; railway ballast; geocell; breakage; cyclic loading.

Introduction

Railways are an essential element of modern transport infrastructure. In traditional railroads, ballast, a coarse and angular material, is placed beneath the sleepers to provide rapid drainage and effectively distribute track loads to the underlying subgrade. However, the track drainage condition, bearing capacity and settlement characteristics are often diminished by ballast fouling (Huang et al., 2009, Indraratna et al., 2014). Over time, the track bed becomes deformed and inadequate, particularly for freight transportation. Ballast fouling results from a range of sources, as shown in Fig. 1, where it is clear that ballast breakdown is by far the greatest contributor to the deterioration of the rail track condition. Therefore, it is of paramount importance to study the breakage behavior of ballast and develop solutions to minimize ballast degradation.

Many studies have been conducted to investigate ballast breakage and its influence on the mechanical response of ballast. Discrete element modeling (DEM) was often used in the studies (Lobo-Guerrero and Vallejo, 2006, Hossain *et al.*, 2007, Indraratna *et al.*, 2009, Lu and McDowell, 2010, Yan *et al.*, 2014, Wang *et al.*, 2017). Yan *et al.* (2014) and Wang *et al.* (2017) employed 3-dimensional (3D) DEM to study the breakage mechanism of a single ballast stone under uniaxial compressive loading. Lu and McDowell (2010) also adopted 3D DEM to simulate breakable ballast by attaching small particles to unbreakable clumps and subjected the ballast assembly to monotonic and cyclic loads under triaxial condition. Particles created in these studies account for the angularity and size of the ballast particles and successfully simulated ballast breakage. To verify the simulation results, laboratory tests on ballast breakage were conducted (Huang *et al.*, 2009, Indraratna *et al.*, 2010, Sun and Zheng, 2017). Sun and Zheng (2017) used triaxial tests to study the effect of particle sizes on ballast breakage behavior. Indraratna *et al.* (2010) used both experimentation and 2D DEM, with simplified ballast shapes formed using 6 to 20 particles, to study the breakage mechanism under biaxial conditions.

To stabilize railway ballast, studies have been conducted to reinforce ballast using geosynthetics (Chen *et al.*, 2012, 2013, Leshchinsky and Ling, 2013, Ngo *et al.*, 2014, Qian *et al.*, 2015, Wang *et al.*, 2016). Chen *et al.* (2012) used DEM to simulate the response of geogrid-reinforced ballast under confined and unconfined conditions. Similarly, Qian *et al.* (2015) used DEM to examine geogrid-reinforced ballast subjected to triaxial tests, whereas Liu *et al.* (2018) modeled a scaled-down geocell-reinforced railway track structure using DEM. However, these studies made no account of ballast breakage, which is an appropriate assumption when considering the change in performance of geosynthetic-reinforced ballast under short-term, low-stress loading conditions. Where more complex loading conditions are considered, ballast breakage should be accounted for.

DEM, a modeling method developed by Cundall and Strack (1979), possesses the capability to represent, with appropriate engineering accuracy, distinct ballast particles and to simulate particle motion. The method is able to replicate variable angularities of the ballast, and similarly reflects variable material micro-properties, such as stiffness and friction (Itasca, 2009, Chen *et al.*, 2012, Irazábal *et al.*, 2017). More importantly, it enables 3D modeling. This is particularly important for the accurate simulation of a 3D geocell panel, as 2D modeling neglects, or at least simplifies, the interaction between cells and so underestimates the performance of the geocell panel.

A geocell is a cellular confinement system, of honey-comb shape, that is commonly fabricated using high-density polyethylene (HDPE) sheets. It is manufactured into various sizes and depths to accommodate different applications. Geocells have been widely used in a variety of infrastructure applications, such as foundations and subbases (Dash, 2012, Yang *et al.*, 2012, Dash and Bora, 2013, Tanyu *et al.*, 2013, Hegde and Sitharam, 2015, Moghaddas Tafreshi, 2015, Oliaei, 2017), slopes (Mehdipour *et al.*, 2013), retaining structures (Chen *et al.*, 2013) and embankments (Madhavi Latha and Rajagopal, 2007, Zhang *et al.*, 2010). All of these studies have shown that using geocells improves the performance of the infrastructure by reinforcing the granular infill materials. Leshchinsky and Ling (2013) used simplified, regular quadrilaterals to model the shape of the geocell in finite element analysis to simulate geocell-reinforced ballast. Liu *et al.* (2018) employed a similar geocell geometry in DEM to simulate straight and curved ballast railway tracks. The simplified geocell model reduced computational effort, without compromising the accuracy of modeling the geocell behavior and its interaction with the infill material. Hegde and Sitharam (2015) and Yang *et al.* (2010) used realistic geocell profiles in the FLAC3D finite element method (FEM) software to demonstrate the benefit of geocell-reinforced sand beds. However, given the continuum nature of the FEM approach, it is likely not to be as applicable to ballast as it is to sands.

The present study utilizes the 3D DEM software PFC3D 5.0 to examine the performance of geocell-reinforced railway ballast, where ballast breakage is considered. A model is developed which involves a single geocell pocket of realistic shape, embedded within a chamber filled with ballast. The size of the model is selected to reproduce a unit of the reinforced railway ballast track bed. Relevant loading scenarios are developed and examined, with a focus on the occurrence of ballast breakage and its effect on ballast performance. Comparisons are made between unreinforced and reinforced cases and the geocell layer depth is examined to optimize track bed design. With awareness of presence of fines arising from ballast abrasion and other external sources, and its adverse effects (e.g., the poor drainage conditions) on load-carry capacity of track bed, this study focuses on the ballast breaking apart into relatively larger pieces, resulting impact, and the solution of geocell mitigating the breakage. This helps avoid excessive computational expenses of DEM simulating the assemblage of fines and therefore maximize simulation efficiency.

Discrete Element Modeling

Contact Model

Discrete element modeling incorporates a contact model to govern the interactions of objects in contact. There are four types of objects available in PFC 3D including: a ball, a wall, a clump and a cluster. The ball and wall objects are the fundamental building blocks. A group of balls can be aggregated either into a clump, if the inter-ball contact in the clump is unbreakable, or a cluster, if the contact is breakable. The cluster allows for the simulation of particle breakage and is used in this study for ballast modeling.

The current study employs two contact models: linear contact and linear parallel-bond contact. The linear contact model is used for cluster-to-wall contacts and inter-cluster contacts, whereas the parallel-bond contact model is used for contacts within the geocell and those within a cluster. Schematic diagrams of the two contact models are provided in Fig. 3. The linear contact model, a combination of linear and dashpot components, allows relative rotation and slip and can only transmit compressive forces over an extremely small contact point. The linear components provide the linear elastic behavior, while the dashpot provides viscous behavior. The linear forces are produced by the constant normal (k_n) and shear (k_s) stiffnesses of the two contacting objects, while the dashpot forces are defined and developed by the normal (β_n) and shear (β_s) damping ratios. Slip between the two contacting objects is controlled by the friction coefficient (μ) and the activity and loss of linear contact is governed by a surface gap (g_s). As one might expect, contact is active when the surface gap is less than or equal to zero.

The linear parallel-bond contact model was developed by Potyondy and Cundall (2004). It has been widely used to model a range of geomaterials, for example, sand, aggregates and geosynthetic materials (Wang and Leung, 2008, Chen *et al.*, 2013, Liu *et al.*, 2015, Xu *et al.*, 2017, Liu *et al.*, 2018). As shown in Fig. 3(b), a parallel bond is the combination of two interfaces, a linear interface, which is equivalent to the linear contact model, and a parallel-bond interface that acts in parallel to the linear interface. The parallel-bond interface is distributed over a circular cross-section lying on the contact plane and centered at the contact point. It can transmit both forces and moments, which means it can resist relative rotation until the imposed load exceeds its limiting strength. The bond strength is defined by multiple input parameters, including the normal ($\bar{k}_n$) and shear ($\bar{k}_s$) stiffnesses, tensile strength ($\bar{\sigma}_c$), cohesion ($\bar{c}$) and friction angle ($\bar{\varphi}$). As with the linear contact model, the linear parallel-bond contact model is active when the surface gap (g_s) is less than or equal to zero. As stated by Cundall (2001), a calibration stage is necessary for acquiring all input micro-parameters, which commonly involves a trial-and-error process.

Materials

Ballast

Railway ballast is usually produced by blasting and/or fragmenting a rock mass, and hence exhibits variable angularities. Past studies (Lim and McDowell, 2005, Lu and McDowell, 2006, Lu and McDowell, 2008, Yan *et al.*, 2014, Liu *et al.*, 2018) have demonstrated the importance of accurately modeling the particle angularities and suggested that modeling angularities in simulations better reproduces the actual behavior of the ballast. In order to do so, ballast is often simulated using clumps. However, a clump is a 'slaved' group of spheres which behaves as a rigid body. This implies that the contacts within a clump are fixed and the clump does not deform or break under loading. Whereas, clusters are more suitable for modeling particle breakage as they incorporate parallel-bonds for the spheres within the cluster. As shown in Fig. 3(b), the bond is breakable when the imposed load exceeds the bond strength. Similar to clumps, clusters aggregate spherical particles into an overall form that resembles angular shapes or blocks. These clusters can interact with each other and approximate the behavior of an angular, blocky system (Group, 2008).

The ballast clusters are generated in a manner similar to that adopted for ballast clumps (Liu *et al.*, 2018), with an additional step of bonding all spheres within a clump by parallel-bonds. Initially, clump templates are defined corresponding to the shapes of actual ballast. Four shapes were selected from a stockpile of ballast in South Australia to represent typical ballast geometries, as shown in Fig. 2. The ballast more or less falls into one of the shapes. The fours shapes agree in appearance with those used in Tutumluer *et al.* (2013) but were simulated in a different approach. These selected shapes were modeled in 3D using CAD software and then imported into PFC. Based on these imported 3D models, PFC generates corresponding clump templates in accordance with the method introduced by Taghavi (2011). The parameters control the fidelity/smoothness of the clump by means of the 'distance' and 'ratio' user-defined parameters. The 'distance' corresponds to an angular measure of smoothness and expressed in degrees, as described by Taghavi (2011). The greater the 'distance', the smoother the clump and the greater the number of particles that are incorporated in a template. The 'ratio' controls the size difference between the largest and smallest particles. In the present study, a ratio of 1:5 is selected in order to reflect realistic ballast shapes in PFC, while optimizing computational effort. It should be noted that varying the clump size has no effect on the number of particles within a clump template; the spheres automatically adjust their diameters to suit the pre-defined ratio and clump sizes. Once the clump templates were created, and clumps were generated within a defined boundary, a bespoke code was executed to replace the group of particles in each clump with parallel-bonded spheres to form clusters. These clusters were then calibrated. It should be noted that the inter-sphere overlaps generated internal forces due to the non-zero linear stiffnesses of two bonded-spheres. The internal forces however contribute to the parallel-bond strengths and do not influence the targeted initial conditions.

The ballast gradation follows the Grade 60 particle size distribution (PSD) requirement specified by Australian Standard (Australia, 2015) and ARTC (2007). The gradation curves and the standard specification are shown in Fig. 4. This study adopts a PSD that is closer to the lower boundary of the specification in order to optimize the number of ballast particles generated in the DEM model. Over the PSD range of 25 to 58 mm, the four shapes of ballast are distributed evenly, and are allocated in equal proportions, 25% each, in an assembly.

Geocell

A realistic form of a single geocell pocket was again created using 3D CAD software and then imported into PFC3D as a surface description. The surface description has identical geometric properties as a commercially available geocell pocket, as shown in Fig. 5(a). The curved surface of the geocell is an improvement on the flat surface adopted by Liu *et al.* (2018) and thus increases the accuracy of geocell modeling. The geocell pocket measures 255 (W) × 375 (L) × 100 (D) mm, with a cell-wall thickness of 2.1 mm, and 4 mm at the junctions. It should be noted that the surface description provides an additional cell-wall thickness of 0.1 mm to assist with reducing the contact forces between the particles and the geocell walls. The implementation of a single geocell pocket optimizes computational effort, whilst also facilitating a more complex numerical model at the micro level, which enhances the accuracy of the simulation. For example, the ballast elements are composed of a greater number of spheres to present more realistic ballast particles and, similarly, the geocell model no longer requires simplification to reduce computational effort, as has been undertaken in previous studies (Ngo *et al.*, 2015, Liu *et al.*, 2018). This leads to more accurate simulation of the mechanical behavior and ballast breakage in particular. However, Chen *et al.* (2013) suggested that the use of a single geocell pocket may result in reduced soil strength when compared against soil reinforced with geocells incorporating multiple pockets. To mitigate this effect, the geocell model adopts the minimum dimensions of a commercially available geocell product, which improves the infill strength (Chen *et al.*, 2013). Additionally, the single geocell pocket is used for the purposes of the present study, which primarily seeks to examine whether geocell can effectively alleviate ballast breakage. We also used perforation-free walls, provided that no drainage was considered. The influence on settlement or breakage should be less significant, as the perforated areas are relatively less and the holes are small. Fig. 5(c) illustrates the geocell pocket embedded in the ballast chamber.

Once the surface description of geocell is imported to PFC, 2 mm diameter spheres, with an initial porosity of 0.28, are distributed in 2 equal layers (50 mm each) on the 100 mm high cell-wall. The second layer is not generated until the first layer is cycled to equilibrium state. It should be noted that the particle generation process creates overlap among the spheres. The overlaps are eliminated by cycling the system to an initial equilibrium, which is assessed by the average mechanical solve ratio. The ratio is defined as the unbalanced force divided by the average value of the sum of the contact, body and applied forces over all of the particles. When the ratio is sufficiently small (e.g. 1 x 10^{-3}), equilibrium is attained. The spheres that are located outside of the boundary of interest are then deleted and the porosity is recalculated to ensure no large gaps exist between the spheres. A total of 31,551 spheres are used to develop the geocell pocket, with a final porosity of 0.001. The final porosity reflects the spheres rearrangement and the optimized sphere-to-sphere connections. The geocell pocket generated in PFC is shown in Fig. 5(c). Finally, the surface description and boundary wall are deleted, and all sphere-to-sphere contacts are assigned with linear parallel-bonds and the calibrated micro-properties.

Material Calibration

Ballast

The behavior of ballast is calibrated against two tests: unconfined compressive strength (UCS) test and point load strength (PLS) test.

UCS test

The UCS tests were conducted on three specimens collected from the ballast stockpile area in South Australia. The specimens were trimmed into cuboids of 15 (W) × 15 (L) × 30 (H) mm to achieve a 2:1 height-to-width ratio. It should be noted that the largest ballast samples are selected for the UCS test in order to produce effectively identical and intact specimens, and to minimize size effects.

As reported by Zhang *et al.* (2011), the reduced sample size results in a significant increase in the UCS. The specimens were placed at the center of the compressive loading device and two sets of linear-variable differential transformers (LVDTs) were installed on the right- and left-hand sides of the specimen, as illustrated in Fig. 6(a). The compression machine applies a loading rate of 50 N/s until failure occurs.

The UCS test was simulated by compressing the same-sized specimen using two walls, as shown in Fig. 7. The specimen was generated by using the same procedures and parameters (i.e. size ratio and smoothness index) as for the ballast clusters. A total of 1,655 spheres were used to generate the specimen. The greater number of spheres enables the use of smaller spheres and the flat surface of specimen prism. The spheres and clusters are equipped with either a linear contact or linear parallel-bond model, depending on the locations of concern. As with similar studies relating to ballast calibration (Lim and McDowell, 2005, Li and McDowell, 2018, Liu *et al.*, 2018), the iterative approach was used to determine the model micro-properties. The initial values were determined from those of similar materials examined in past studies (Lu and McDowell, 2010, Ngo *et al.*, 2017, Liu *et al.*, 2018). Using the micro-properties provided in Table 1, excellent agreement is obtained between the test and simulation results in regards to the stress–strain relationship, as shown in Fig. 7(b). As can be seen, the test and simulation results exhibit linear stress–strain behavior where the average elasticity, peak strength and corresponding strain largely agree. The test results exhibit a slight strain-hardening process which may be caused by micro-cracks within the ballast specimen closing up under loading. Whereas, these micro-cracks are not reproducible in the simulation due to the limited number of spheres and the homogenous parallel-bond strengths among a bonded assembly. It is noteworthy that micro-property normal stiffness is expressed as deformability to the center-to-center distance of spheres. From this expression, the sphere stiffness is dependent on the sphere sizes.

PLS test

In addition to the UCS test, the PLS test was carried out in order to validate the micro-properties obtained for the clusters. The test was conducted on three ballast specimens that match the surface characteristics of ballast templates 1, 2 and 3 in Fig. 2. The ballast specimens were randomly selected from the same stockpile as those used in the UCS test. Fig. 8(a) shows the hydraulic point load tester used to conduct the PLS tests. The loading was applied manually, with the load measured by the tester and displayed on its gauge. The machine stops measuring once it detects material failure. The PLS results of the three specimens are 1,284, 1,271 and 1,213 kPa. For the simulation, the ballast clusters (Templates 1, 2 and 3) are created using a similar process to that for cluster templates. The cluster diameters are equivalent to their laboratory counterparts, i.e. 51 mm (Template 1), 48 mm (Template 2) and 47 mm (Template 3). The simulation loading setup uses a cone for the upper loading platen and a disc for the base. The disc provides stability to the ballast during the initialization phase. Once the upper cone is in contact with the cluster, the disc base is removed and replaced with a cone that is identical to the upper platen, as shown in Fig. 8(b). Loading is achieved by displacing the upper cone at a strain rate of 0.1% per second and the ballast cluster is assigned the micro-parameters previously given in Table 1. The stresses imposed on the parallel-bonds are recorded when the bonds break. The three cluster templates yield PLS values of 1,199, 1,217 and 1,268 kPa. These values agree well with the test results, which validates the micro-properties obtained from the UCS test.

Geocell

The calibrations of geocell cell-wall and junction were carried out using the uniaxial tensile strength (UTS) and seam strength (SS) tests, respectively. The cell-wall specimen was trimmed from a perforation free area of the cell-wall and prepared in accordance with (ASTM (2004)). Its thickness was 2 mm and gauge length 107 mm. The narrow section, where elongation occurs, was 13 mm in width. The junction specimen was 4 mm thick, with an overall length of 75.5 mm and a width of 25 mm. The gauge length was 30 mm, which is the minimum distance that can be achieved due to the rigidity of the HDPE.

For the laboratory tests, an Instron tensile machine is used and the test setup is similar for both the cell-wall and the junction. Schematic drawings of the prepared specimens and testing schemes are shown in Fig. 8. The cell-wall and junction specimens are clamped at both ends, with a 30 mm and 40 mm gripping area at each end, respectively. The loading ranges of the Instron machine were set to 1,000 N in order to achieve the optimal resolution. Once the specimen is clamped in place, the tensile force is applied by the displacement-controlled mechanism, at a rate of 50 mm/min (ASTM, 2004). The elongation process continued until failure of the specimen occurred.

The DEM simulation of the cell-wall UTS test involves generating the cell-wall and junction specimen from pre-defined surface descriptions, assigning parallel-bonds to the specimens, and applying the tensile load by translating the upper gripping spheres. As with the models developed for ballast and geocell pocket, the material outlines were drawn in CAD software and then imported into PFC to scale. The surface descriptions have dimensions identical to the specimens used in the laboratory tests [Fig. 9(a) and (c)]. This step is followed by distributing 2 mm diameter spheres within the pre-defined surface descriptions. It should be noted that only the gauge sections of the cell-wall and junction specimens are generated in the DEM. An additional layer of spheres with the same diameter is generated at the top and bottom to act as gripping (red) and loading (green) spheres, as shown in Fig. 10, resulting in an overall height of 108 mm. For the junction SS test, the cell-wall region of the specimen is neglected in the simulation to eliminate possible elongation of the cell-wall. The specimen is generated within a box that is 25 mm in length and 10.5 mm in width, which shares identical dimensions to that of the geocell junction. The box has a height of 8 mm, which is equivalent to the thickness of a geocell junction (4 mm) plus two x 2 mm thick layers of gripping and loading spheres. All parameters used in the sphere generation process are identical to those used in the geocell model generation in order to replicate trimmed cell-wall and junction strips.

Subsequent to the sphere generation process, the cell-wall and junction models are cycled to their initial equilibrium. Once equilibrium is reached within the cell-wall and junction models, parallel-bonds are assigned to the cell-wall and junction models at sphere-to-sphere contacts, with separate sets of micro-properties as specified in Table 2. Lastly, the gripping spheres located at the bottom are prohibited from both rotation and displacement. The remaining spheres, including the loading spheres and those forming the specimens are prohibited only from rotation. Loading, in both the UTS and SS tests, is achieved by displacing the loading spheres at a rate of 50 mm/s, which matches the loading rate used in the laboratory experimentation.

The stress–strain relationships of the calibrated cell-wall and junction models, as well as their laboratory counterparts, are shown in Fig. 11. Very close agreement is obtained between the simulation and test results with respect to the peak strengths. For the cell-wall model, the simulation yielded a peak tensile strength of 10.14 MPa at an axial strain of 17.60%, while the laboratory test yielded 10.16 MPa at 17.64% axial strain. For the junction model, a peak seam strength of 2.06 MPa was achieved at 52.38% axial strain in the simulation, while the laboratory test yielded 2.05 MPa at the same axial strain value. There are, nevertheless, discrepancies between the elastic regions in both simulations; the simulations exhibited linear behavior while the laboratory counterparts experienced different levels of strain-hardening or softening. This is due to the linear nature of the parallel-bonds implemented in the simulation. Previous work (Liu *et al.*, 2018) obtained a similar outcome in the elastic region, when conducting UTS test in PFC on the cell-wall. This is considered a limitation in the currently available built-in contact models. This limitation can reduce or enhance the tensile strength of the geocell model when compared to actual geocells, resulting in variations in the confinement level.

Ballast Chamber Model

A full-scale railway structure simulation is computationally intensive and extremely time-consuming, owing to the large number of spheres needed to simulate the geocell and ballast infills (Liu *et al.*, 2018). Unfortunately, full-scale modeling is beyond current and available computer capability, including supercomputers. Liu *et al.* (2018) downscaled the model to suit the computer capability. This downscaling solution, however, may likely underestimate performance of geocell-reinforced embankments due to the use of a smaller volume of ballast used in the simulation. To minimize the influence of downscaling and to account for the available computer capability, an alternative solution is to adopt a ballast-filled chamber which is representative of the below-sleeper section. A similar approach has been adopted in previous studies (Chen *et al.*, 2012, Li and McDowell, 2018), which have proven to be successful in examining the performance of ballast embankments and optimizing computational effort. The geometry of the ballast chamber is given in Fig. 12. The chamber is 450 mm in the longitudinal direction of a railway and 350 mm in cross-sectional width that can accommodate a single geocell pocket. It has a nominal ballast depth (below-sleeper) of 300 mm, which is the same as actual railways, as per ARTC (2012). The boundary effect is mitigated through assigning identical linear contact parameters to both the cluster-to-cluster and cluster-to-wall contacts.

For the geocell-reinforced model, a parametric study is conducted on the effect of geocell embedment depth, *D*, on the breakage behavior of the ballast. As shown in Fig. 12 (a), three embedment depths are examined: D_1 =100 mm, D_2 = 200 mm and D_3 =300 mm, using the upper surface of the chamber as the reference point. As shown in Fig. 12(b), the geocell pocket is placed in line with the rail track, 37 mm longitudinally and 47.5 mm transversely from the chamber walls and, to mitigate boundary effects, the chamber walls are assigned the same linear stiffness and frictional coefficient as those for the ballast. The sleeper uses the same parameters as for the loading wall in the ballast calibration process, which creates consistent stress–strain behavior. The sleeper is 250 mm wide, which is consistent with the base width of heavy-duty prestressed concrete sleepers, as per specified by ARTC (2017). In this study, the sleeper coincides with the centre of geocell, avoiding acting directly above the junction. This helps examine the full capacity of the reinforced chamber.

The ballast chamber models are shown in Fig. 13. Four ballast chamber models are developed: one unreinforced and three reinforced, depending on the geocell embedment depth. The four models are numbered Tests 1 to 4, respectively. For the unreinforced model, the ballast infills were generated at an initial porosity of 0.4. The ballast assembly was cycled to equilibrium, resulting in a porosity of 0.46. The porosity was measured using six evenly distributed measurement spheres (300 mm in diameter), as suggested by Wang *et al.* (2018). For the reinforced models, the ballast infills were generated alternating with the geocell pocket. For example, when the geocell pocket is embedded at D_2 =100 mm, the bottom 100 mm of ballast is generated first and cycled to equilibrium. The geocell pocket is then placed on the bottom ballast layer. The remaining 200 mm thick ballast layer is generated above the geocell pocket and allowed to fall into the pocket under gravity. This approach mimics the placement of ballast in actual geocells and accelerates the dissipation of the internal contact forces. Due to the inclusion of the geocell, the reinforced ballast chamber arrived at slightly greater post-equilibrium porosities than those of the unreinforced model. Once the ballast chamber model was established, the sleeper is generated, and subsequent loading conditions are applied.

Monotonic and Cyclic Loading

Monotonic loading is applied to determine the subsidence of the ballast layer in response to a slowly increasing vertical load and is similar in nature to a plate load test. The sleepers advance at a rate of 0.02 mm/s to cause the ballast layer to settle to the desired strain of 15% (45 mm). This loading scenario provides insight on the responses of the geocell and ballast under an extreme loading condition. The slow loading rate is consistent with that adopted for the compressive strength test in the material calibration stage, which improves the simulation accuracy by allowing sufficient time to calculate the inter-particle contact forces.

Cyclic loading, on the other hand, is of higher significance in regard to the assessment of the long-term serviceability of the ballast. The current study adopts the load distribution method proposed by Sadeghi (2008). He suggested to apply the stress distribution acting on the ballast, as shown in Fig. 14. The contact pressure is at maximum, W_2, under the rail seat position and decreases in stages as W_1, W_3 and W_4 depending on the region of concern. The load calculation model is specified in Table 3. The load relies on several parameters, such as a dynamic coefficient ($Ø$), wheel diameter (D), train velocity (V), sleeper spacing (S) and sleeper length (L_s), that are listed in Table 4. By accounting for the sleeper dimensions used in this study, the contact pressure is calculated as 150 kPa. The cyclic loading is applied with a frequency of 8.25 Hz, which corresponds to a wagon traveling at 60 km/h with an axle load of 25 t (Indraratna *et al.*, 2010).

A total of 20,000 loading cycles were performed for each of the four models. The cycle number doubles the number suggested by Ngo *et al.* (2017), who suggested, based on laboratory observation, that the majority of the ballast deformation and degradation occurs within the initial 10,000 cycles. Therefore, the cycle number adopted in the present study is sufficient to capture the deformation and breakage behavior of ballast. Additionally, the doubled cycle number may shed light on the long-term serviceability and response of the geocell.

Results and Discussion

Monotonic Loading

Settlement

The axial stress versus settlement relationships of all four models are given in Fig. 15. All models exhibited relatively linear behavior when subjected to monotonic loading. The stress–settlement relationships are divided into two zones: *A* and *B*. Zone *A* covers the initial 10 mm of settlement; Zone *B* ranges from 10 mm to 45 mm. In Zone *A*, all models underwent an initial compaction stage reflected by the more rapid settlement rate. Test 1 reached approximately 10 mm under minimal load (i.e. < 50 kPa). Tests 2–4 experienced a similar tendency, whereas the initial compaction stage was completed earlier. The ballast assemblies reached a denser state at 4 mm for Tests 2 and 3, and at 2 mm for Test 4. The differences mainly arise from the different embedment depths of the geocell. The geocell pocket provides more efficient confinement of the ballast when it is placed at a higher, rather than a lower level. This outcome is in agreement with that obtained by Liu *et al.* (2018). The reinforcing layer acts as a stiffened mattress, which provides passive resistance against lateral spreading of the ballast infill, which in turn reduces the load on the sleeper propagating into the underlying foundation material. An approximately 5% reduction in porosity is recorded in all models at the end of their respective compaction stage. From that point onward, the ballast in all test models further stiffens, with an associated decrease in settlement.

In Zone *B*, Tests 1 and 2 noticeably stiffen once the settlement reaches approximately 15 mm. Both of the two models then become stable, while Tests 3 and 4 maintain a slow gain in stiffness as the ballast settles. The normal stiffness, which is defined as the ratio of the applied stress divided by the settlement, is used to assess the performance of each model test, Generally, Test 1 exhibits the poorest load bearing performance, reflected by the lowest average normal stiffness of 19.7 kPa/mm. Slight improvement in the normal stiffness is observed in Tests 2 and 3, with an average of 21.6 and 22.5 kPa/mm, respectively. The stiffness increases by 10% and 14%, respectively. Test 4 yields the best bearing performance, with a normal stiffness of 24.6 kPa/mm or 25% stiffness gain compared to the unreinforced model. The overall behavior of Tests 1 and 2 agrees with those in Liu *et al.* (2018), whose results are also presented in Fig. 15 for comparison. It is shown that the bearing capacity of all of the models in the current study almost doubles the corresponding value reported by Liu *et al.* (2018), where the strain reaches 15%. The chamber conferment may contribute to the gain, but, as aforementioned, Liu *et al.* (2018) scaled down the ballast embankment model and used a lower volume of ballast assemblage, which generally underestimates the ballast bearing capacity. In addition, differences in the ballast gradation and the loading method also play important roles in the observed difference in bearing capacity. However, the current study agrees with the past studies (Leshchinsky and Ling, 2013, Liu *et al.*, 2018), in that suspending a geocell at a higher level yields improved bearing performance.

Investigating the displacement vectors of the ballast particles provides insights on the improved bearing capacity of the geocell-reinforced models. Fig. 16 presents the displacement vectors of the ballast in all of the model tests. For illustration purposes, a clipped region of width 125 mm (i.e. half of the width of the sleeper) is used to extrapolate the displacement vectors of the ballast directly beneath the sleeper. In Test 1 all ballast particles move downward and spread laterally when approaching the base. Compared to Test 1, the reinforced models show noticeable improvement in reducing settlement which is reflected by the displacement vectors. Placing the geocell at the base showed interesting results in terms of ballast movements. Unlike the unreinforced model, the geocell pocket restricts the lateral movement of the ballast. At the center of the geocell pocket, the ballast particles restrict their own lateral movement, forming the pattern highlighted by the arrows. Initially, the ballast particles tend to move laterally to the opposite side as they approach the geocell pocket center from both directions. Consequently, the movement is then deflected by both sides, which results in downward movement. In addition, the geocell pocket also reduces the movement of the surrounding ballast. This enhancement is visualized in Test 3. When compared with the unreinforced model at an identical depth, the vertical displacements of the ballast particles are significantly reduced. Furthermore, Tests 3 and 4 further validate the load-settlement responses presented in Fig. 15 and the reinforcing mechanism of the geocell at a micro-mechanical level. In the geocell-embedded layers and the underlying ballast, settlement reductions are evident when the geocell pocket is placed 100 and 200 mm above the base.

Ballast Breakage Characteristics

Fig. 17 shows the number of ballast particle breakages versus settlement relationships of all model tests. As expected, Test 1 experienced the greatest number of breakages, whereas the lowest number is recorded in Test 2, where the geocell is placed at the base. Although Tests 3 and 4 exhibit superior bearing performance than Test 2 in the monotonic loading condition, Test 2 outperforms Tests 3 and 4 in reducing ballast breakage. To better understand the breakage behavior in unreinforced and reinforced test models, detailed analyses are conducted in relation to ballast shape, location distribution and failure strength.

Table 5 presents the breakage and failure strength results with respect to the ballast layers where the chamber is subjected to monotonic loading. The failure strength is the stress (in kPa) imposed on a parallel-bond when breakage occurs. In each of the four test models, the uppermost layer (i.e. 200–300 mm) includes the greatest number of breakages, while the central layer (i.e. 100–200 mm) contains the least number of breakages. In Test 2, the bottom reinforced layer has the least breakages compared to the other three model tests, although the confined ballast experiences slightly higher contact forces when compared to Test 1, as shown Fig. 18(b). Among the reinforced models, the top layer in Test 2, has the least number of breakages owing to a significantly lower applied monotonic stress. In Test 3, the central layer experienced the greatest number of breakages among the three reinforced model tests. The confined and stiffened ballast layer absorbs a proportion of the stress induced by the monotonic loading, leading to stress concentrations inside the geocell pocket. This observation is verified in Fig. 18(c), which, as a contact force distribution map for Test 2, shows that the ballast particles confined in the central layer experience greater contact forces when compared to the corresponding layer of the unreinforced model [Fig. 18(a)]. Owning to the central layer absorbing the load, the bottom layer in Test 2 reduces breakage by 37.7%. In Test 4, the suspended geocell pocket results in an additional 13.6% breakage within the top layer, when compared to Test 1. The uppermost layer exhibits the greatest amount of breakage due to the combined monotonic load and stress concentration [Fig. 18(d)]. The breakage in the underlying layers reduces by 50.2% and 38%, in the central and bottom layers respectively, when compared to the corresponding layers in Test 1. The high stress in the geocell pocket is reflected by the high average failure strength of 1,536 kPa. Overall, placing the geocell at the base level leads to a reduction in breakage of 29.7%. Strength increases due to the use of the geocell, with placement of the geocell at the base exhibiting the greatest strength gain.

Fig. 19 illustrates the location distribution of ballast breakage, which is represented by failure planes (disks), and categorized by the ballast shapes defined in Fig. 2. The sizes of the failure planes are scaled based on the radius of the broken-off particle and, hence, a large failure plane corresponds to a large sphere that has broken off from a ballast cluster. For all of the model tests, most of breakage occurs near the sleeper where the ballast is subjected to the major monotonic load. It should be noted that the clustered failure planes indicate the occurrence of multiple breaks in one ballast particle. Conversely, scattered failure planes indicate minor ballast breakage, which suggests occurrence of corner breakage due to the angular nature of the ballast.

The ballast breakage results are further categorized by the ballast shapes and test models, as summarized in Table 6. Shape 1 experiences the greatest number of breakages on average, which as expected is due to its high angularity. The finer spheres at the sharp corners are more vulnerable to breakage as a result of their lower bond strength. A significant breakage reduction is shown in the other three ballast shapes. Shape 2, being the roundest and least angular, shows the least number of breakages. Similar breakage characteristics are observed with Shapes 3 and 4, albeit Shape 4 is more angular than Shape 3. A possible reason for this is that Shape 4 is flat and hence there are more inter-ballast contacts with the surrounding ballast. In addition, all ballast shapes show similar failure strength, independent of their geometrical characters and angularity. This outcome agrees with the point load test carried out in the calibration stage described earlier.

Geocell Response

Fig. 20 shows the deformation magnitudes, drawn at the same scale, for the geocell pockets in the three reinforced model tests. The geocell in Test 2 experiences deformation with an average tensile strain of 9.7%, especially at its base due to the restricted ballast movement at this location. In addition, as shown on Fig. 20(a), the cell-wall to the right deforms laterally, which leads to tensile ruptures in the cell-wall, as shown in Fig. 21(a). The red disks in Fig. 21(a) indicate the orientations and diameters of the failure planes. The ballast movement highlighted in Fig. 16(b), pushes the cell-wall to expand and stretch under tensile force. The surrounding ballast (i.e. outside of the geocell pocket) cannot withstand the expansion of the cell-wall and hence it eventually exceeds its tensile strength. Furthermore, the geocell junction also experiences minor failure as a result of ballast penetration. In Test 3, no evident deformation was observed in the geocell pocket, other than vertical displacement along with the ballast settlement, reflected by the least average tensile strain of 8.8%. In Test 4, the geocell pocket experienced the greatest deformation with an average tensile strain of 12.6%. As shown in Fig. 21(b), the top and bottom edges of the geocell pocket experience shear ruptures under monotonic loading. Fig. 16(d) illustrates the contributing factor of the bottom ruptures, which is the reduced ballast movement in the layers beneath the reinforced section. As the sleeper displaces into the top ballast layer, the geocell pocket is forced to settle. However, the small contact interface between the base of the geocell and the ballast reduces the deformation of the underlying ballast. As the sleeper compresses further, the high contact pressure induces noticeable deformation in the bottom edge of the geocell resulting in the occurrence of the shear ruptures. Similar ruptures occur at the geocell top edge.

Cyclic Loading

Settlement

The cyclic loading scenario is important in assessing the long-term performance of the geocell and the reinforced ballast. Fig. 22 shows the relationships between settlement and the number of cycles of the four model tests. The relationships are displayed using a logarithmic scale to account for the large number of cycles. Overall, the reinforced model tests consistently outperform the unreinforced model over the entire range of cycles examined. For all model tests, the majority of the settlement occurred within the first 1,000 cycles, which is in agreement with previous studies (Leshchinsky and Ling, 2013, Ngo *et al.*, 2017). As was undertaken with the monotonic load tests, the settlement versus load cycle relationships are again subdivided into three zones: A, from cycles 1 to 10; B, from cycles 10 to 1,000; and C, from cycles 1,000 to 20,000. In Zone A, the reinforced models experience significantly reduced settlement than that exhibited in the unreinforced model (Test 1), demonstrating the benefit of the geocell reinforcement. Greater than 50% settlement reduction (the average reduction within each region) is obtained across all reinforced model tests. This performance agrees with the results obtained in the monotonic loading scenario described earlier. Within Zone A, all model tests exhibit small settlement rates, while Tests 1 and 4 settle faster at the end of Zone A. The settlement increases when all curves enter Zone B. The settlement of Test 2 is more pronounced when compared with that of the other three models, with Tests 3 and 4 yielding an average settlement reduction of 35% and 44%, respectively. The values demonstrate the value of the geocell in reducing settlement as a consequence of cyclic loading. Overall, placing the geocell 200 mm above the base provides the best performance with respect to cyclic loading, attaining a settlement reduction of 27% by the end of the test. In comparison, the reduction rate for model Test 3 is 12% and 3% for model Test 2.

The settlement response obtained by Leshchinsky and Ling (2013) and Satyal *et al.* (2018) are included in Fig. 22 for comparison. Leshchinsky and Ling (2013) applied cyclic loading to a pilot-scale, geocell-reinforced ballast embankment and examined the response of the embankment and Satyal *et al.* (2018) conducted finite element analysis (FEA) on a full-scale railway structure. As shown in Fig. 22, there is a discrepancy in the unreinforced cases between the current study and the results of Leshchinsky and Ling (2013). This is contributed to by the unconfined nature of their ballast embankment, in which the ballast can move freely in both the longitudinal and transverse directions. Additionally, differences in ballast gradation also added to the discrepancy. The current study uses the gradation with a D_{50} of 42.5 mm, while that adopted by Leshchinsky and Ling (2013) was 15.5 mm. In comparison with the FEA results, the disagreement in settlement mainly exists in the first 10,000 cycles, where the FEA yielded significantly lower settlement when compared with the current study. Also, the settlement responses are different between these two studies where, as discussed previously, most of the settlement occurred within the first 1,000 cycles in the current study. Whereas, minimal settlement (< 8mm) was recorded in the first 700 cycles in the FEA simulation, and this was followed by a dramatic increase, resulting in a similar final settlement (< 3mm difference), when compared with the current study. For Test 2 (i.e., placing the geocell 100 mm above the base), the main discrepancy exists in the early stage of the tests, reflected by an approximate 20 mm difference in settlement after the first load cycle. However, the difference becomes less evident towards the end of both tests, while the experimental, reinforced-models exhibited much greater improvement. Apart from the differences in boundary conditions and particle gradation, the geocell material likely contributes to the settlement discrepancy. Leshchinsky and Ling (2013) used a Novel Polymetric Alloy (NPA) geocell which provides different stiffness and tensile strength from that of HDPE geocell used in the present study.

Ballast Breakage Characteristics

The number of ballast breakages versus the number of cycles for all model tests are provided in Fig. 23. In the figure, all curves are divided into 4 zones: A, from cycles 1 to 10; B, from cycles 10 to 3,000; and C, from cycles 3,000 to 18,000; and D, from cycle 18,000 to 20,000. For each of the model tests, the number of breakages in Zone A remains largely constant. In Zone B, the number of breakages in each of the models increases, which mainly arises from the internal stress build-up. As expected, the unreinforced model exhibits the most breakages throughout the period of cycles examined. The three reinforced models exhibit a similar number of ballast breakages at the end of Zone B. Subsequently, into Zone C, the reinforced models exhibit noticeable deviation in the number of breakages until the end of each test, with Tests 2 and 4 experiencing greater breakage rates than Test 3. Within the same zone, in the unreinforced model, the number of breakages increases at a reduced rate. For all reinforced models, after approximately the 18,000th load cycle (i.e. Zone D), the number of breakages rapidly increases until the end of each test. This is attributed to the internal contact stresses (as a result of the denser assemblies) reaching the strength limits of some of the parallel-bonded spheres, while these particular bonds had already ruptured in the unreinforced model.

As for the monotonic loading scenario, the breakage results are categorized by ballast layers and model tests, as summarized in Table 7. Compared to the monotonic loading situation, the ballast breakages are more evenly distributed across the three layers of interest. Similar distributions of uniform ballast breakage are illustrated in Fig. 24. The uniform distribution is caused by the lower cyclic load acting on the ballast, whereas under monotonic loading, the applied load is much greater. In Tests 2 and 3, the ballast in the respective geocell-reinforced layers fracture less often than the ballast in the unreinforced layers of the same test. In Test 2, however, the geocell-reinforced layer does not perform as well as its counterpart in the monotonic loading case; resulting in only a 15.5% reduction in ballast breakage, with no increase in failure strength. For each of the reinforced cases, the ballast in the uppermost layer (200–300 mm) rupture more often than those in the lower layers, independent of the geocell embedment depth. In Tests 2 and 3, the geocell pockets enhance the stiffness of the layer of interest and reduce the corresponding number of breakages. Simultaneously, the geocell pockets restrict ballast movement and rearrangement in the top layers which result in stress concentrations and hence a greater number of breakages. In Test 4, as with monotonic loading, the stiffened top layer restricts stress propagation into the underlying layers, as a result, the stress concentrates in the top layer, resulting in 32.1% more ballast breakages and 6.2% higher average failure strength.

Overall, a slight failure strength increase is exhibited by the reinforced model tests. Placing the geocell 100 mm above the subgrade is the most optimal solution for mitigating ballast breakage, where the highest breakage reduction of 19.8% and strength increase of 2.6% are attained. Placing the geocell directly above the subgrade is less effective when the performance of the model under cyclic loading condition is assessed. In this situation, the improvement percentage is a breakage reduction of 5.5% and a 1.2% failure strength increase.

At end of each test, the final PSDs were examined for all model tests, as shown in Table 8. The final PSDs agree with the number of breakages recorded for each test, which is reflected by the evident shifts in each curve. Besides having the least number of breakages, Test 3 performed best in preventing the ballast breaking down into finer particles which, as mentioned previously, is the most common source of ballast fouling (Selig and Waters, 1994).

As with monotonic loading, the ballast breakage results are categorized based on the ballast and model tests, as summarized in Table 9. The results agree well with those obtained with the monotonic loading. The number of breakages decreases along with decrease in angularity. The Shape 1 ballast exhibited the greatest number of breakages, with 36–52% more ruptures than the other ballast shapes. In addition, the Shape 1 ballast resulted in the smallest breakage diameter (i.e. failure plane) on average, which indicates a major proportion of corner breakage. This phenomenon is further validated by the lowest average failure strength (964 kPa) for Shape 1. The other ballast shapes, however, result in, on average, larger breakage diameters. The Shape 2 ballast experiences the least number of breakages, owing to its more rounded surface. It should be noted that the average ballast strengths of all of the four shapes are noticeably lower than their counterparts when subjected to monotonic loading. This is because the broken-off spheres are of smaller diameters, which as expected is due to the significantly lower loading magnitude applied in the cyclic loading condition.

Geocell Response

The responses of the geocell, in terms of displacement and deformation, are examined at the end of the cyclic loading tests, for all reinforced models, and these are presented in Fig. 25. In Test 2, the geocell pocket experiences more localized deformation on the lower left-hand side. The local deformation results in a minor rupture at the place of concern. The remaining areas of the geocell experience minimal deformation, i.e. the lowest average tensile strain of 4.3%, and remain in a serviceable condition. No rupture is observed in either the cell-wall or the junction components of the geocell in Tests 3 and 4. The two test models, however, exhibit relatively large deformation, particularly on the right-hand side of the respective pockets. The ballast tends to move to one side, resulting in higher average tensile strains of 5.1% and 6.2%, respectively.

Conclusions

This study examines the mechanical behavior of geocell-reinforced railway ballast using the discrete element method (DEM). The ballast is modeled as being breakable and in typical angular shapes. The DEM micro-properties are calibrated based on a series of laboratory tests performed on the ballast and geocell sample materials. The tests include unconfined compressive and point load tests on the ballast, uniaxial tensile strength tests on the cell-wall and seam strength tests on the junction. The ballast chamber models are subjected to the monotonic and cyclic loading. The cyclic loading is continued to 20,000 cycles. From the two load tests, the performance of the geocell in term of reinforcing the ballast is examined. The performance includes assessing ballast settlement, geocell responses, and ballast breakage characteristics. The breakage characteristics include the number of breakages, location distributions, failure strength, breakage diameters and shape effects. Results are compared to those obtained in previous studies. The following conclusions are drawn:

1. From the application of monotonic loading, placing the geocell 200 mm above the base outperforms other model tests with respect to settlement reduction. Placing the geocell directly on the base, however, reduces ballast breakage to the greatest extent.

2. Under monotonic loading, the geocell can effectively reduce the number of ballast breakages and help increase the strength of the reinforced layer if the geocell is placed at the base or 100 mm above. Placing the geocell directly beneath the sleeper reduces the number of breakages in the underlying layers but increases them in the reinforced layer.
3. Offsetting the geocell location influences the performance of ballast in different aspects and at various levels. Under monotonic loading, placing the geocell 200 mm above the base consistently performs best, reducing settlement by 24% and 15% relative to placing the geocell on the base and 100 mm above the base, respectively. Meanwhile, placing the geocell 100 mm above the base achieves the better performance in breakage reduction by 6.9% compared with placing the geocell 200 mm above the base. Overall, placing the geocell 200 mm above the base is the optimal location where settlement and ballast breakage are concerned, for the scenarios examined in the current model. The use of a deeper geocell or a double-layer system may improve settlement and breakage characteristics simultaneously, but these are beyond the scope of the present study and hence require further examination.
4. Ballast shape plays an important role in governing breakage. Ballast with major angularities rupture more, and vice versa. The sharper corners of the ballast are vulnerable to breakage, leading to the small fractures. Rounded ballast exhibits better performance with respect to minimizing breakage.
5. The geocell experiences local failures under both monotonic and cyclic loading. The material is subjected to more damage when the geocell is

placed on the base. The center of the cell-wall component is more vulnerable to the failure and where ruptures are more likely to occur. The cell-wall junction was shown to be strong and does not debond. However, minor, local debonding occurs when the geocell is placed on the base and subjected to monotonic loading.

6. Whilst this study presents a valid and advanced geocell-reinforced ballast model, there are limitations exist that should be considered in future study. Firstly, a more comprehensive calibration program that involves additional tests for both geocell and ballast clusters, such as the torsion resistance of geocell. Secondly, a user-defined non-linear parallel-bond can be introduced to mitigate the differences between simulation and experimental results in the calibration stage. Last but not least, an experimental counterpart should be used to validate the accuracy of the simulation.

Data Availability Statement

All data, models, or code generated or used during the study are proprietary or confidential in nature and may only be provided with restrictions.

References

ARTC (2007). "ETA-04-01 Ballast Specification." *Engineering (Track & Civil) Standard*, Australian Rail Track Corporation Ltd., Australia, 6.

ARTC (2012). "Engineering (Track & Civil) Code of Practice - Section 4 Ballast." Australian Rail Track Corporation Ltd., Australia, 12.

ARTC (2014). "Route Access Standard." *General Information*, Australian Rail Track Corporation Ltd., Australia.

ARTC (2017). "Engineering (Track & Civil) Code of Practice - Section 2 Sleepers and Fastenings." Australian Rail Track Corporation Ltd., Australia.

ARTC (2018). "Common Interface Requirements WOS 01.200." *WOS 01.211 - Wheels, Design and Manufacture*, Australian Rail Track Corporation Limited (ARTC), 94.

ASTM (2004). "Standard Test Method for Tensile Properties of Plastics." *ASTM D638-03*, ASTM International, PA, US.

Australia, S. (2015). "AS 2758.7 Aggregates and rock for engineering purposes - Part 7: Railway ballast." SAI Global Limited, Sydney, 13.

Chen, C., McDowell, G. R., and Thom, N. H. (2012). "Discrete element modelling of cyclic loads of geogrid-reinforced ballast under confined and unconfined conditions." *Geotextiles and Geomembranes*, 35, 76-86.

Chen, C., McDowell, G. R., and Thom, N. H. (2013). "A study of geogrid-reinforced ballast using laboratory pull-out tests and discrete element modelling." *Geomechanics and Geoengineering*, 8(4), 244-253.

Chen, R.-H., Huang, Y.-W., and Huang, F.-C. (2013). "Confinement effect of geocells on sand samples under triaxial compression." *Geotextiles and Geomembranes*, 37, 35-44.

Chen, R.-H., Wu, C.-P., Huang, F.-C., and Shen, C.-W. (2013). "Numerical analysis of geocell-reinforced retaining structures." *Geotextiles and Geomembranes*, 39, 51-62.

Cundall, P. A. (2001). "A discontinuous future for numerical modelling in geomechanics?" *Proceedings of the Institution of Civil Engineers - Geotechnical Engineering*, 149(1), 41-47.

Cundall, P. A., and Strack, O. D. L. (1979). "A discrete numerical model for granular assemblies." *Géotechnique*, 29(1), 47-65.

Dash, S. K. (2012). "Effect of geocell type on load-carrying mechanisms of geocell-reinforced sand foundations." *International Journal of Geomechanics*, 12(5), 537-548.

Dash, S. K., and Bora, M. C. (2013). "Improved performance of soft clay foundations using stone columns and geocell-sand mattress." *Geotextiles and Geomembranes*, 41, 26–35.

Group, I. C. (2008). *PFC3D: Particle Flow Code in 3 Dimensions*, Minneapolis.

Hegde, A., and Sitharam, T. G. (2015). "3-Dimensional numerical modelling of geocell reinforced sand beds." *Geotextiles and Geomembranes*, 43(2), 171–181.

Hegde, A. M., and Sitharam, T. G. (2015). "Three-dimensional numerical analysis of geocell-reinforced soft clay beds by considering the actual geometry of geocell pockets." *Canadian Geotechnical Journal*, 52(9), 1396-1407.

Hossain, Z., Indraratna, B., Darve, F., and Thakur, P. K. (2007). "DEM analysis of angular ballast breakage under cyclic loading." *Geomechanics and Geoengineering*, 2(3), 175-181.

Huang, H., Tutumluer, E., and Dombrow, W. (2009). "Laboratory characterization of fouled railroad ballast behavior." *Transportation Research Record: Journal of the Transportation Research Board*, 2117, 93-101.

Indraratna, B., Ngo, N. T., Rujikiatkamjorn, C., and Vinod, J. S. (2014). "Behavior of fresh and fouled railway ballast subjected to direct shear testing: Discrete element simulation." *International Journal of Geomechanics*, 14(1), 34-44.

Indraratna, B., Nimbalkar, S., Christie, D., Rujikiatkamjorn, C., and Vinod, J. S. (2010). "Field Assessment of the Performance of a Ballasted Rail Track with and without Geosynthetics." *Journal of Geotechnical and Geoenvironmental Engineering*, 136(7), 907-917.

Indraratna, B., Thakur, P. K., and Vinod, J. S. (2010). "Experimental and numerical study of railway ballast behavior under cyclic loading." *International Journal of Geomechanics*, 10(4), 134-144.

Indraratna, B., Vinod, J. S., and Lackenby, J. (2009). "Influence of particle breakage on the resilient modulus of railway ballast." *Geotechnique*, 59(7), 643-646.

Irazábal, J., Salazar, F., and Oñate, E. (2017). "Numerical modelling of granular materials with spherical discrete particles and the bounded rolling friction model. Application to railway ballast." *Computers and Geotechnics*, 85(Supplement C), 220-229.

Itasca (2009). *PFC3D 4.0 User's Manual*, Itasca Consulting Group, Inc., Minnesota, USA.

Itasca (2009). "Particle Flow Code in Three Dimensions " *Version 4*, Itasca Consulting Group, Inc., Monnesota, USA.

Leshchinsky, B., and Ling, H. (2013). "Effects of Geocell Confinement on Strength and Deformation Behavior of Gravel." *Journal of Geotechnical and Geoenvironmental Engineering*, 139(2), 340-352.

Leshchinsky, B., and Ling, H. I. (2013). "Numerical modeling of behavior of railway ballasted structure with geocell confinement." *Geotextiles and Geomembranes*, 36, 33-43.

Li, H., and McDowell, G. R. (2018). "Discrete element modelling of under sleeper pads using a box test." *Granular Matter*, 20(2).

Lim, W. L., and McDowell, G. R. (2005). "Discrete element modelling of railway ballast." *Granular Matter*, 7(1), 19-29.

Liu, Y., Deng, A., and Jaksa, M. (2015). "Discrete element modelling of geocell-reinforced track ballast under static and cyclic loading." *Proc. The 12th Australia–New Zealand Conference on Geomechanics*Wellington, New Zealand, 279–286.

Liu, Y., Deng, A., and Jaksa, M. (2018). "Three-dimensional modeling of geocell-reinforced straight and curved ballast embankments." *Computers and Geotechnics*, 102, 53-65.

Lobo-Guerrero, S., and Vallejo, L. E. (2006). "Discrete element method analysis of railtrack ballast degradation during cyclic loading." *Granular Matter*, 8(3-4), 195-204.

Lu, M., and McDowell, G. R. (2006). "The importance of modelling ballast particle shape in the discrete element method." *Granular Matter*, 9(1-2), 69-80.

Lu, M., and McDowell, G. R. (2008). "Discrete element modelling of railway ballast under triaxial conditions." *Geomechanics and Geoengineering*, 3(4), 257-270.

Lu, M., and McDowell, G. R. (2010). "Discrete element modelling of railway ballast under monotonic and cyclic triaxial loading." *Géotechnique*, 60(6), 459-467.

Madhavi Latha, G., and Rajagopal, K. (2007). "Parametric finite element analyses of geocell-supported embankments." *Canadian Geotechnical Journal*, 44(8), 917-927.

Mehdipour, I., Ghazavi, M., and Moayed, R. Z. (2013). "Numerical study on stability analysis of geocell reinforced slopes by considering the bending effect." *Geotextiles and Geomembranes*, 37, 23–34.

Moghaddas Tafreshi, S. N., Shaghaghi, T., Tavakoli Mehrjardi, G., Dawson, A.R., Ghadrdan, M. (2015). "A simplified method for predicting the settlement of circular footings on multi-layered geocell-reinforced non-cohesive soils." *Geotextiles and Geomembranes*, 43, 332–344.

Ngo, N. T., Indraratna, B., and Rujikiatkamjorn, C. (2014). "DEM simulation of the behaviour of geogrid stabilised ballast fouled with coal." *Computers and Geotechnics*, 55, 224-231.

Ngo, N. T., Indraratna, B., and Rujikiatkamjorn, C. (2017). "Simulation ballasted track behavior: Numerical treatment and field application." *International Journal of Geomechanics*, 17(6), 04016130.

Ngo, N. T., Indraratna, B., Rujikiatkamjorn, C., and Mahdi Biabani, M. (2015). "Experimental and discrete element modeling of geocell-stabilized subballast subjected to cyclic loading." *Journal of Geotechnical and Geoenvironmental Engineering*, 04015100.

Oliaei, M., Kouzegaran, S. (2017). "Efficiency of cellular geosynthetics for foundation reinforcement." *Geotextiles and Geomembranes*, 45, 11-22.

Potyondy, D. O., and Cundall, P. A. (2004). "A bonded-particle model for rock." *International Journal of Rock Mechanics and Mining Sciences*, 41(8), 1329-1364.

Qian, Y., Mishra, D., Tutumluer, E., and Kazmee, H. A. (2015). "Characterization of geogrid reinforced ballast behavior at different levels of degradation through triaxial shear strength test and discrete element modeling." *Geotextiles and Geomembranes*, 43(5), 393-402.

Sadeghi, J. M. (2008). "Experimental evaluation of accuracy of current practices in analysis and design of railway track sleepers." *Canadian Journal of Civil Engineering*, 35(9), 881-893.

Satyal, S. R., Leshchinsky, B., Han, J., and Neupane, M. (2018). "Use of cellular confinement for improved railway performance on soft subgrades." *Geotextiles and Geomembranes*, 46(2), 190-205.

Selig, E. T., and Waters, J. M. (1994). *Track Geotechnology and Substructure Management*, Thomas Telford Publications, London.

Sun, Y., and Zheng, C. (2017). "Breakage and shape analysis of ballast aggregates with different size distributions." *Particuology*, 35, 84-92.

Taghavi, R. (2011). "Automatic clump generation based on mid-surface." *Continuum and Distinct Element Numerical Modeling in Geomechanics*Melbourne, Australia.

Tanyu, B. F., Aydilek, A. H., Lau, A. W., Edil, T. B., and Benson, C. H. (2013). "Laboratory evaluation of geocell-reinforced gravel subbase over poor subgrades." *Geosynth Int*, 20(2), 47–61.

Tutumluer, E., Qian, Y., Hashash, Y. M. A., Ghaboussi, J., and Davis, D. D. (2013). "Discrete element modelling of ballasted track deformation behaviour." *International Journal of Rail Transportation*, 1(1-2), 57-73.

Wang, B., Martin, U., and Rapp, S. (2017). "Discrete element modeling of the single-particle crushing test for ballast stones." *Computers and Geotechnics*, 88, 61-73.

Wang, C., Deng, A., and Taheri, A. (2018). "Three-dimensional discrete element modeling of direct shear test for granular rubber–sand." *Computers and Geotechnics*, 97, 204-216.

Wang, Y. H., and Leung, S. C. (2008). "A particulate-scale investigation of cemented sand behavior." *Canadian Geotechnical Journal*, 45(1), 29-44.

Wang, Z., Jacobs, F., and Ziegler, M. (2016). "Experimental and DEM investigation of geogrid–soil interaction under pullout loads." *Geotextiles and Geomembranes*, 44(3), 230-246.

Xu, M., Hong, J., and Song, E. (2017). "DEM study on the effect of particle breakage on the macro- and micro-behavior of rockfill sheared along different stress paths." *Computers and Geotechnics*, 89(Supplement C), 113-127.

Yan, Y., Zhao, J., and Ji, S. (2014). "Discrete element analysis of breakage of irregularly shaped railway ballast." *Geomechanics and Geoengineering*, 10(1), 1-9.

Yang, X., Han, J., Parsons, R. L., and Leshchinsky, D. (2010). "Three-dimensional numerical modeling of single geocell-reinforced sand." *Frontiers of Architecture and Civil Engineering in China*, 4(2), 233-240.

Yang, X., Han, J., Pokharel, S. K., Manandhar, C., Parsons, R. L., Leshchinsky, D., and Halahmi, I. (2012). "Accelerated pavement testing of unpaved roads with geocell-reinforced sand bases." *Geotextiles and Geomembranes*, 32, 95-103.

Zhang, L., Zhao, M., Shi, C., and Zhao, H. (2010). "Bearing capacity of geocell reinforcement in embankment engineering." *Geotextiles and Geomembranes*, 28(5), 475-482.

Zhang, Q., Zhu, H., Zhang, L., and Ding, X. (2011). "Study of scale effect on intact rock strength using particle flow modeling." *International Journal of Rock Mechanics and Mining Sciences*, 48(8), 1320-1328.

List of Tables

Table 1. Micro-properties of the materials in the UCS model

Type	Micro-properties	Value
Material	Density (kg/m^3)	2,500
Linear contact (ballast – wall)	Deformability (N/m)	1.2 x 10^9
	Stiffness ratio	1
	Damping ratio	0.5
	Friction coefficient	0.28
Parallel-bond (within ballast only)	Bond gap (mm)	2 x 10^{-5}
	Bond deformability (N/m)	1.2 x 10^8
	Bond tensile strength (N/m^2)	1.7 x 10^7
	Bond cohesion (N/m^2)	1.65 x10^7
	Bond friction angle (°)	55

Table 2. Micro-properties of parallel-bonds for cell-wall and junction

Type	Micro-properties	Cell-wall	Junction
Material	Density (kg/m^3)	950	950
Linear contact (geocell - ballast)	Deformability (N/m)	1.5 x 10^6	1.5 x 10^6
	Friction coefficient	0.18	0.18
	Stiffness ratio	1.0	1.0
	Damping ratio	0.5	0.5
Parallel-bond (within geocell only)	Bond gap (mm)	0.0	0.0
	Bond deformability (N/m)	1.23 x 10^6	2.98 x 10^8
	Bond stiffness ratio	1.0	1.0
	Bond tensile strength (N/m^2)	8.7 x 10^6	8.0 x 10^6
	Bond cohesion (N/m^2)	1.8 x 10^6	3.98 x 10^7
	Bond friction angle (°)	0.0	0.0

Table 3. Load calculation model proposed by Sadeghi (2008)

Factor	Proposed model	
Design wheel load	$P = \varnothing P_s$	Eq. 1
Dynamic coefficient	$\varnothing = 1 + 4.73\, {}^{V}\!/_{D}$	Eq. 2
Rail seat load	$q_r = 0.474\ (1.27\ S + 0.238)\ P$	Eq. 3
Maximum contact load (After tamping)	$w_2 = 2.954\ {}^{q_r}\!/_{L_s}$	Eq. 4

Note: P_s = monotonic wheel load (t); V = train velocity (km/h); D = wheel diameter (mm); S = sleeper spacing (m); and L_s = sleeper length (m).

Table 4. Parameters used for the calculation of maximum contact pressure

Parameters	Value	Condition applied
Wheel diameter *D* (mm)	920	Coal traffic wagon (ARTC, 2018)
Train velocity *V* (km/h)	60	Hunter Valley coal traffic wagon (ARTC, 2014)
Sleeper spacing *S* (m)	0.6	Typical prestressed concrete sleeper spacing on a straight line (ARTC, 2017)
Sleeper length L_s (m)	2.5	Heavy duty prestressed concrete sleeper (ARTC, 2017)
Static wheel load P_s (t)	12.5	Hunter Valley coal traffic wagon (ARTC, 2017)

Table 5. Ballast breakage and failure strength results categorized by layers under monotonic loading

Test	By layer					Ballast box model			
	Layer (mm)	Number of Breakages	Breakage reduction	Average failure strength (kPa)	Strength increase	Number of Breakages	Breakage reduction	Average failure strength (kPa)	Strength increase
1	200–300	828	*NA*	1390	*NA*	1,436	*NA*	1,165	*NA*
	100–200	237		1063					
	0–100	371		1044					
2	200–300	688	16.9%	1481	6.58%	1,010	29.7%	1,288	10.5%
	100–200	121	48.9%	1214	14.20%				
	0–100 (reinforced)	201	45.8%	1171	12.10%				
3	200–300	823	0.6%	1479	6.45%	1,218	15.2%	1,284	10.2%
	100–200 (reinforced)	164	30.8%	1279	20.39%				
	0–100	231	37.7%	1095	4.86%				
4	200–300 (reinforced)	941	–13.6%	1536	10.53%	1,289	10.2%	1,261	8.2%
	100–200	118	50.2%	1151	8.29%				
	0–100	230	38.0%	1097	5.08%				

Table 6. Ballast breakage results categorized by ballast shape and test model under monotonic loading

Shape	Behavior	Test model				Average
		1	2	3	4	
1	No. of Breakages	694	482	607	556	585
	Avg. failure strength (kPa)	1,169	1,272	1,319	1,254	1,254
	Avg. breakage dia. (mm)	4.88	5.21	6.53	7.61	6.06
2	No. of Breakages	173	147	164	218	176
	Avg. failure strength (kPa)	1,161	1,248	1,305	1,273	1,247
	Avg. breakage dia. (mm)	5.05	5.34	7.21	9.28	6.72
3	No. of Breakages	259	212	193	265	232
	Avg. failure strength (kPa)	1,263	1,302	1,309	1,272	1,287
	Avg. breakage dia. (mm)	4.34	5.12	6.91	8.28	6.16
4	No. of Breakages	310	169	254	250	246
	Avg. failure strength (kPa)	1,201	1,332	1,205	1,246	1,246
	Avg. breakage dia. (mm)	4.28	5.11	5.23	7.58	5.55

Table 7. Ballast breakage and failure strength results categorized by layers under cyclic loading

Test	By layer					Ballast chamber model			
	Layer (mm)	Number of breakages	Breakage reduction	Avg. failure strength (kPa)	Strength increase	Number of breakages	Breakage reduction	Avg. failure strength (kPa)	Strength increase
	200–300	598		933					
1	100–200	388	NA	1,012	NA	1,668	NA	982	NA
	0–100	682		1,001					
	200–300	780	–30.4%	928	–0.6%				
2	100–200	264	32.0%	1,056	4.4%	1,577	–5.5%	994	1.2%
	0–100 (reinforced)	576	15.5%	997	–0.4%				
	200–300	614	–2.7%	971	4.1%				
3	100–200 (reinforced)	257	33.8%	1,028	1.5%	1,338	–19.8%	1,007	2.6%
	0–100	467	31.5%	1,023	2.2%				
	200–300 (reinforced)	790	–32.1%	991	6.2%				
4	100–200	238	38.7%	993	–1.9%	1,452	–12.9%	1,011	3.0%
	0–100	424	37.8%	1,049	4.8%				

Table 8. Final particle size distributions

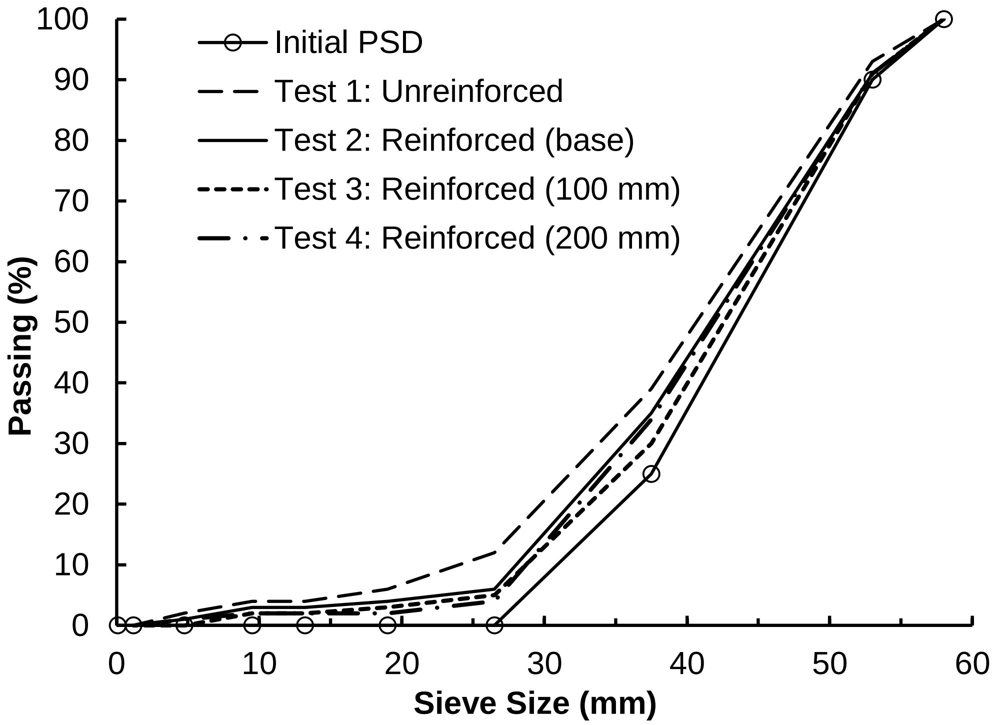

Sieve Size (mm)	Initial	Test 1	Test 2	Test 3	Test 4
58	100	100	100	100	100
53	90	93	91	91	91
37.5	25	39	35	30	34
26.5	0	12	6	5	4
19	0	6	4	3	2
13.2	0	4	3	2	2
9.5	0	4	3	2	2
4.75	0	2	1	0	1
1.18	0	0	0	0	0

Table 9. Ballast breakage results categorized by ballast shape and test model under cyclic loading

Shape	Behavior	Test				Average
		1	2	3	4	
1	No. of Breakages	575	636	520	548	570
	Avg. failure strength (kPa)	985	954	1,003	996	964
	Avg. breakage dia. (mm)	2.88	3.05	3.07	3.08	3.02
2	No. of Breakages	328	298	203	261	273
	Avg. failure strength (kPa)	946	1,001	956	952	985
	Avg. breakage dia. (mm)	3.53	3.68	3.84	3.97	3.76
3	No. of Breakages	408	305	285	242	310
	Avg. failure strength (kPa)	1,016	1,022	1,086	1,029	1,038
	Avg. breakage dia. (mm)	3.72	3.78	3.83	3.8	3.78
4	No. of Breakages	357	381	330	401	367
	Avg. failure strength (kPa)	982	998	984	969	983
	Avg. breakage dia. (mm)	3.74	3.78	3.96	3.65	3.77

Template No.	Cluster Template	Shape and Angularity	Number of Particles
1	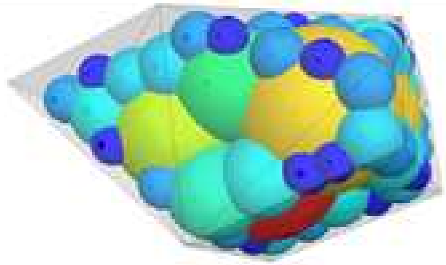	Thin, high angularity	44
2	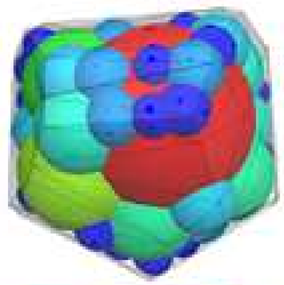	Round, low angularity	41
3	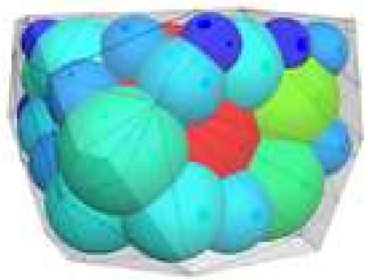	Flat, low angularity	41
4	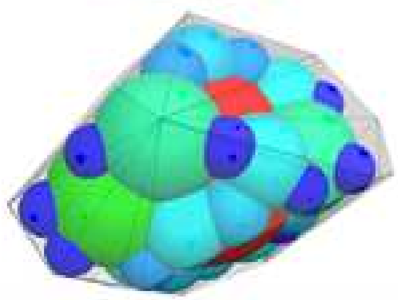	Plump, moderate angularity	41

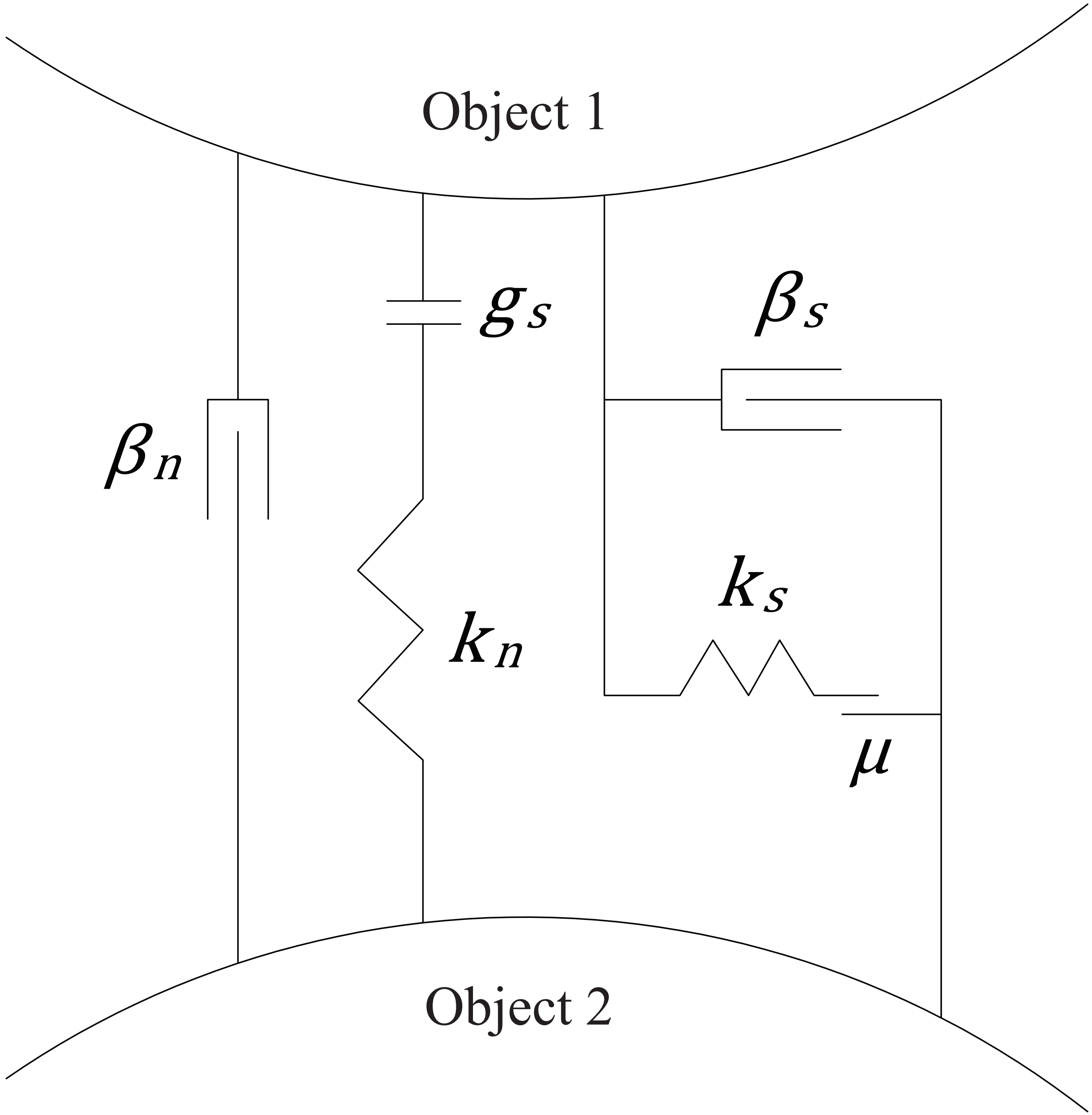
Object 1
g_s
β_s
β_n
k_s
k_n
μ
Object 2

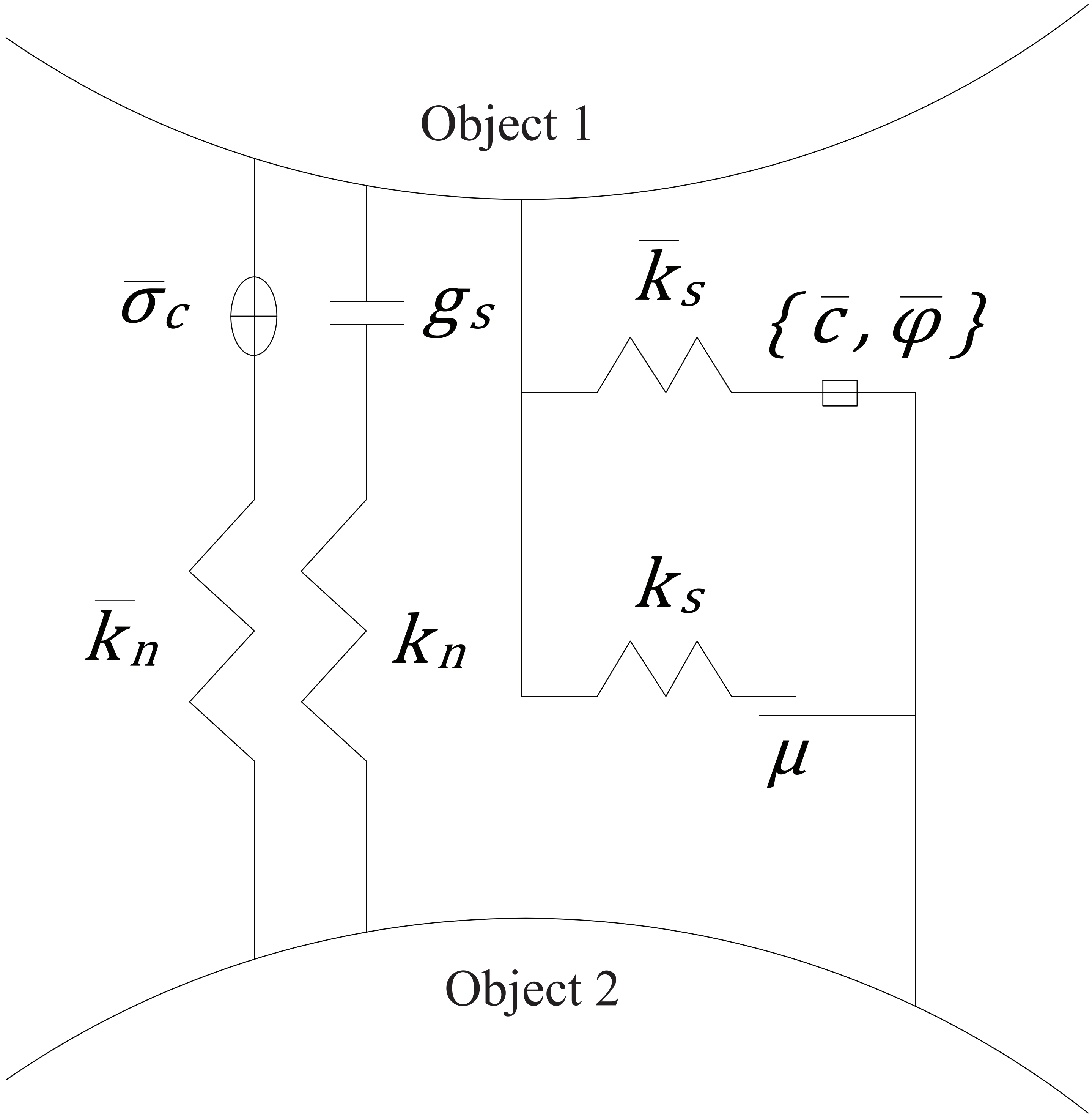

Object 1
$\bar{\sigma}_c$
g_s
$\bar{k}_s$
$\{\bar{c}, \bar{\varphi}\}$
k_s
$\bar{k}_n$
k_n
μ
Object 2

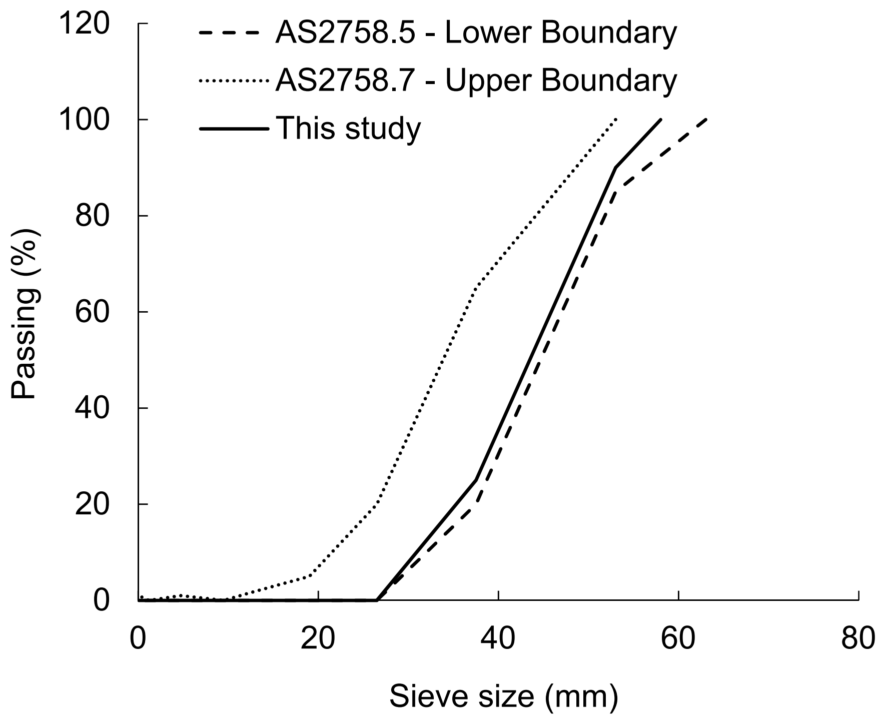

AS2758.5 - Lower Boundary
AS2758.7 - Upper Boundary
This study
120
100
80
60
40
20
0
Passing (%)
0
20
40
60
80
Sieve size (mm)

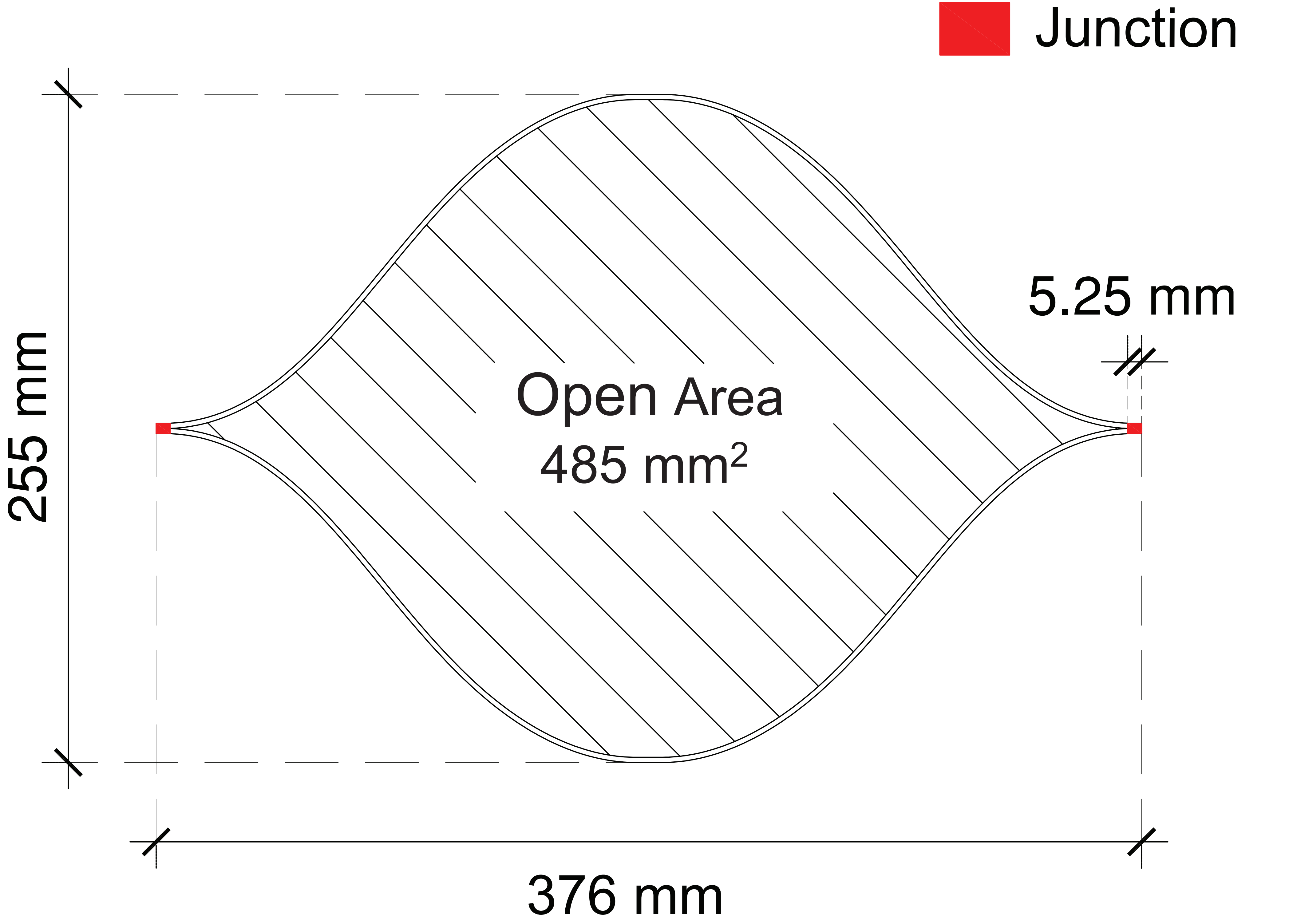
Junction
5.25 mm
255 mm
Open Area
485 mm²
376 mm

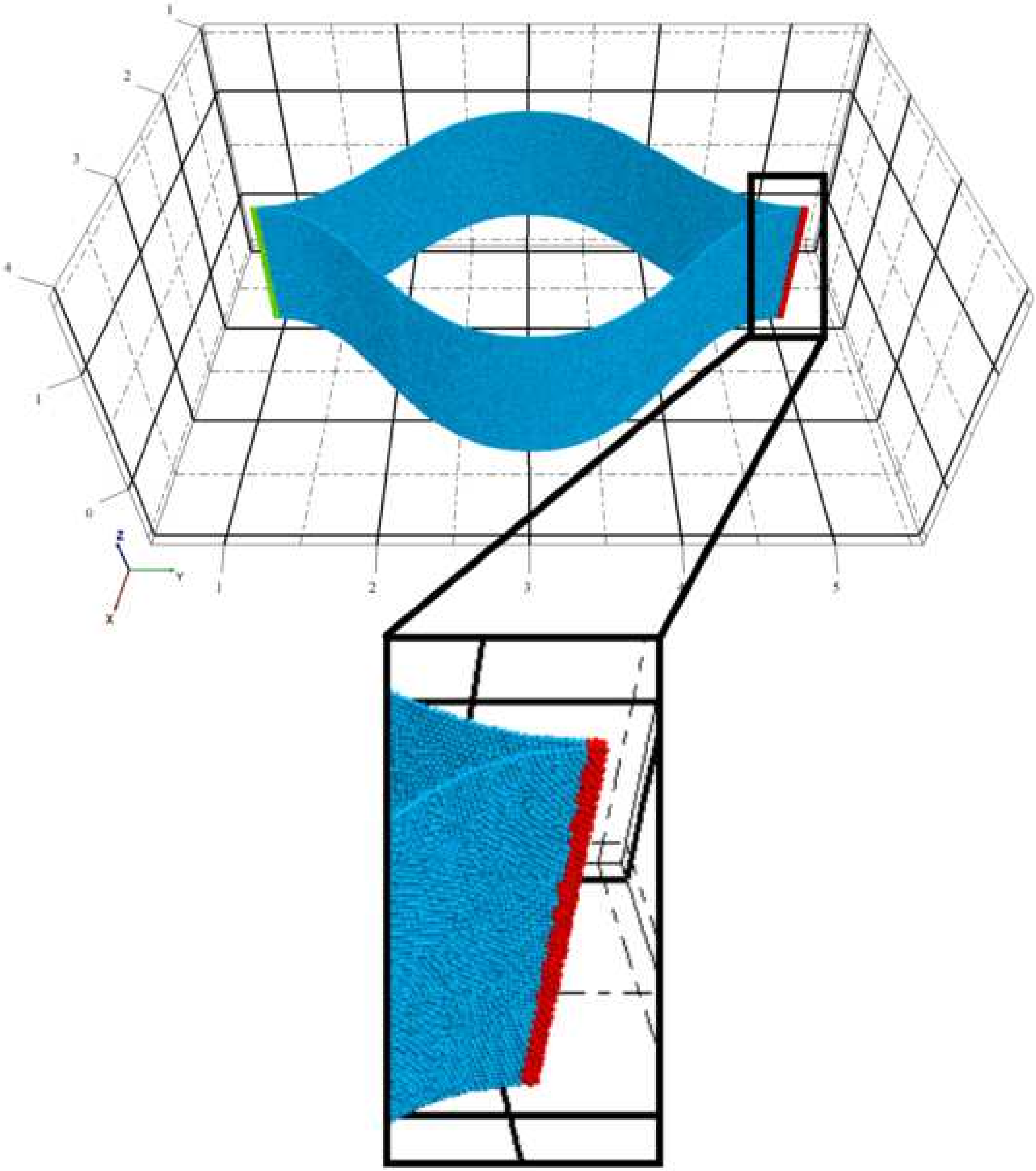
1
2
3
4
1
0
Z
Y
X
1
2
3
5

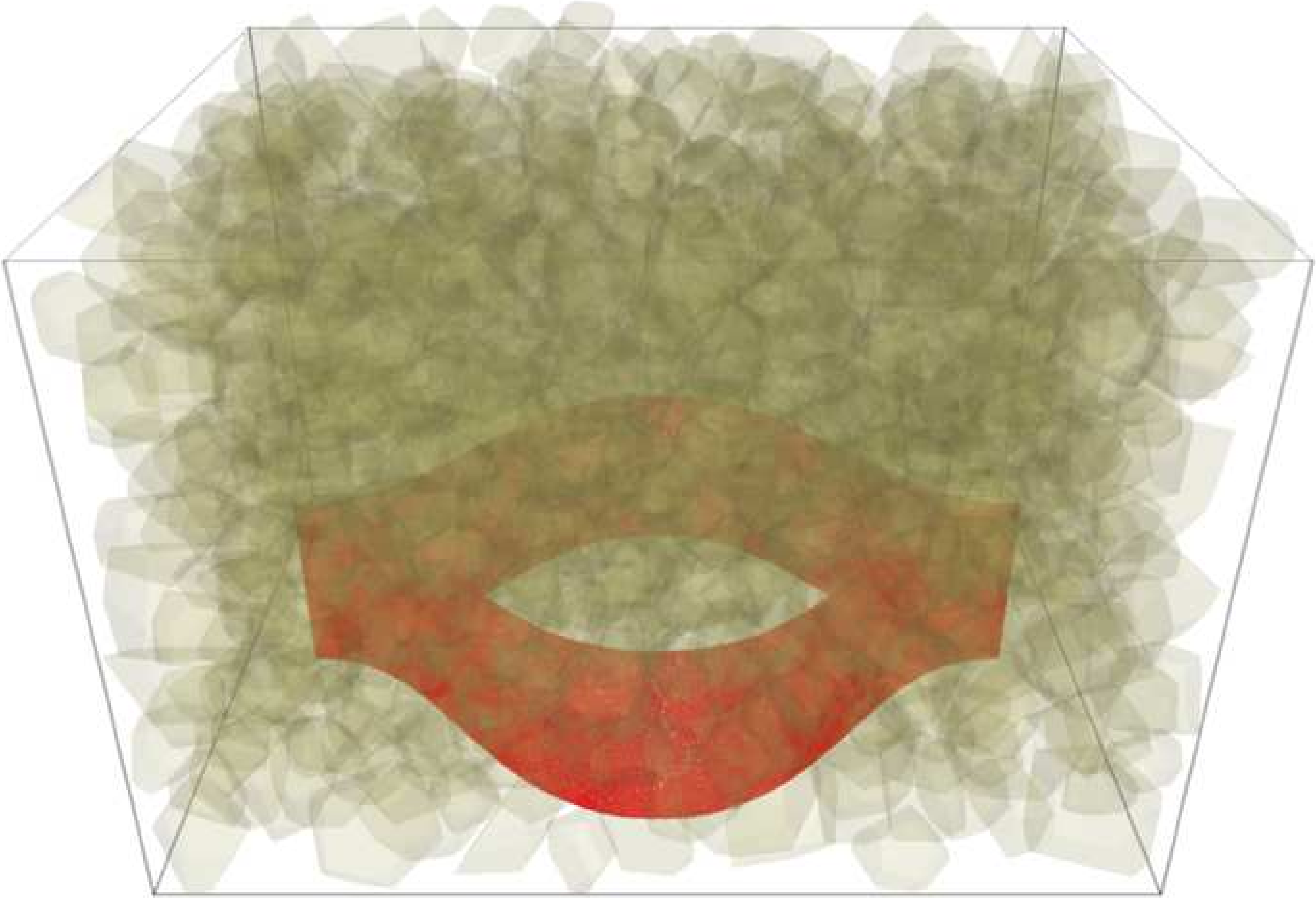

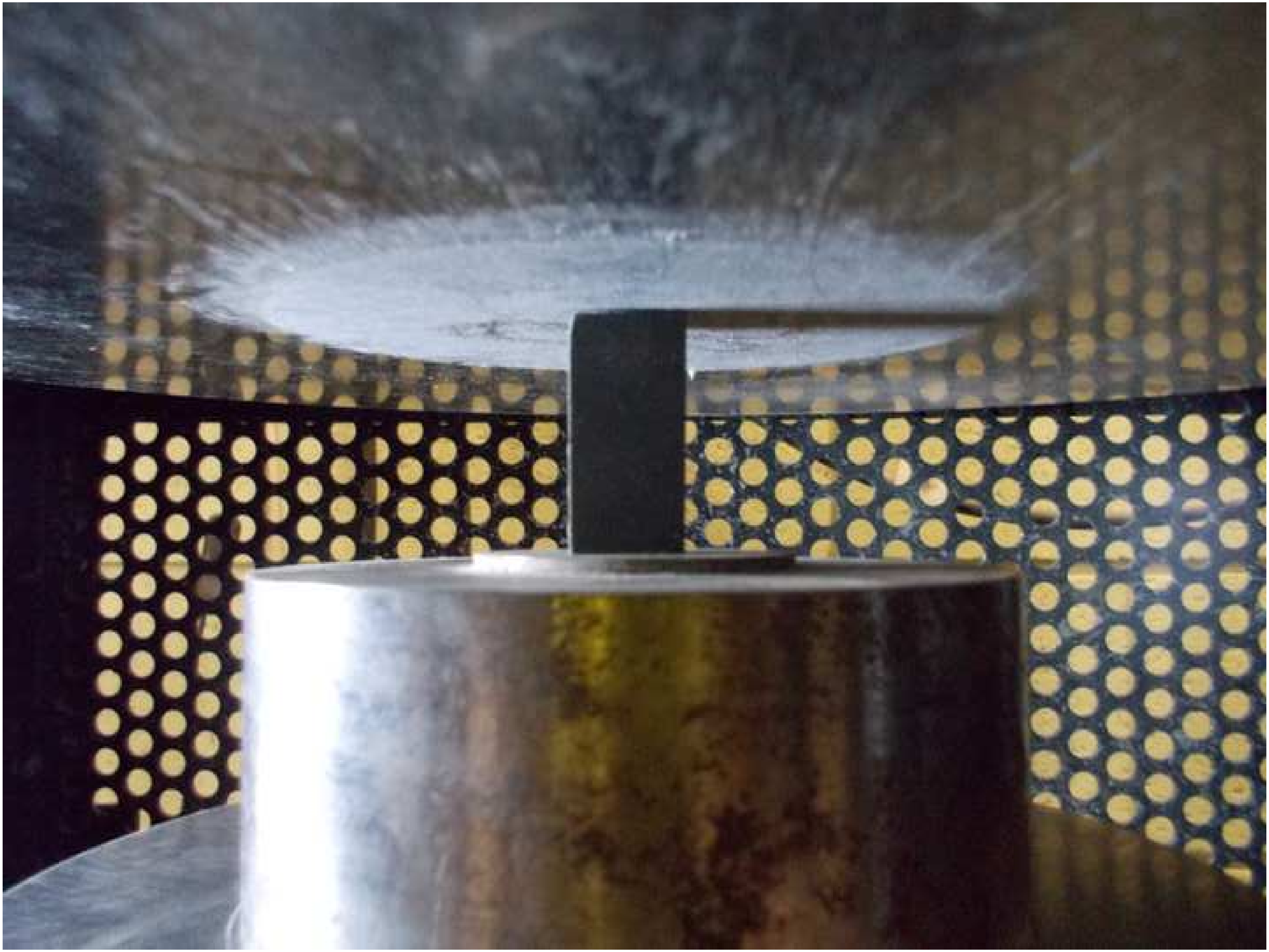

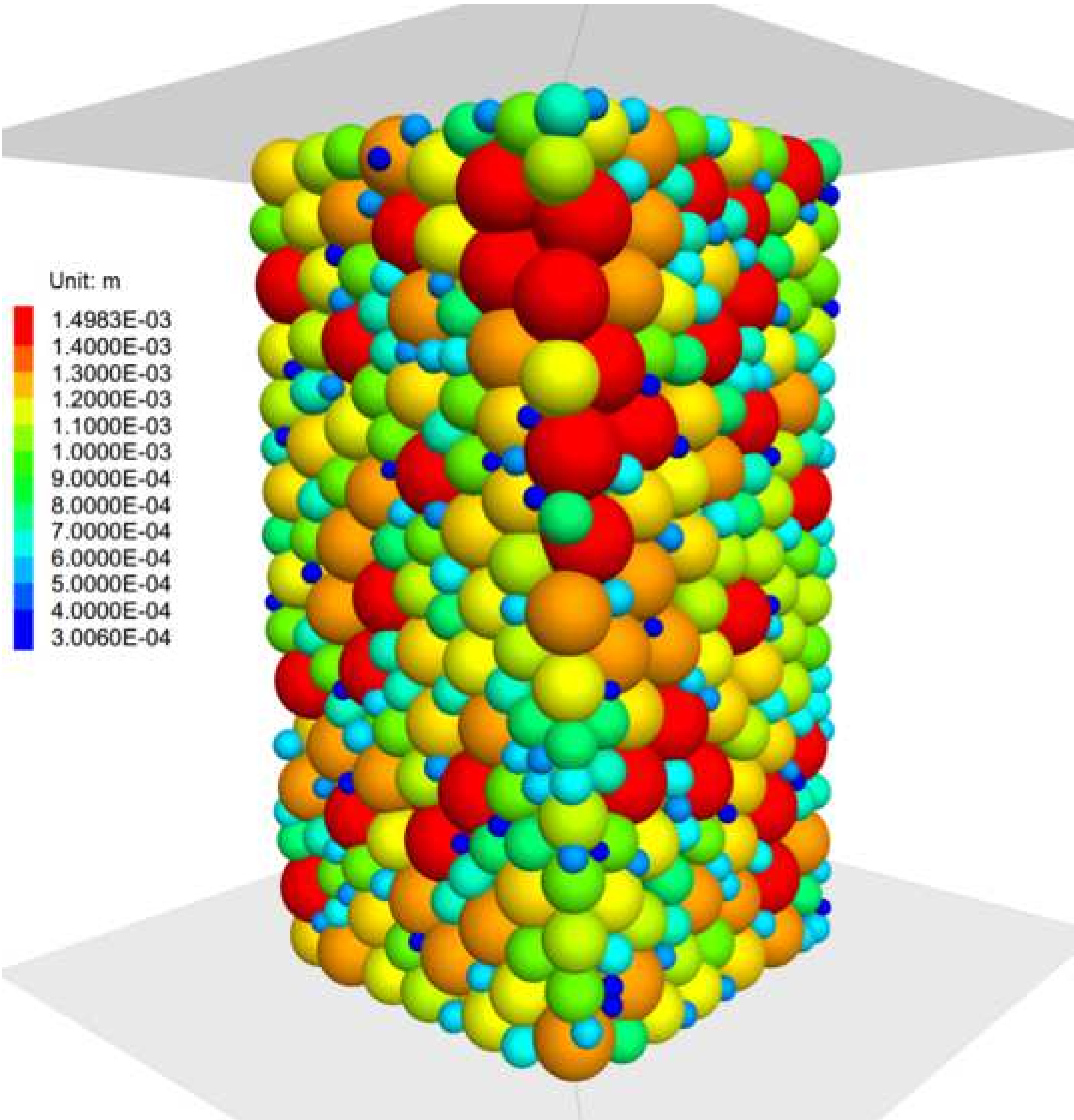
Unit: m
1.4983E-03
1.4000E-03
1.3000E-03
1.2000E-03
1.1000E-03
1.0000E-03
9.0000E-04
8.0000E-04
7.0000E-04
6.0000E-04
5.0000E-04
4.0000E-04
3.0060E-04

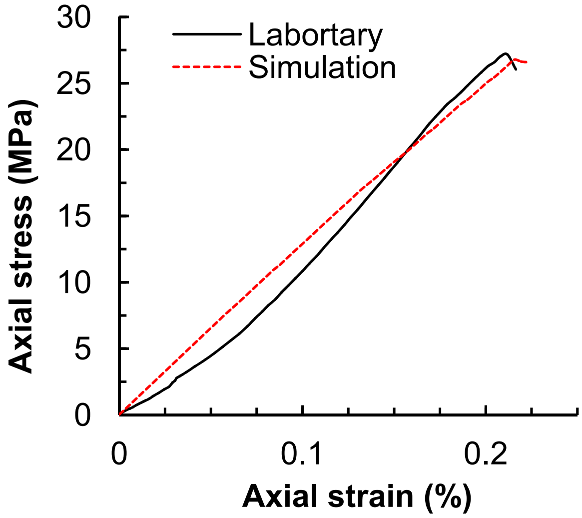

Laborta ry
Simulation
Axial stress (MPa)
30
25
20
15
10
5
0
0
0.1
0.2
Axial strain (%)

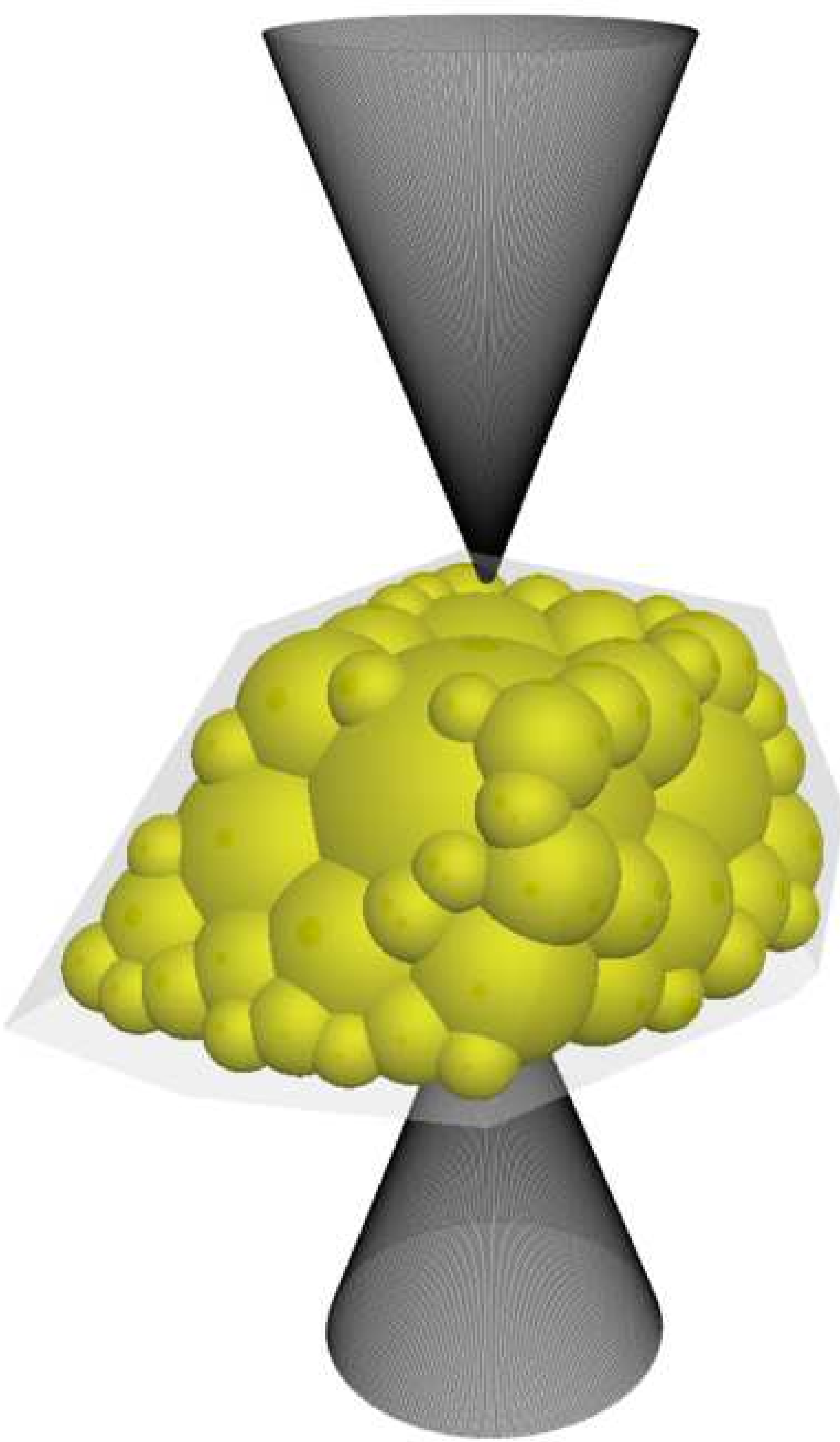

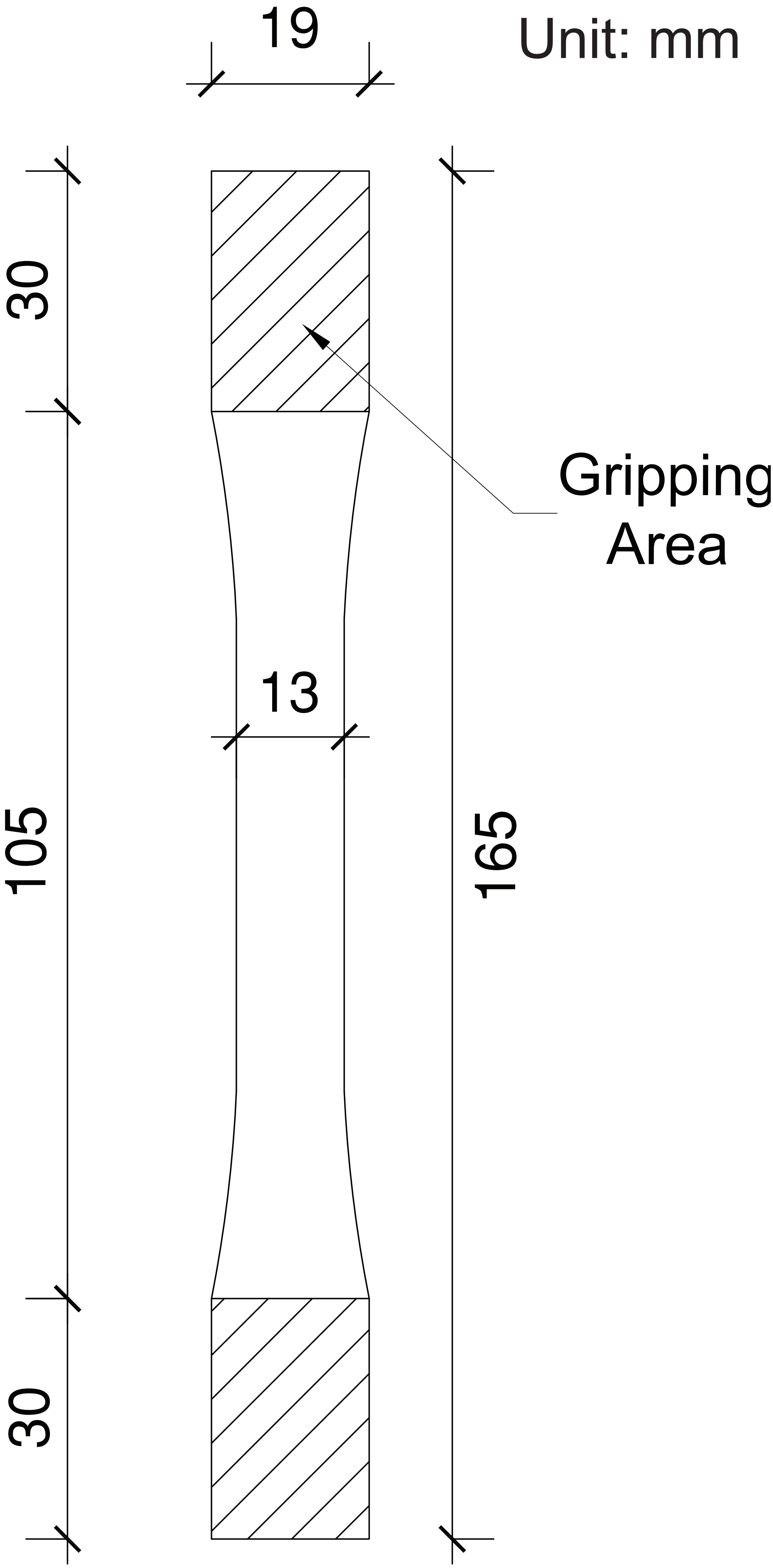
Unit: mm
19
30
105
30
165
13
Gripping
Area

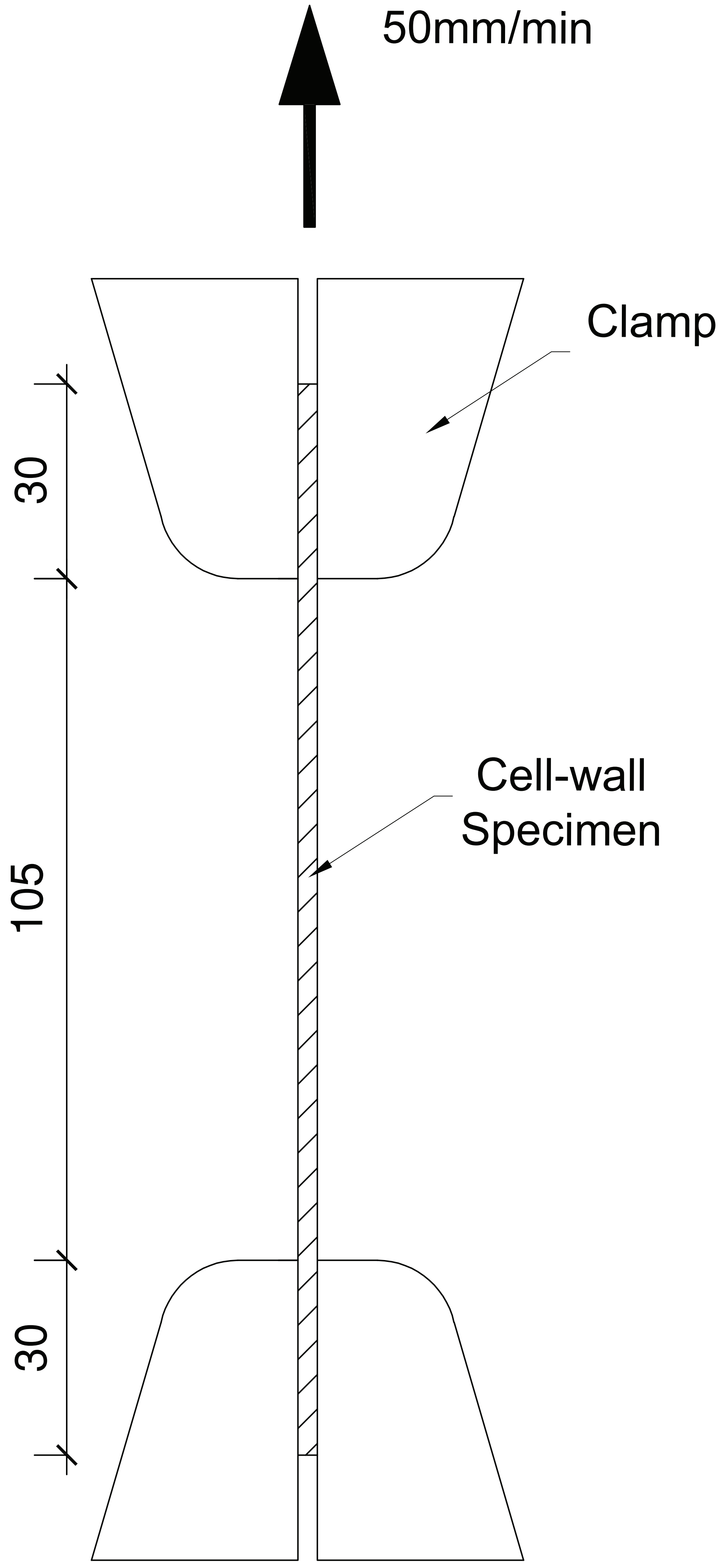
50mm/min
Clamp
Cell-wall
Specimen
30
105
30

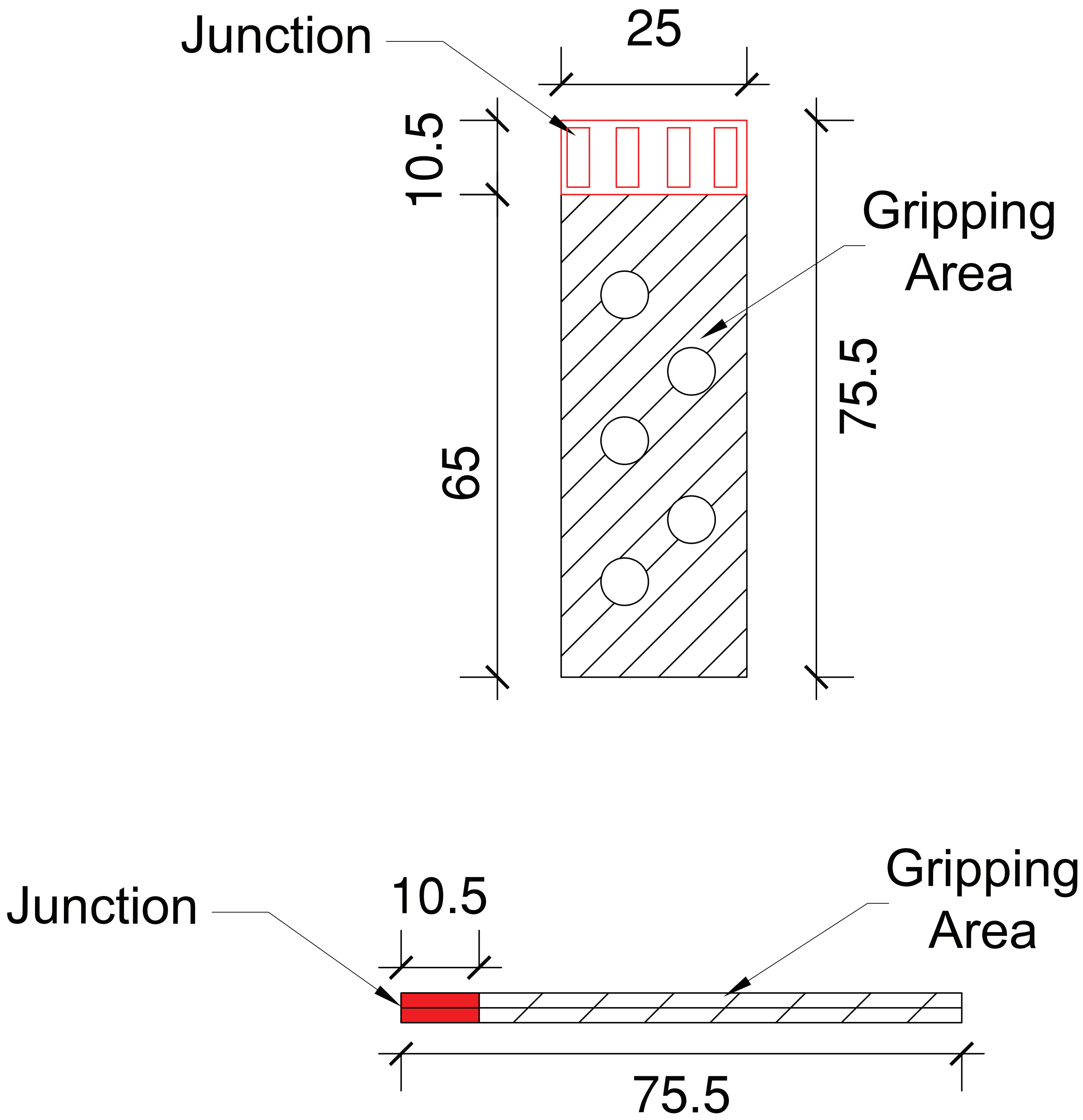
Junction
25
10.5
Gripping
Area
75.5
65
Junction
10.5
Gripping
Area
75.5

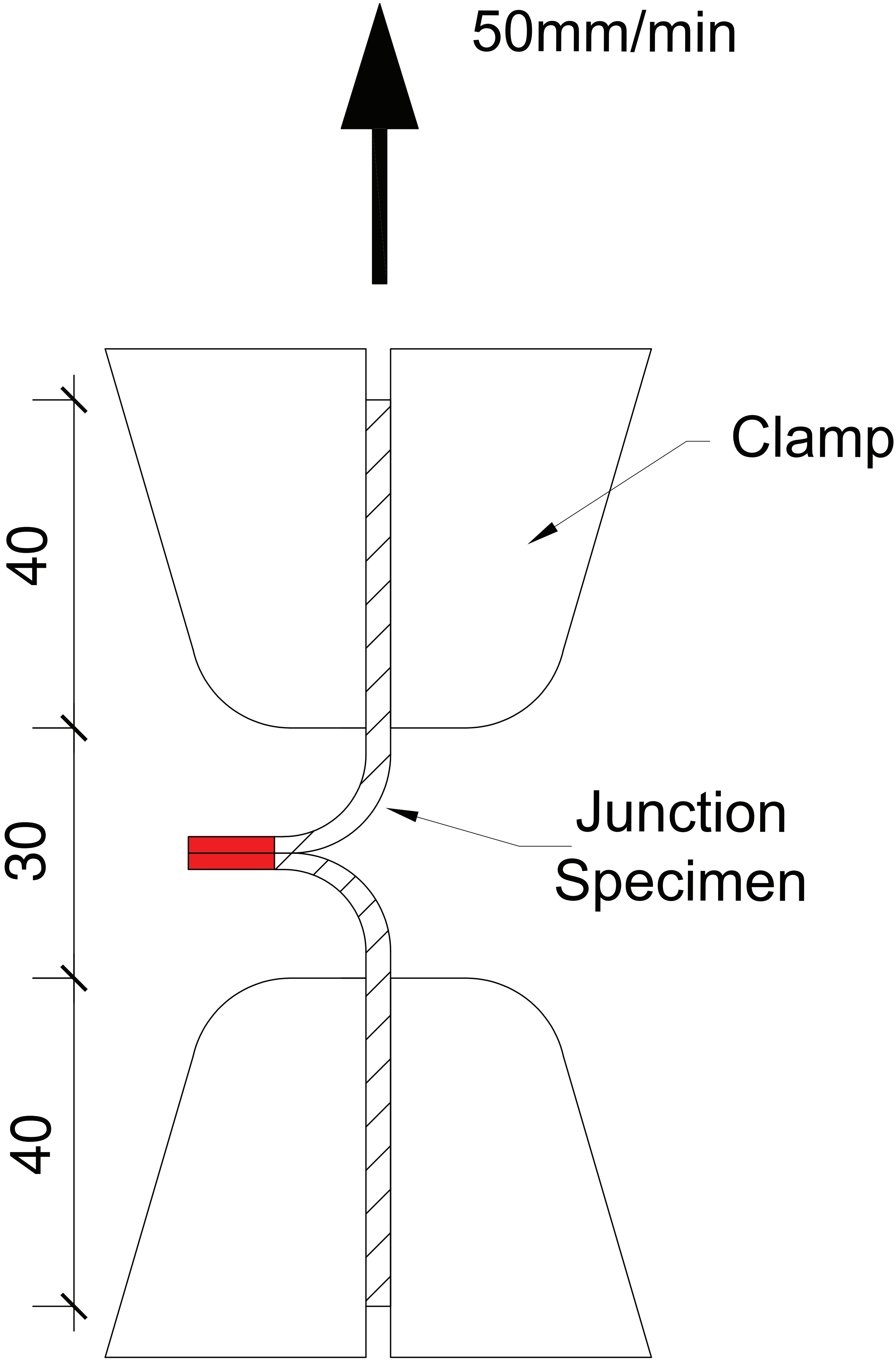
50mm/min
Clamp
Junction
Specimen
40
30
40

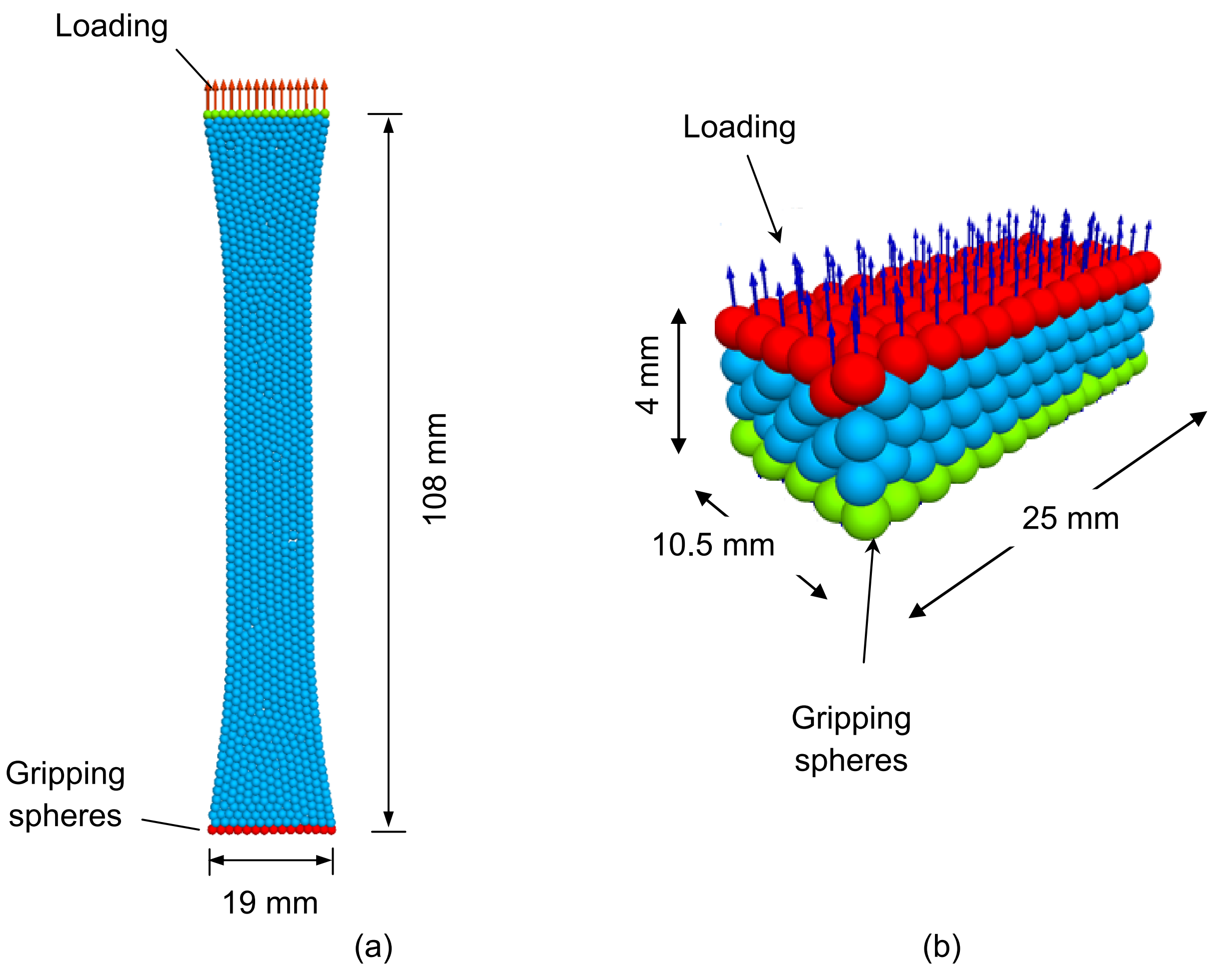
Loading
108 mm
Gripping
spheres
19 mm
(a)
Loading
4 mm
10.5 mm
25 mm
Gripping
spheres
(b)

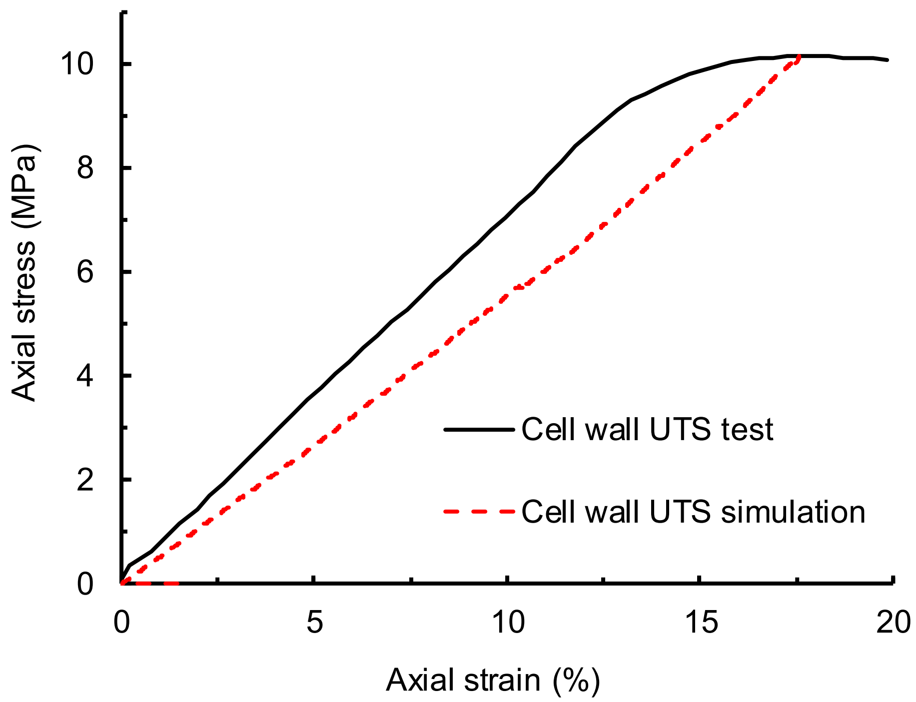

Axial stress (MPa)
0
2
4
6
8
10
0
5
10
15
20
Axial strain (%)
Cell wall UTS test
Cell wall UTS simulation

(a)

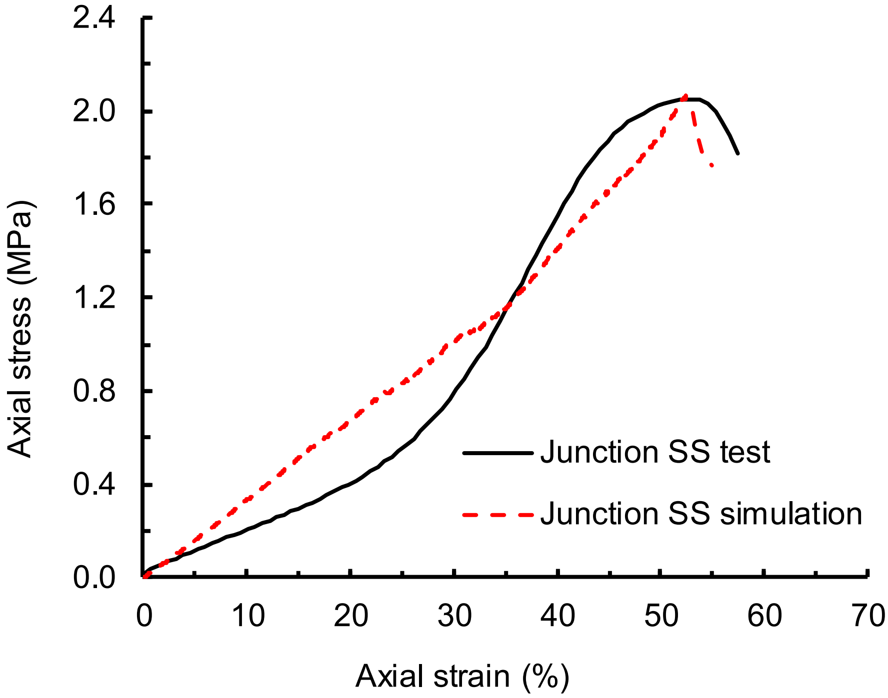

Axial stress (MPa)
2.4
2.0
1.6
1.2
0.8
0.4
0.0
0
10
20
30
40
50
60
70
Axial strain (%)
Junction SS test
Junction SS simulation

(b)

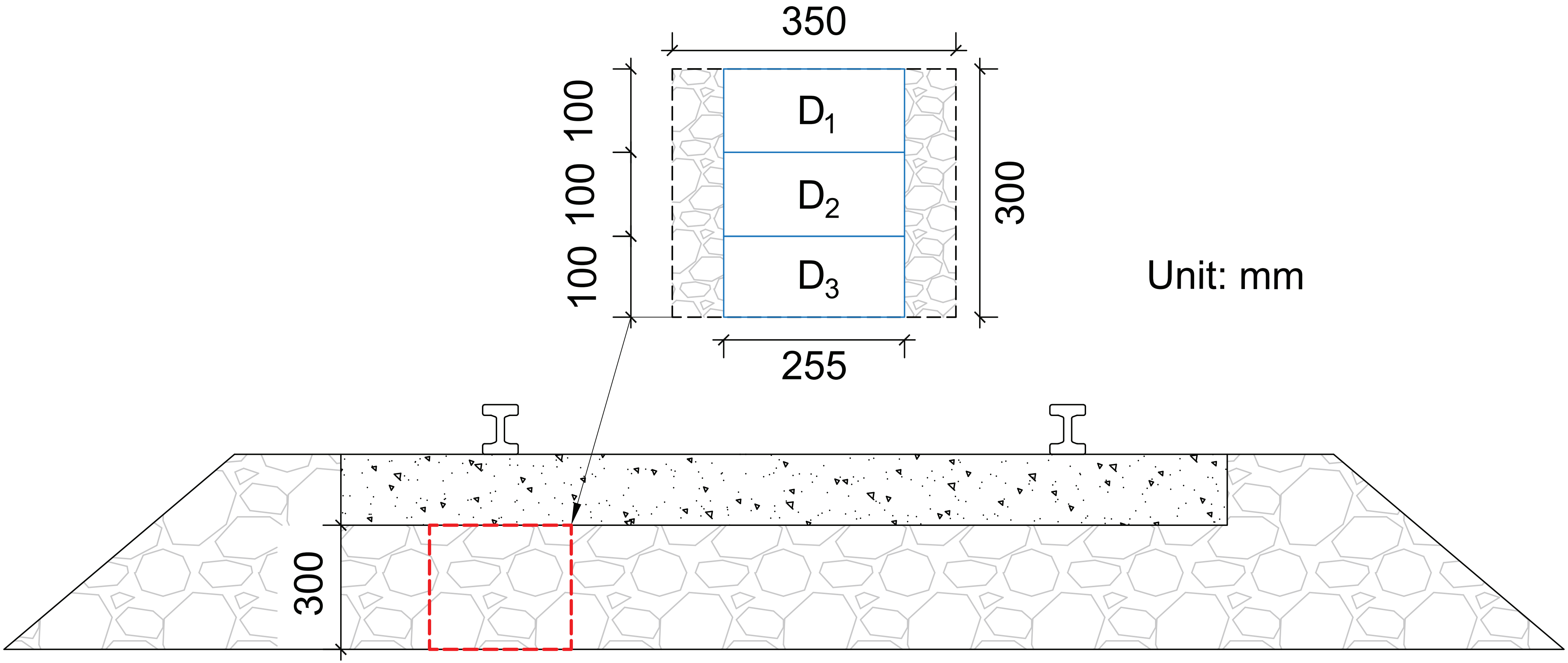
350
100
100
100
D1
D2
D3
300
255
Unit: mm
300

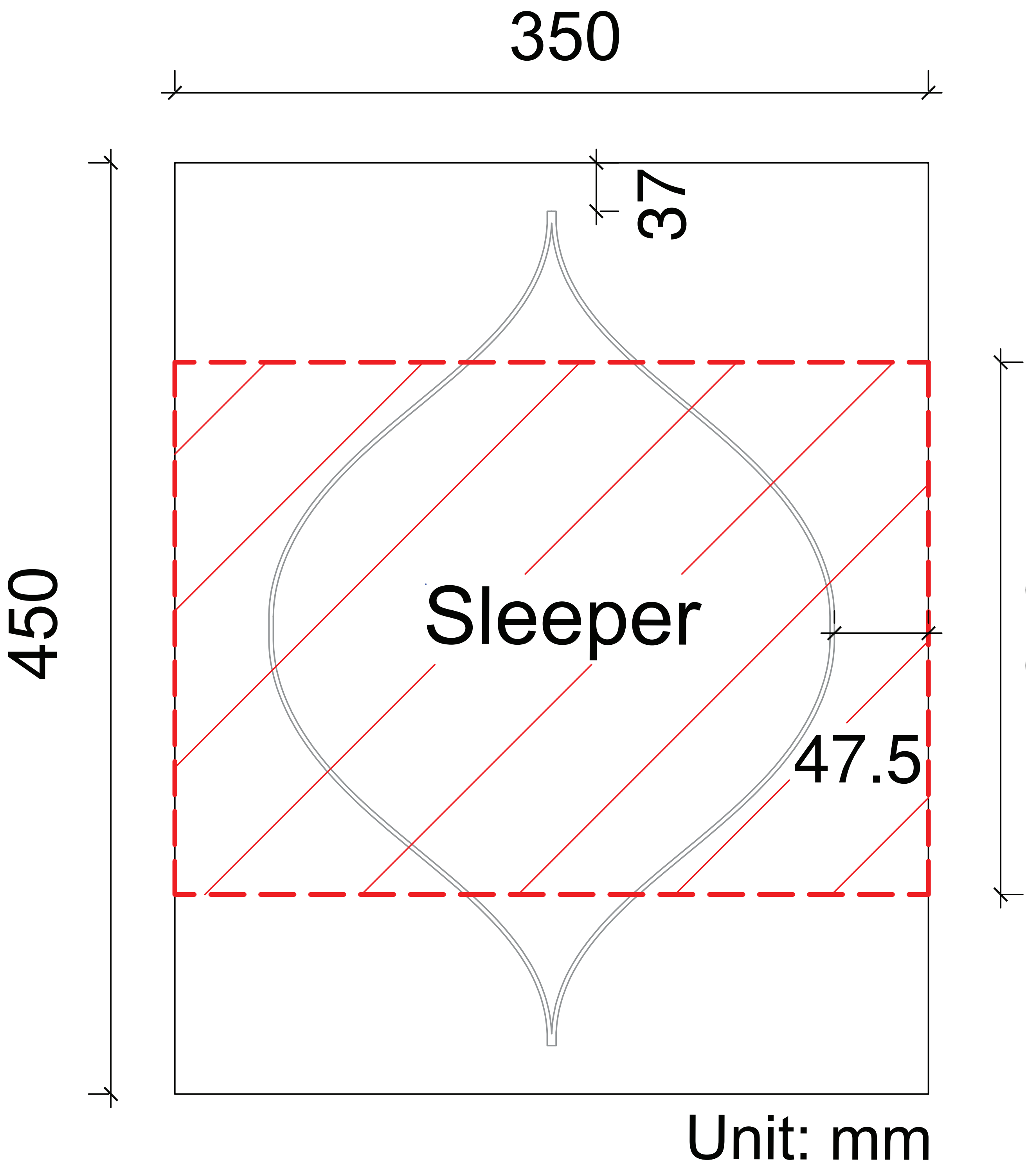
350
37
450
Sleeper
250
47.5
Unit: mm

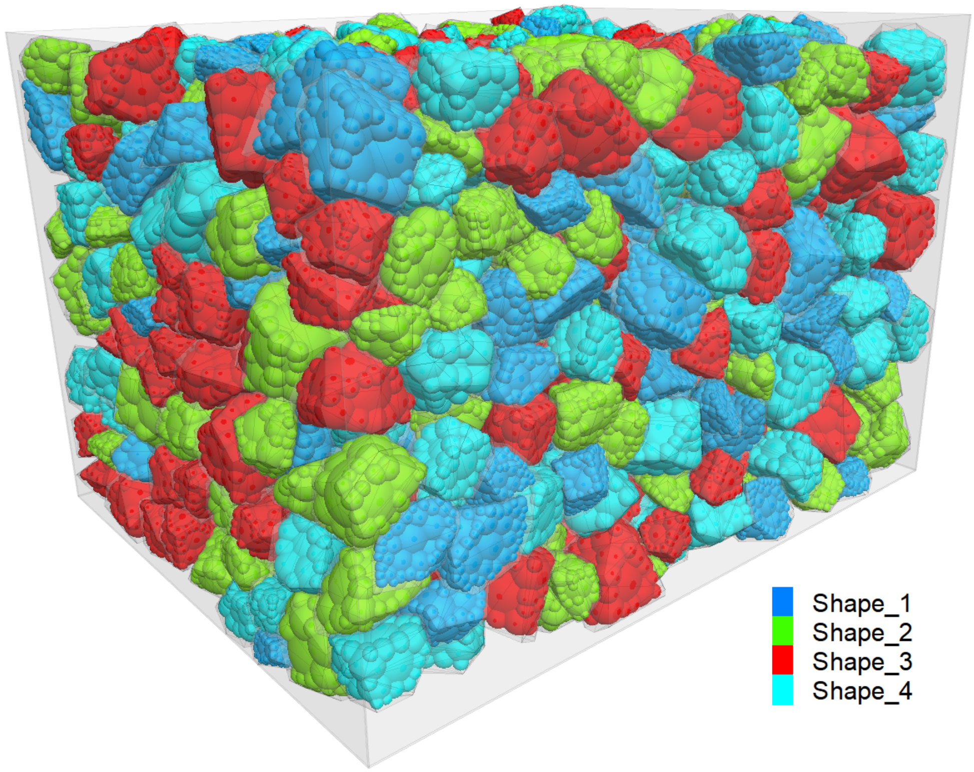

No. of ballast particles: 960

Initial porosity: 0.46

No. of parallel-bonds for the ballast: 110,469

(a)

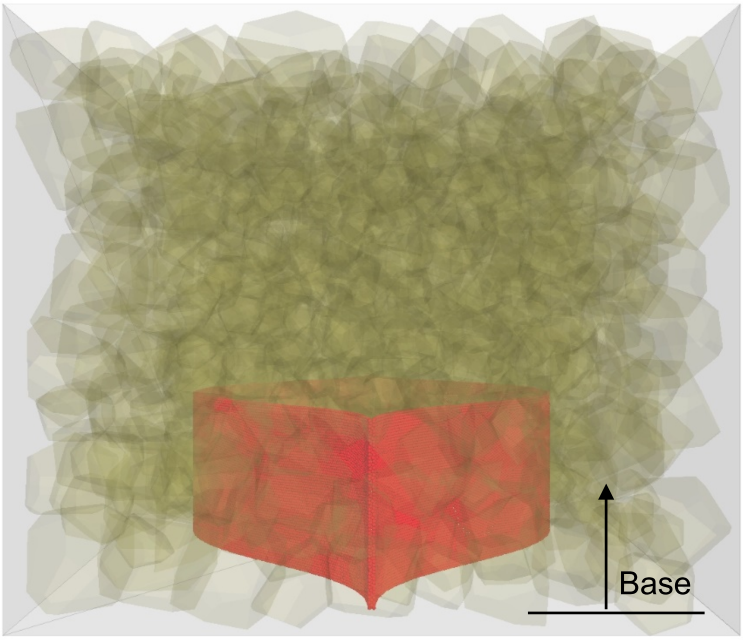

No. of ballast particles: 960
Initial porosity: 0.463
No. of parallel-bonds for: ballast: 110,474; and
geocell: 90,747

(b)

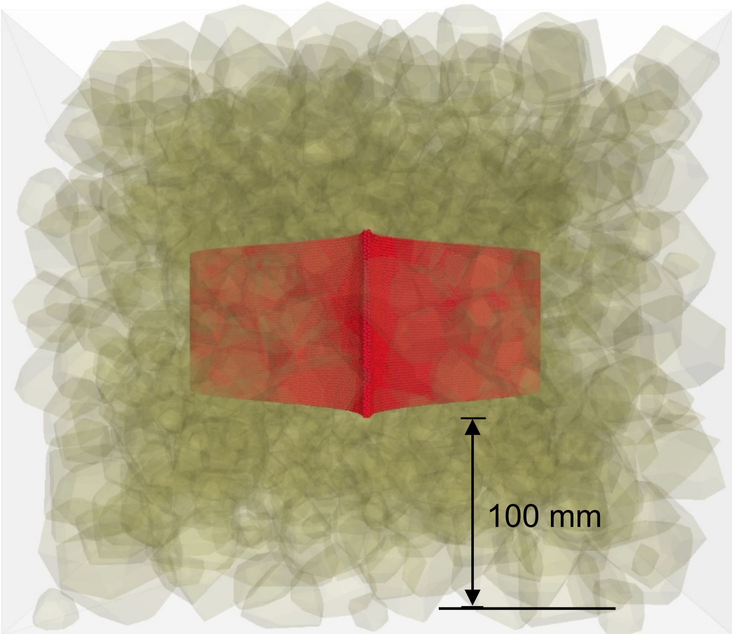

No. of ballast particles: 960
Initial porosity: 0.462
No. of parallel-bonds for: ballast: 110,466; and
geocell: 90,747

(c)

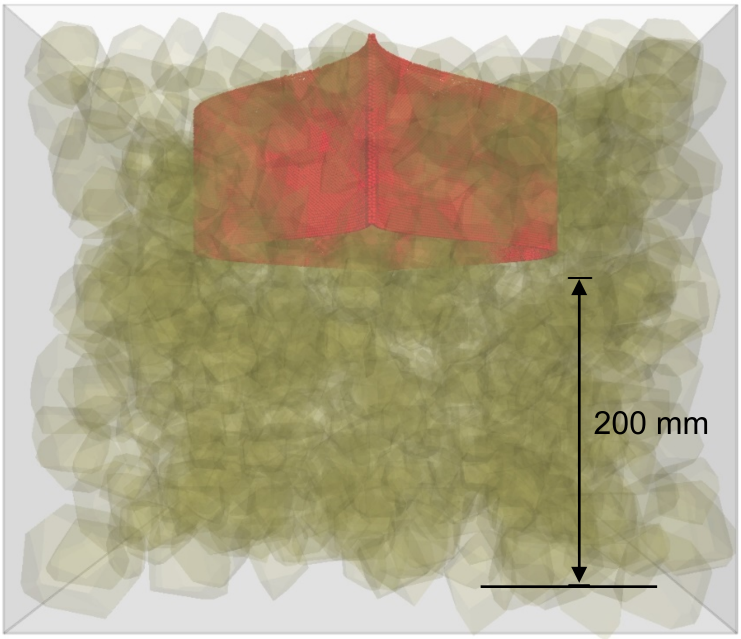

No. of ballast particles: 960
Initial porosity: 0.461
No. of parallel-bonds for: ballast: 110,469 and geocell: 90,747

(d)

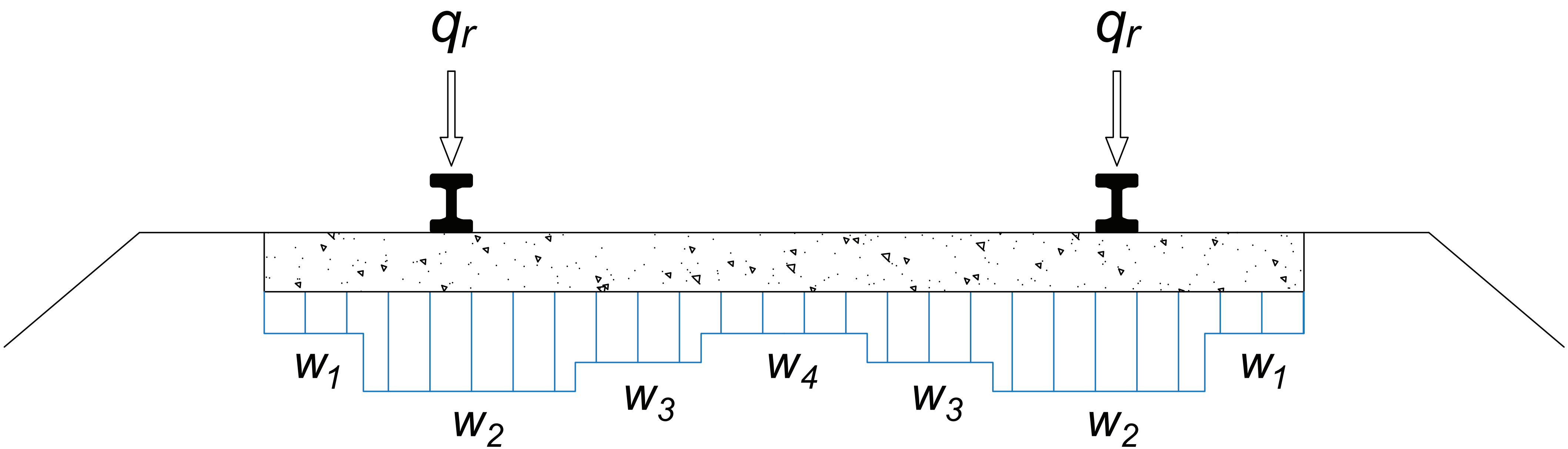

q_r
q_r
w_1
w_2
w_3
w_4
w_3
w_2
w_1

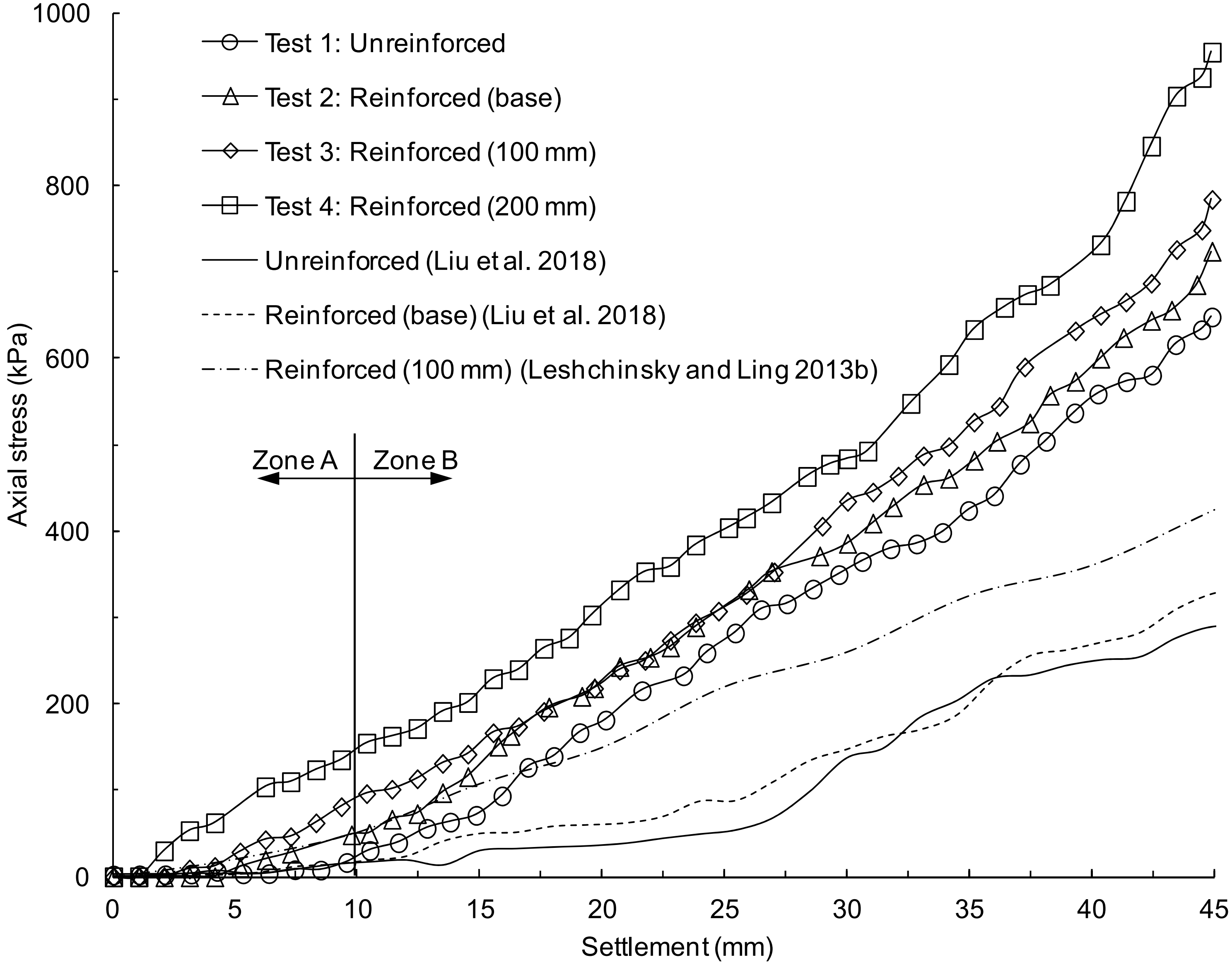

1000
800
600
400
200
0
Axial stress (kPa)
0
5
10
15
20
25
30
35
40
45
Settlement (mm)
Test 1: Unreinforced
Test 2: Reinforced (base)
Test 3: Reinforced (100 mm)
Test 4: Reinforced (200 mm)
Unreinforced (Liu et al. 2018)
Reinforced (base) (Liu et al. 2018)
Reinforced (100 mm) (Leshchinsky and Ling 2013b)
Zone A
Zone B

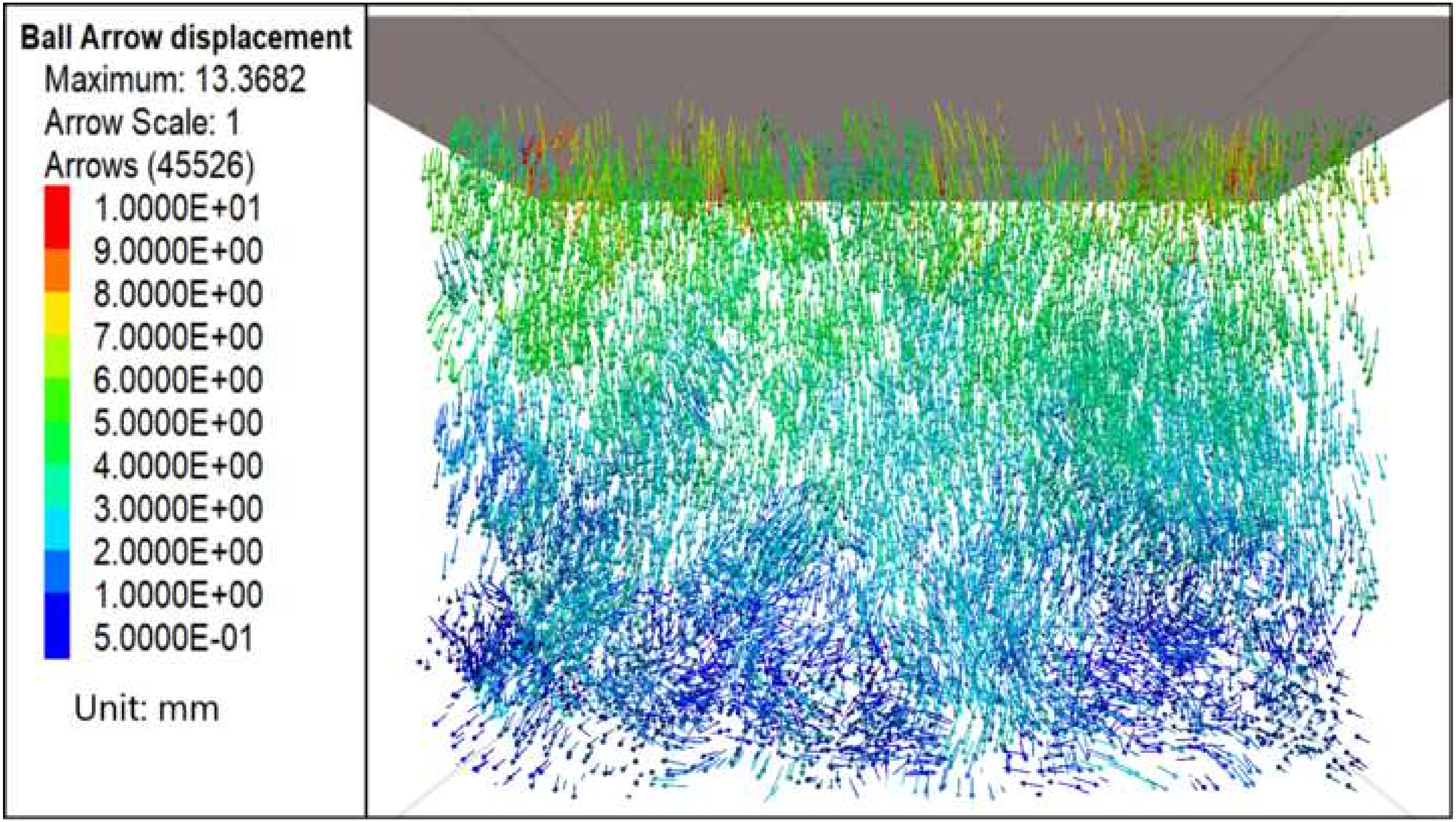
Ball Arrow displacement
Maximum: 13.3682
Arrow Scale: 1
Arrows (45526)
1.0000E+01
9.0000E+00
8.0000E+00
7.0000E+00
6.0000E+00
5.0000E+00
4.0000E+00
3.0000E+00
2.0000E+00
1.0000E+00
5.0000E-01
Unit: mm

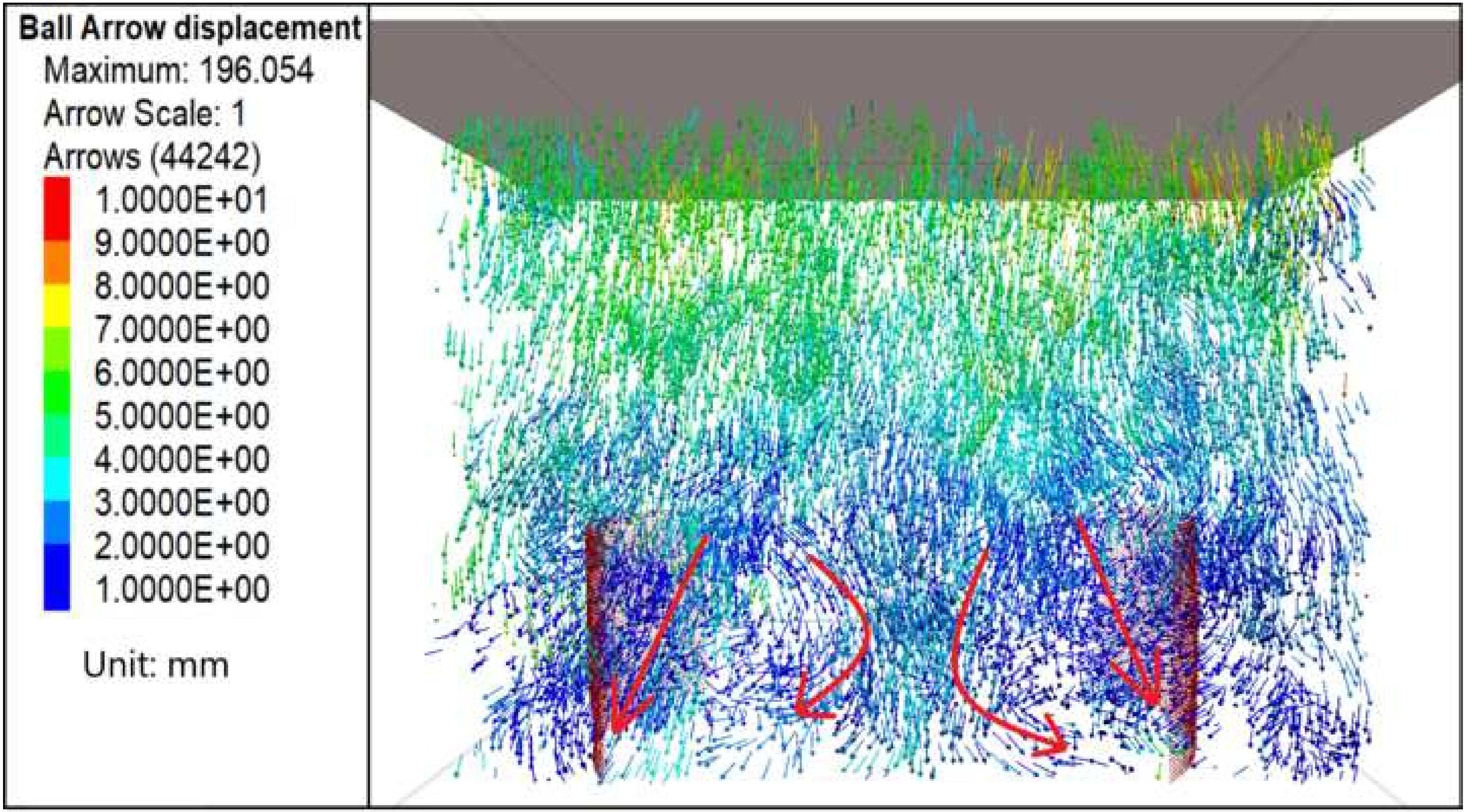
Ball Arrow displacement
Maximum: 196.054
Arrow Scale: 1
Arrows (44242)
1.0000E+01
9.0000E+00
8.0000E+00
7.0000E+00
6.0000E+00
5.0000E+00
4.0000E+00
3.0000E+00
2.0000E+00
1.0000E+00
Unit: mm

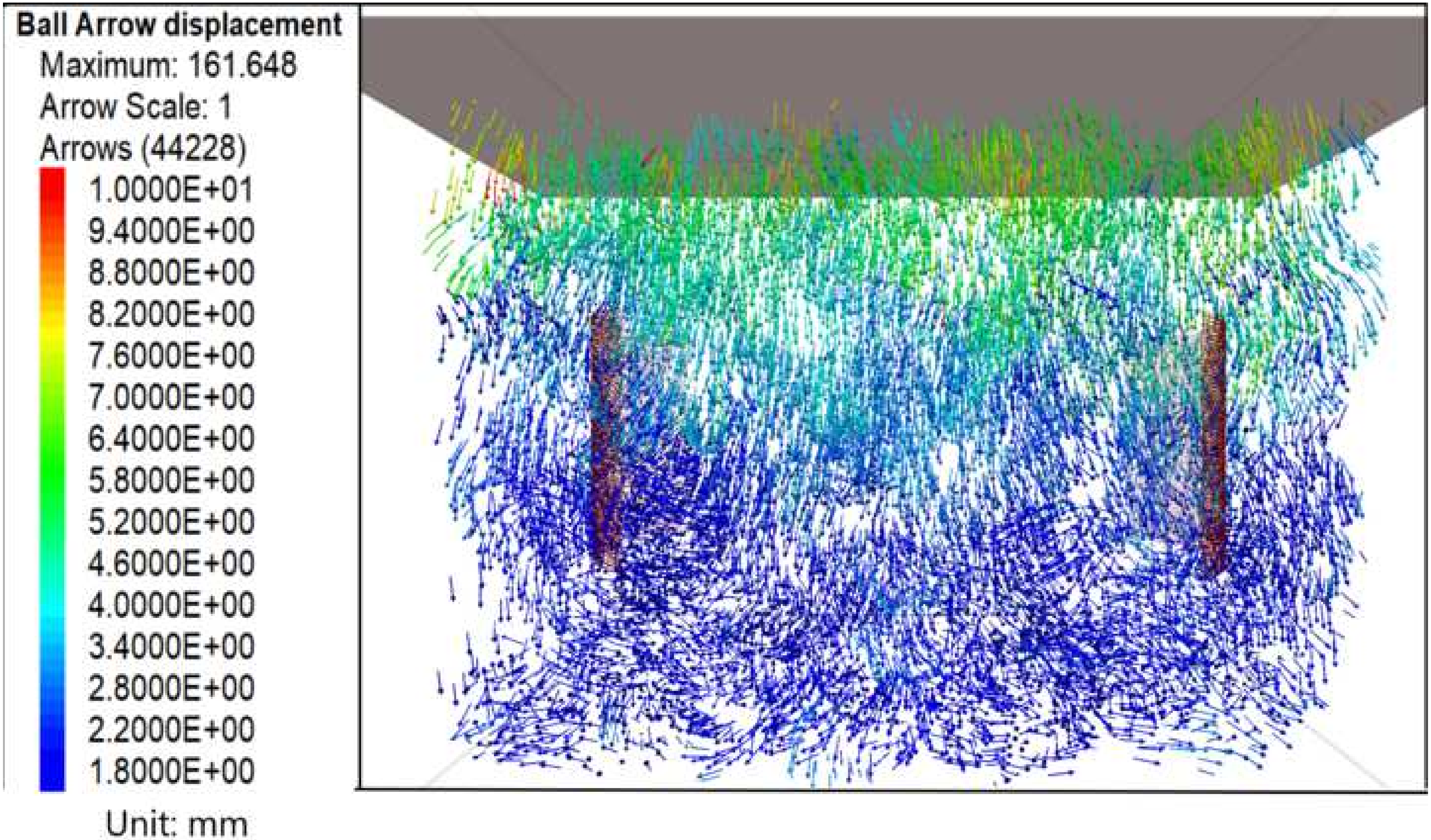
Ball Arrow displacement
Maximum: 161.648
Arrow Scale: 1
Arrows (44228)
1.0000E+01
9.4000E+00
8.8000E+00
8.2000E+00
7.6000E+00
7.0000E+00
6.4000E+00
5.8000E+00
5.2000E+00
4.6000E+00
4.0000E+00
3.4000E+00
2.8000E+00
2.2000E+00
1.8000E+00
Unit: mm

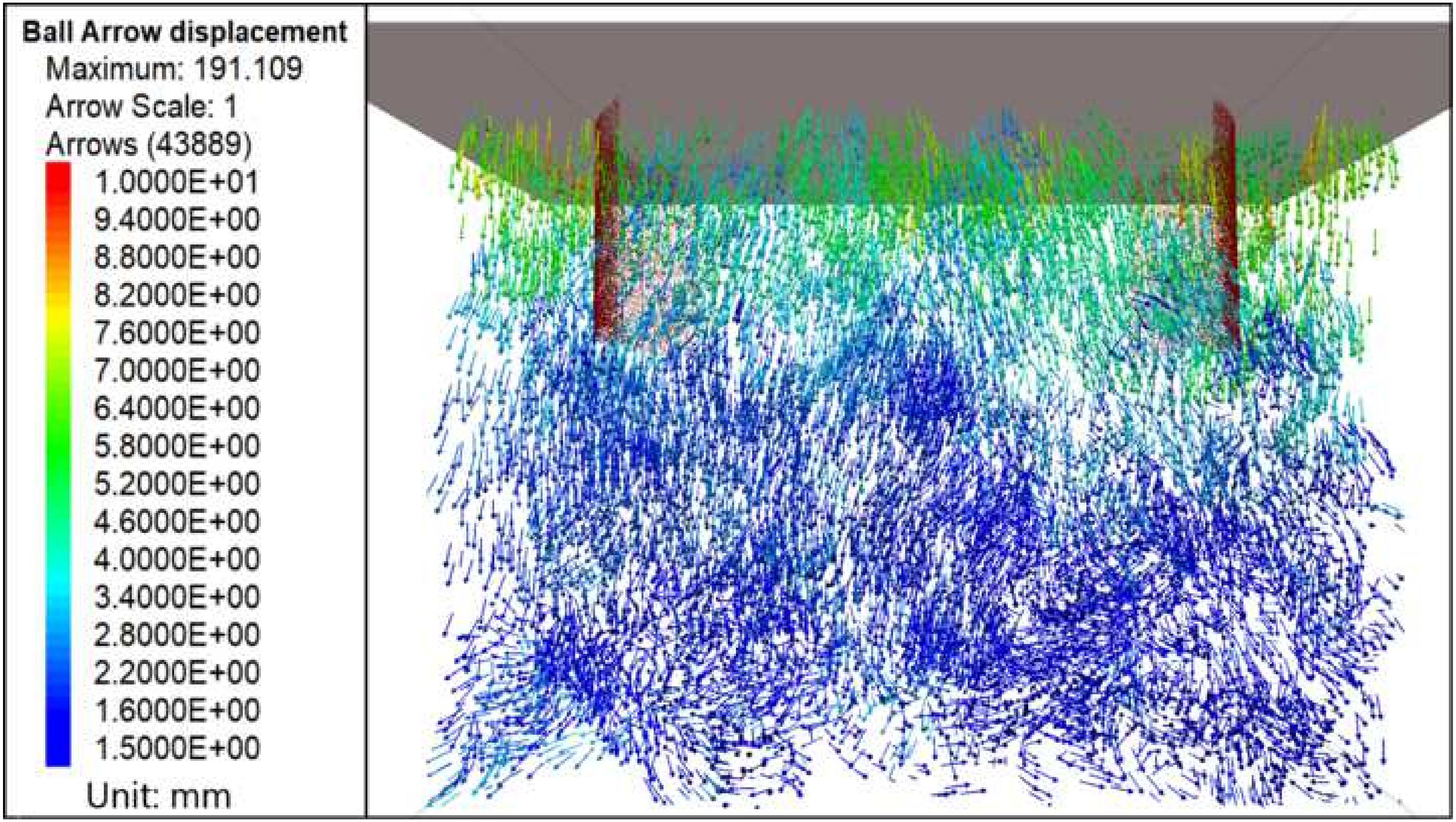
Ball Arrow displacement
Maximum: 191.109
Arrow Scale: 1
Arrows (43889)
1.0000E+01
9.4000E+00
8.8000E+00
8.2000E+00
7.6000E+00
7.0000E+00
6.4000E+00
5.8000E+00
5.2000E+00
4.6000E+00
4.0000E+00
3.4000E+00
2.8000E+00
2.2000E+00
1.6000E+00
1.5000E+00
Unit: mm

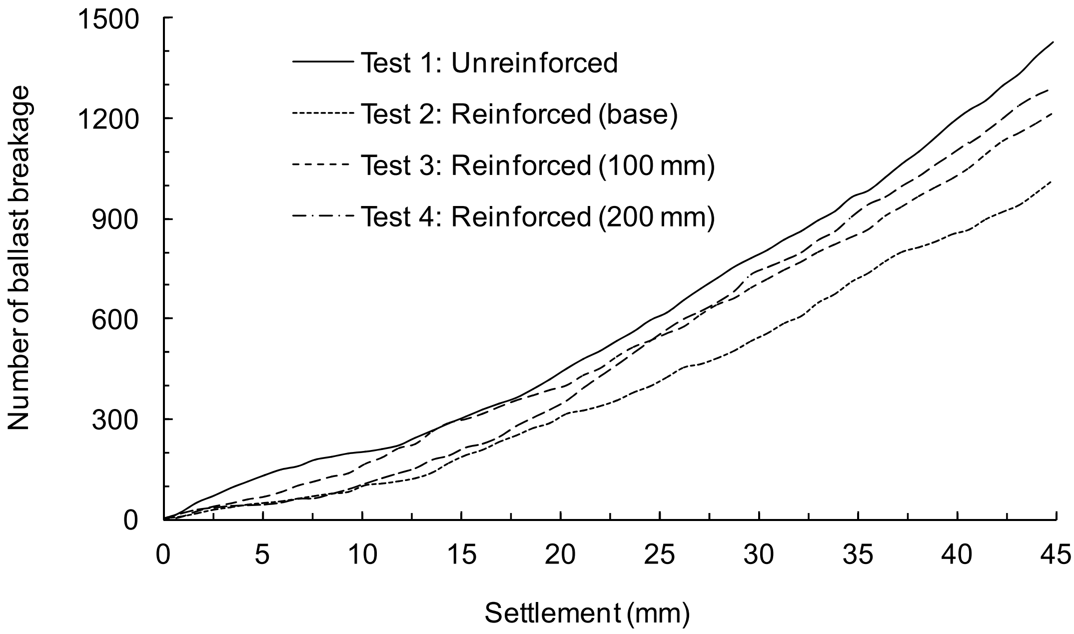
Number of ballast breakage
1500
1200
900
600
300
0
0
5
10
15
20
25
30
35
40
45
Settlement (mm)
Test 1: Unreinforced
Test 2: Reinforced (base)
Test 3: Reinforced (100 mm)
Test 4: Reinforced (200 mm)

Click here to access/download;Figure;Fig 18a.tiff

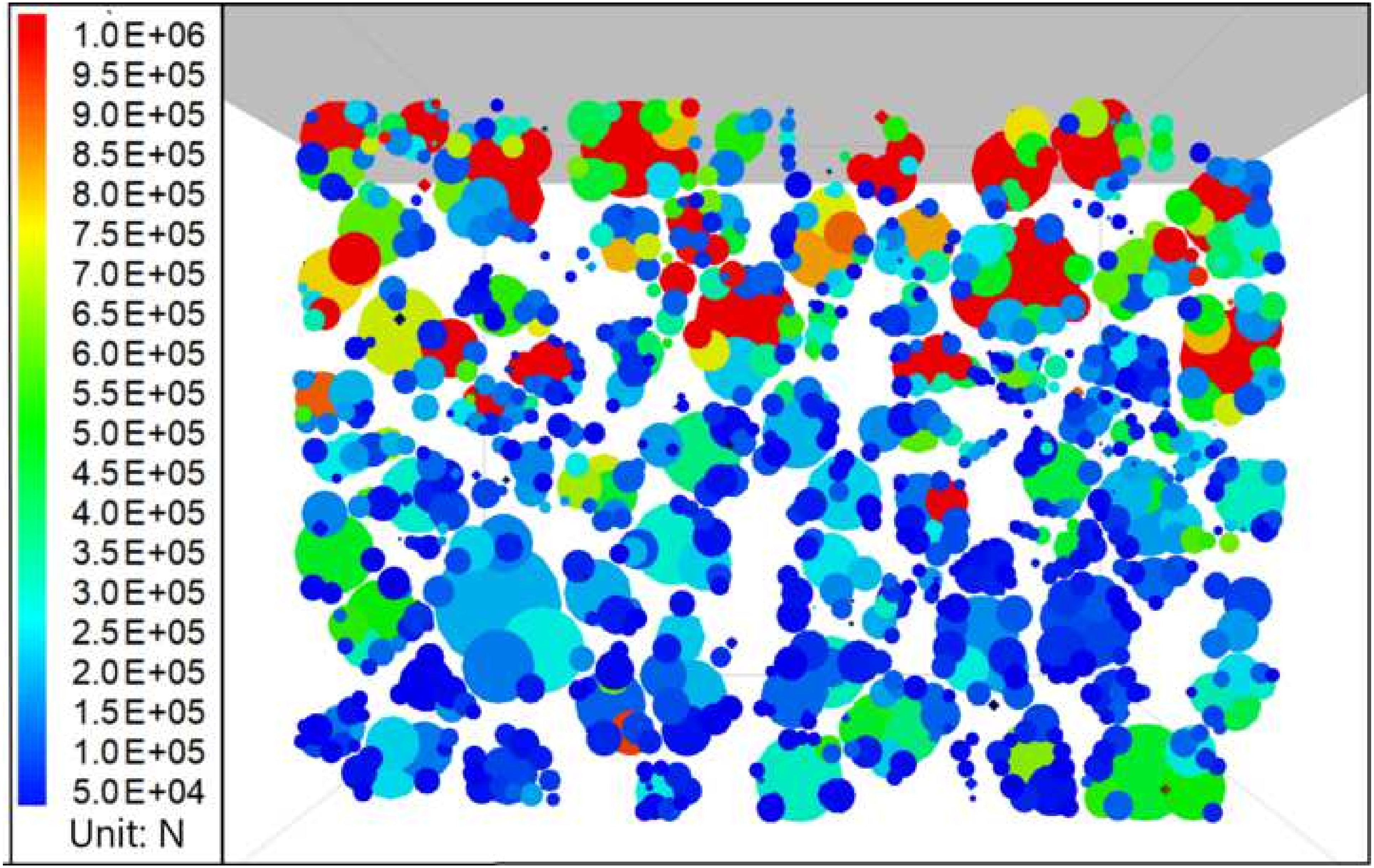

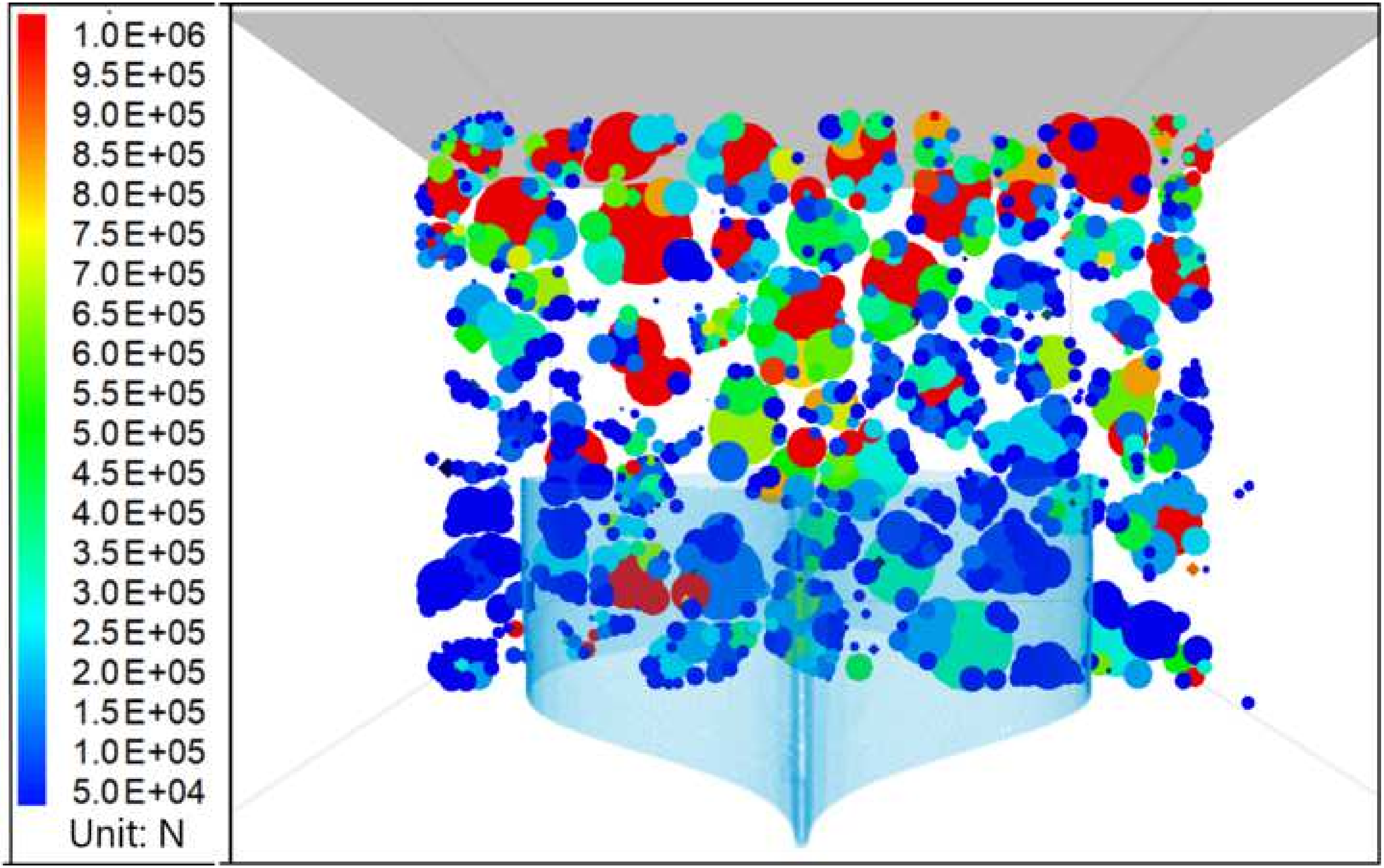
1.0E+06
9.5E+05
9.0E+05
8.5E+05
8.0E+05
7.5E+05
7.0E+05
6.5E+05
6.0E+05
5.5E+05
5.0E+05
4.5E+05
4.0E+05
3.5E+05
3.0E+05
2.5E+05
2.0E+05
1.5E+05
1.0E+05
5.0E+04
Unit: N

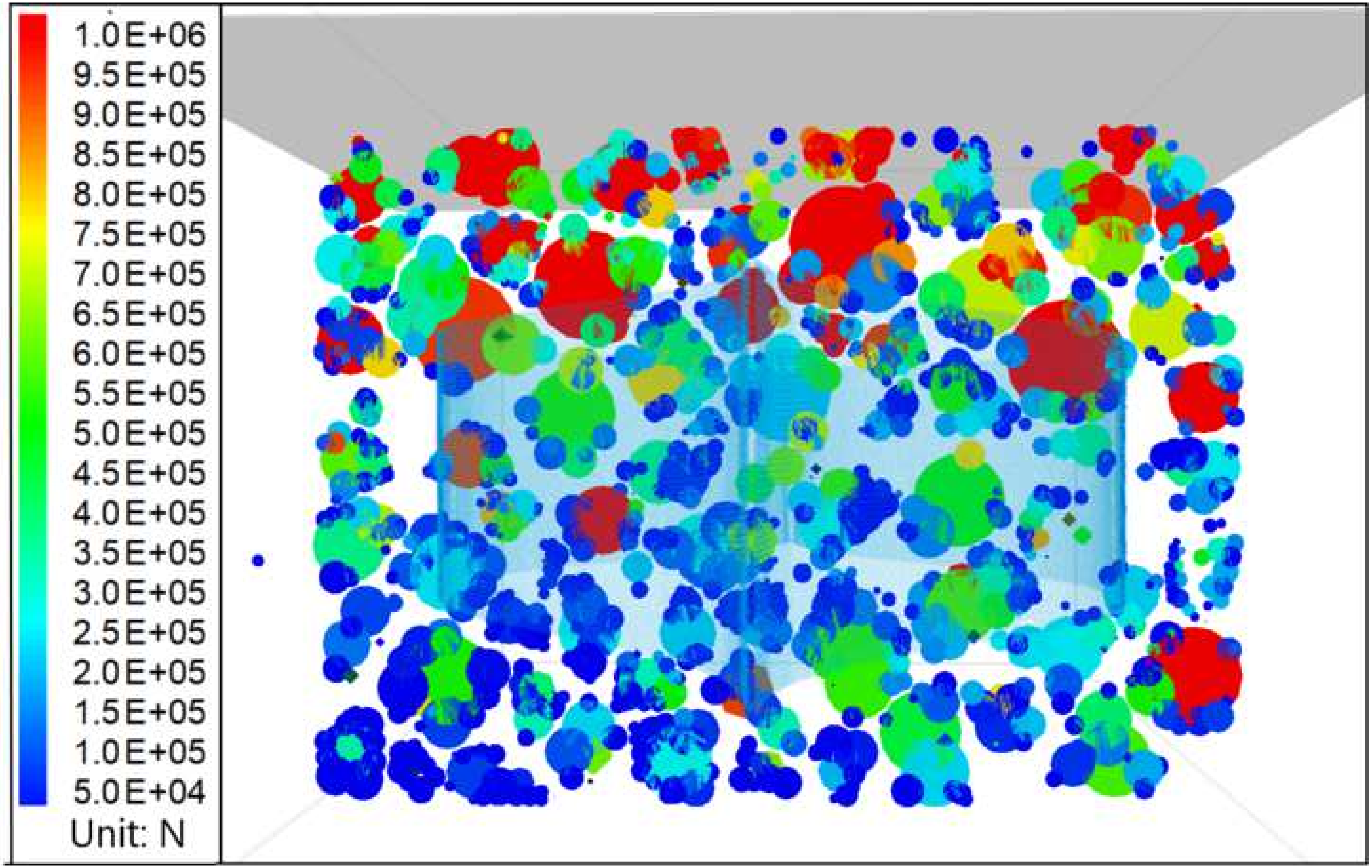
1.0E+06
9.5E+05
9.0E+05
8.5E+05
8.0E+05
7.5E+05
7.0E+05
6.5E+05
6.0E+05
5.5E+05
5.0E+05
4.5E+05
4.0E+05
3.5E+05
3.0E+05
2.5E+05
2.0E+05
1.5E+05
1.0E+05
5.0E+04
Unit: N

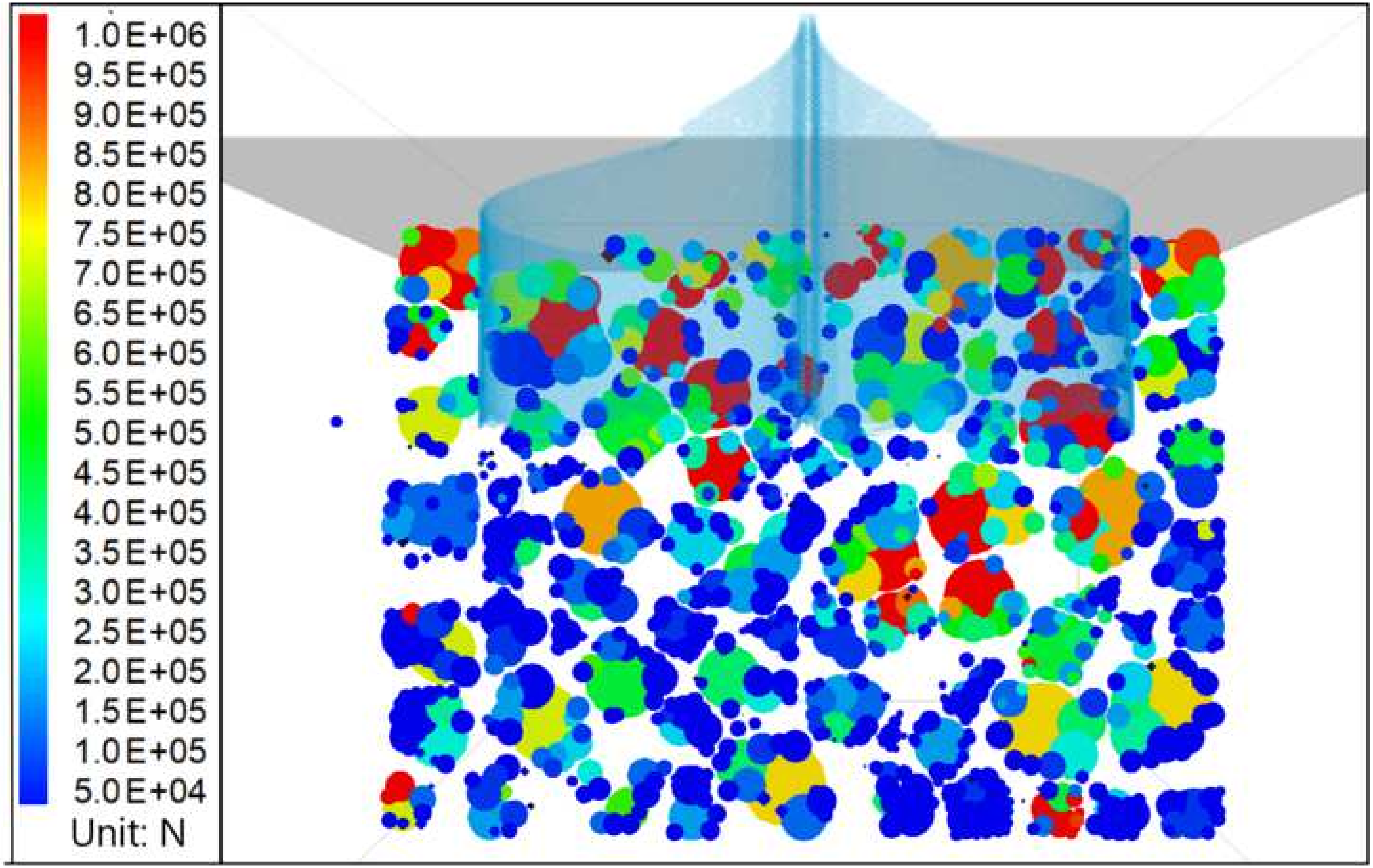
1.0E+06
9.5E+05
9.0E+05
8.5E+05
8.0E+05
7.5E+05
7.0E+05
6.5E+05
6.0E+05
5.5E+05
5.0E+05
4.5E+05
4.0E+05
3.5E+05
3.0E+05
2.5E+05
2.0E+05
1.5E+05
1.0E+05
5.0E+04
Unit: N

Click here to access/download;Figure;Fig 19a.tiff

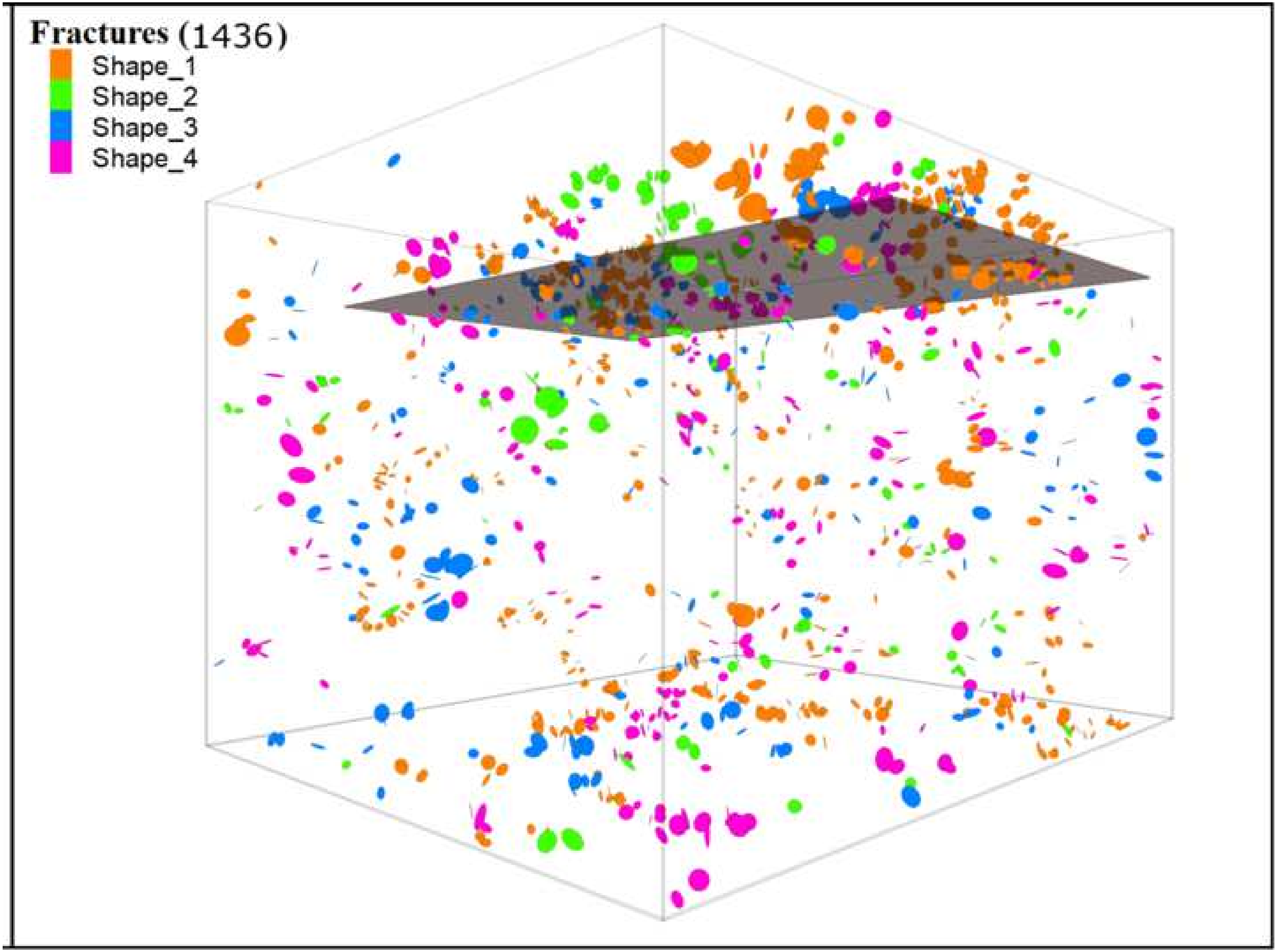

Click here to access/download;Figure;Fig 19b.tiff

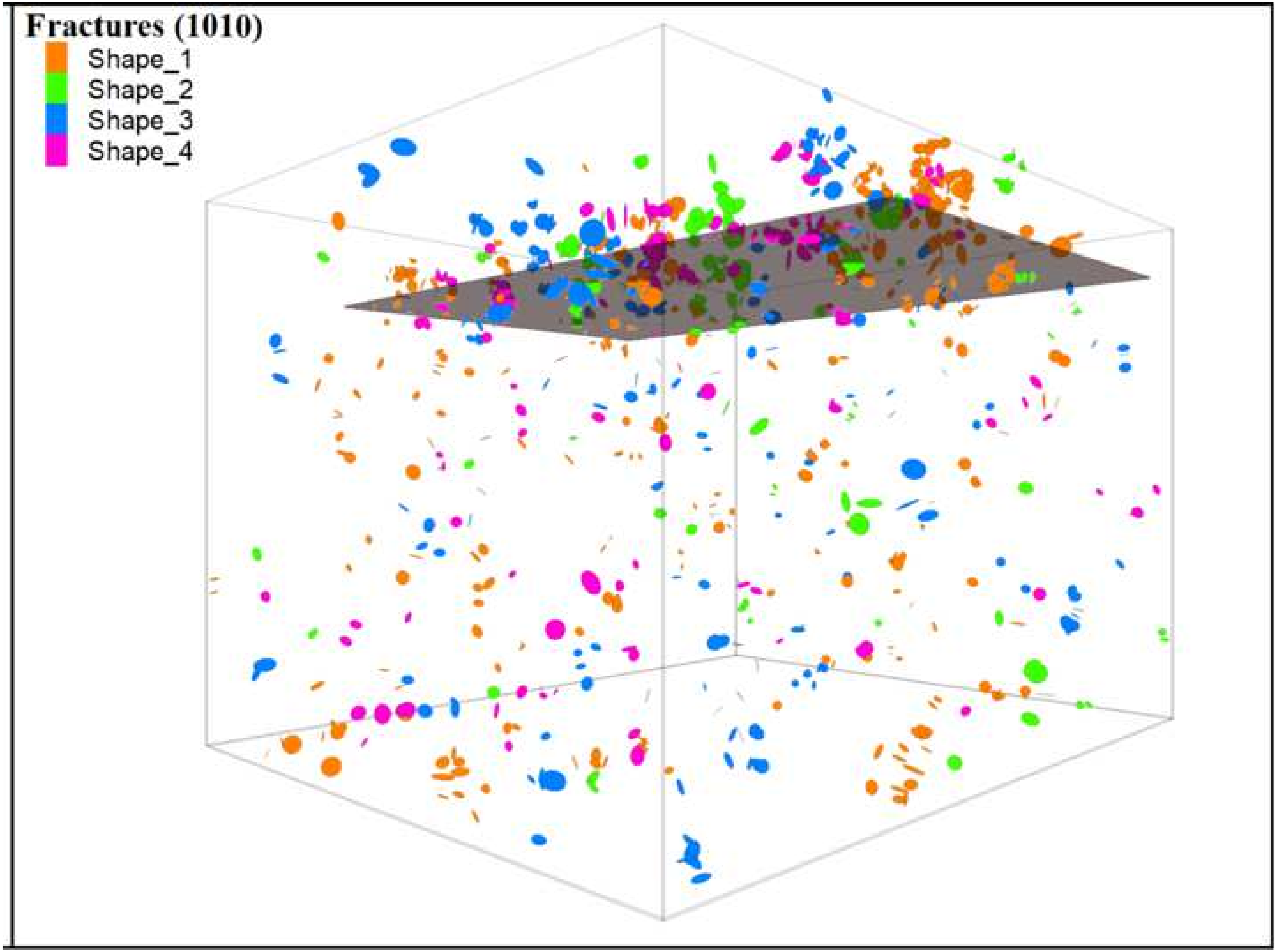

Click here to access/download;Figure;Fig 19c.tiff

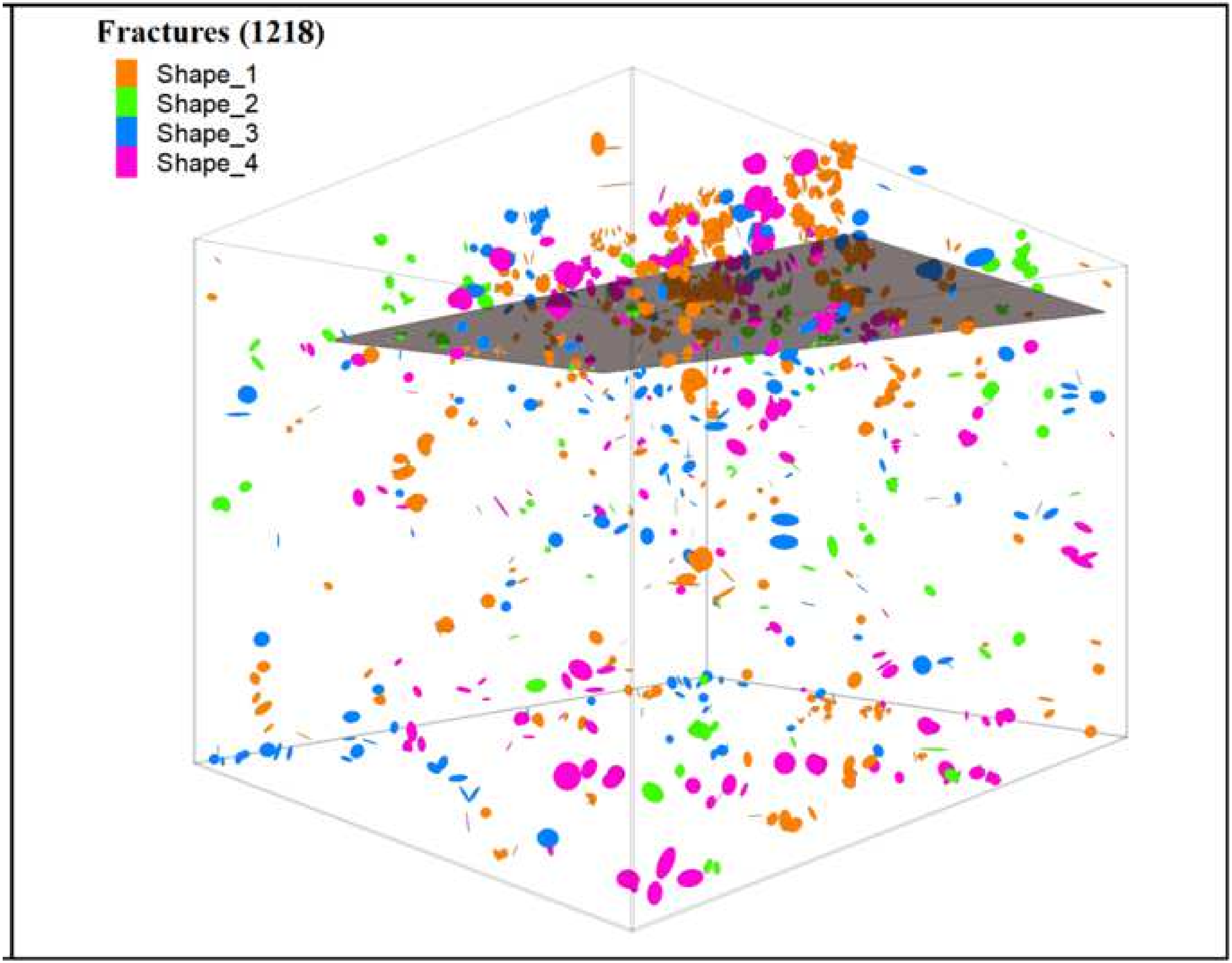

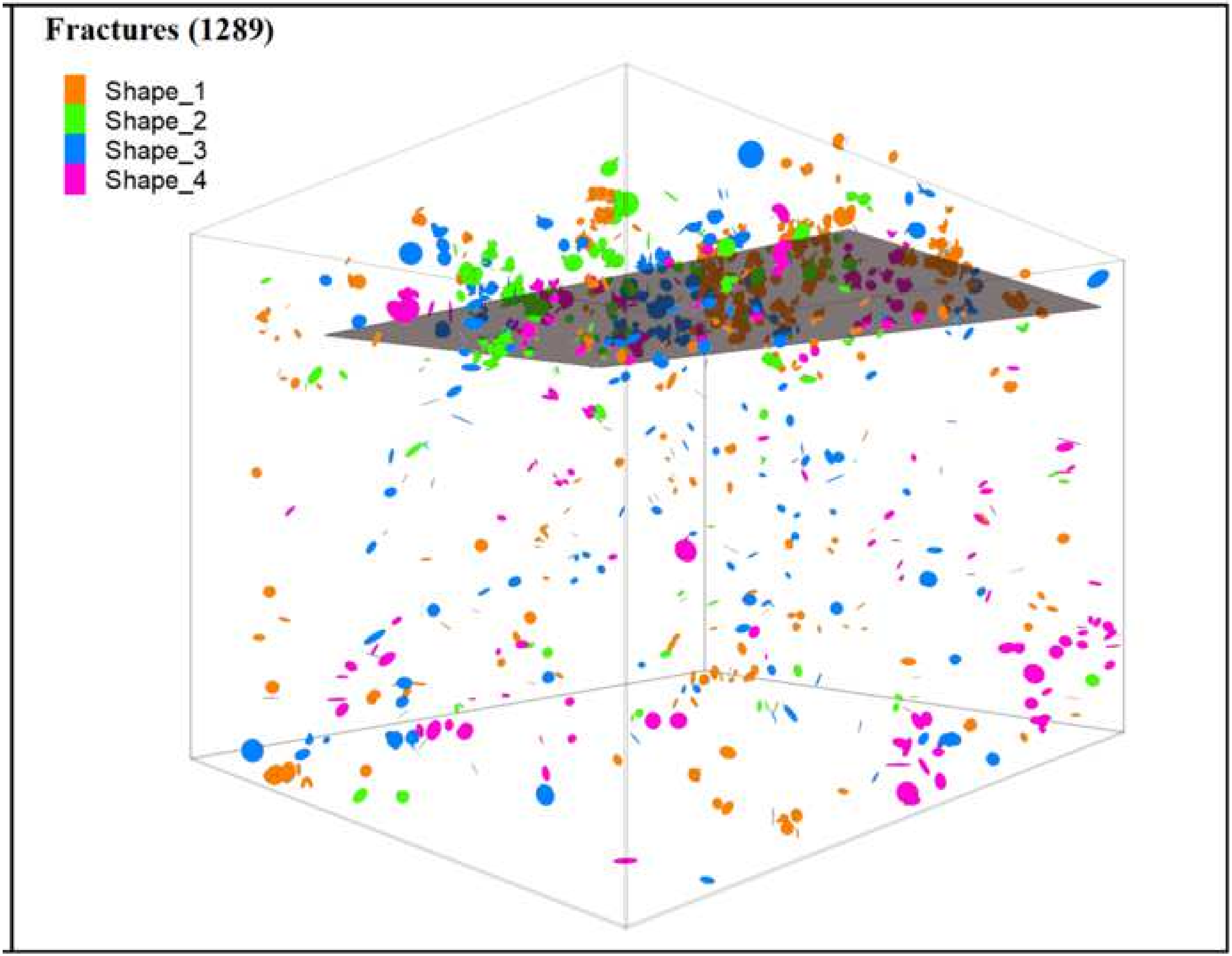
Fractures (1289)
Shape_1
Shape_2
Shape_3
Shape_4

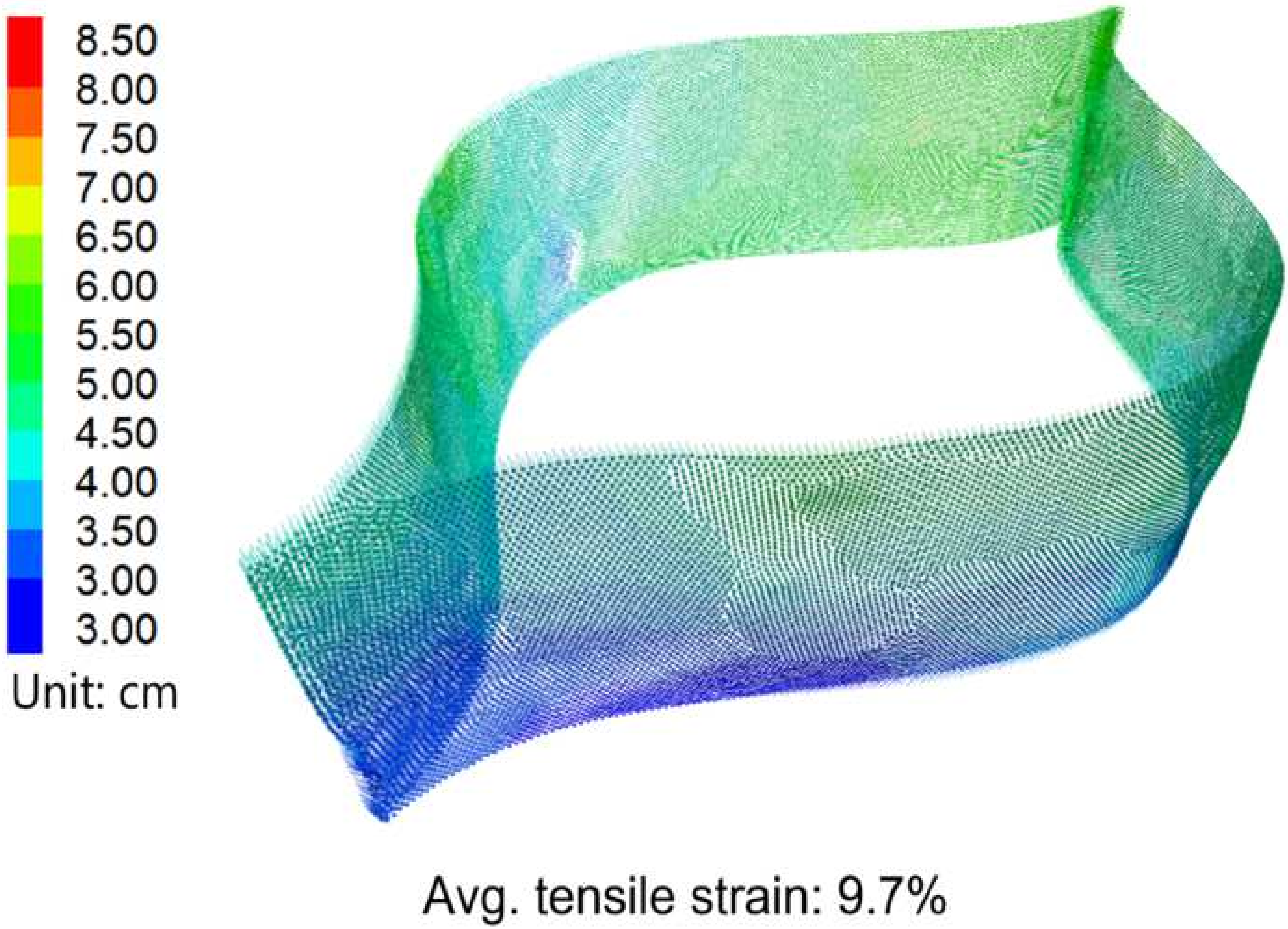
8.50
8.00
7.50
7.00
6.50
6.00
5.50
5.00
4.50
4.00
3.50
3.00
3.00
Unit: cm
Avg. tensile strain: 9.7%

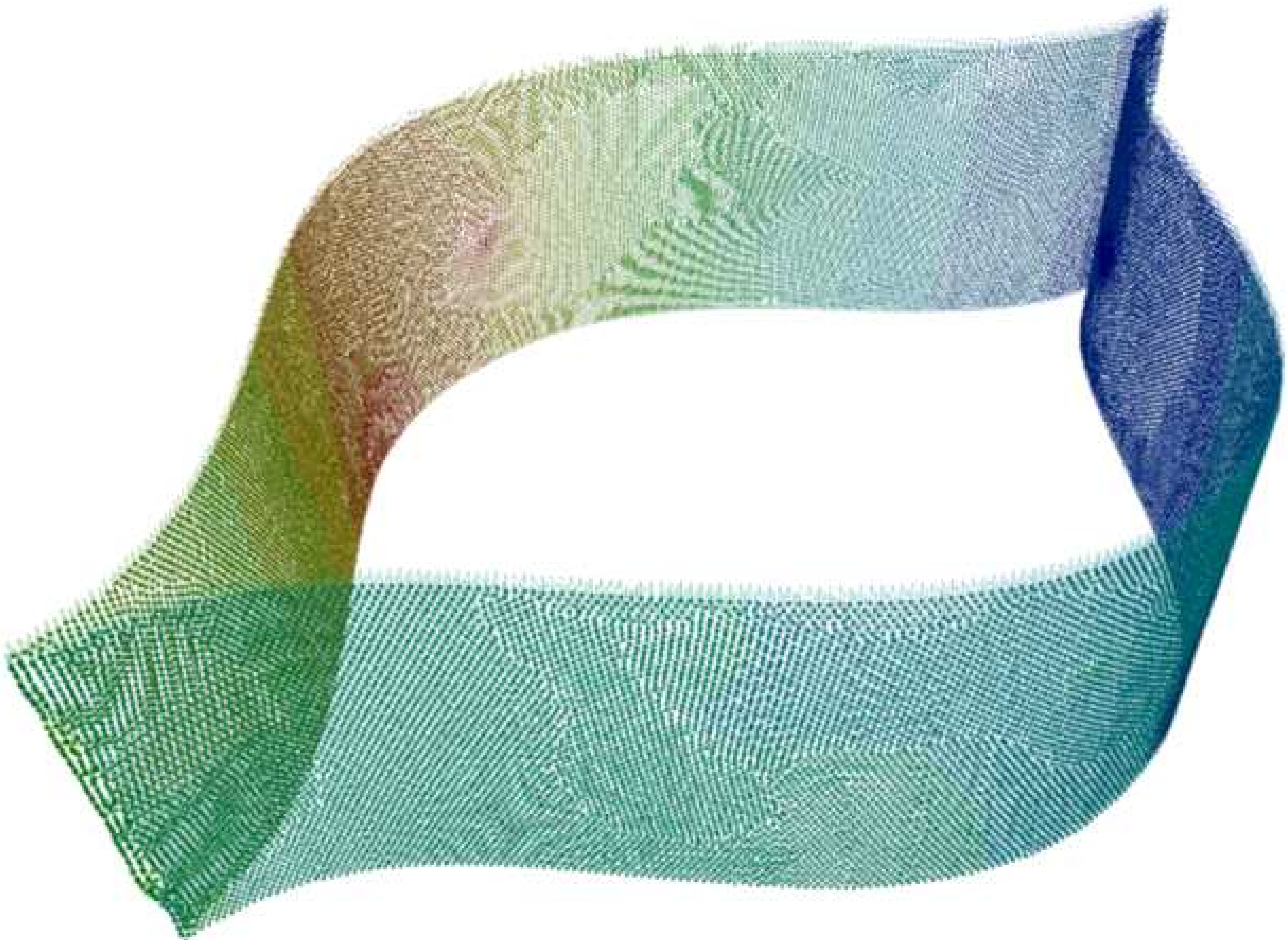

Avg. tensile strain: 8.8%

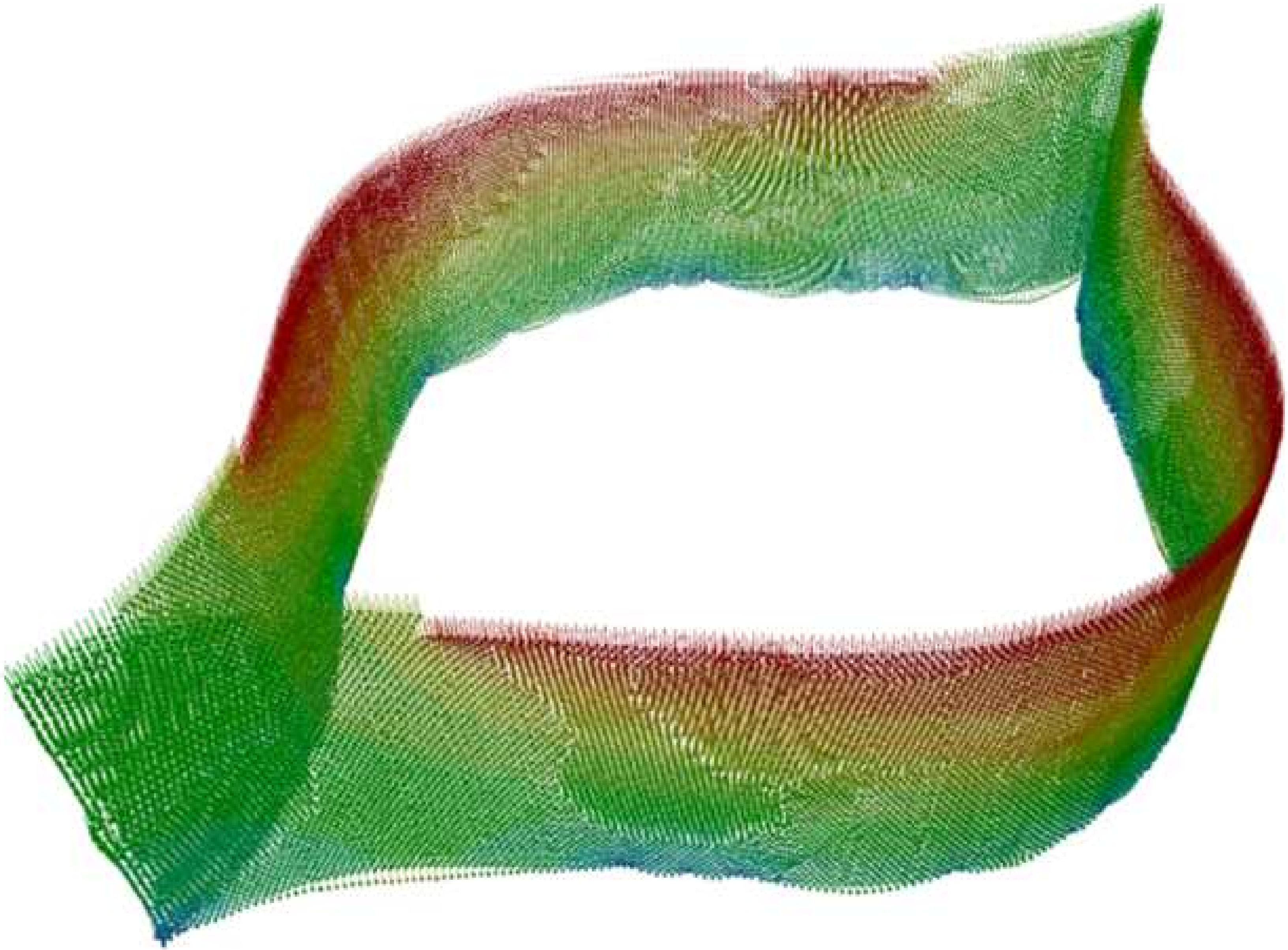

Avg. tensile strain: 12.6%

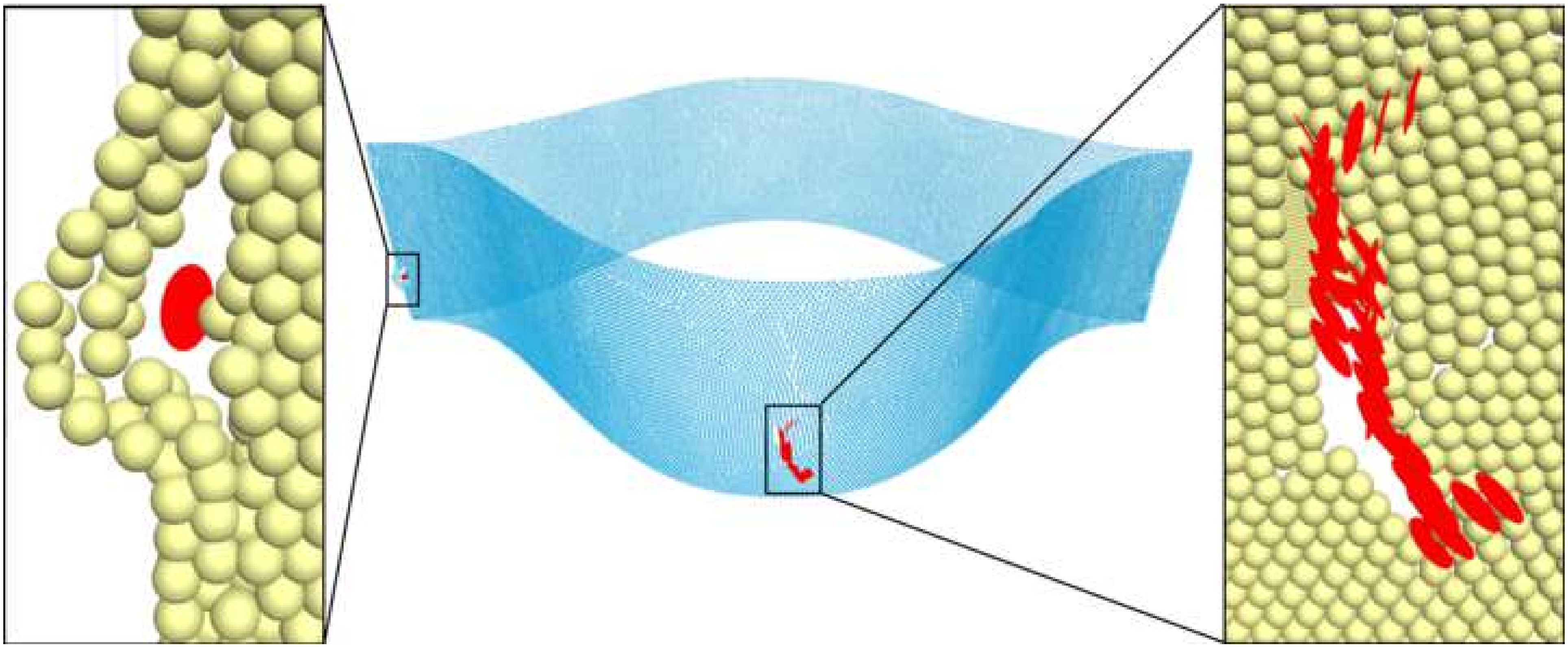

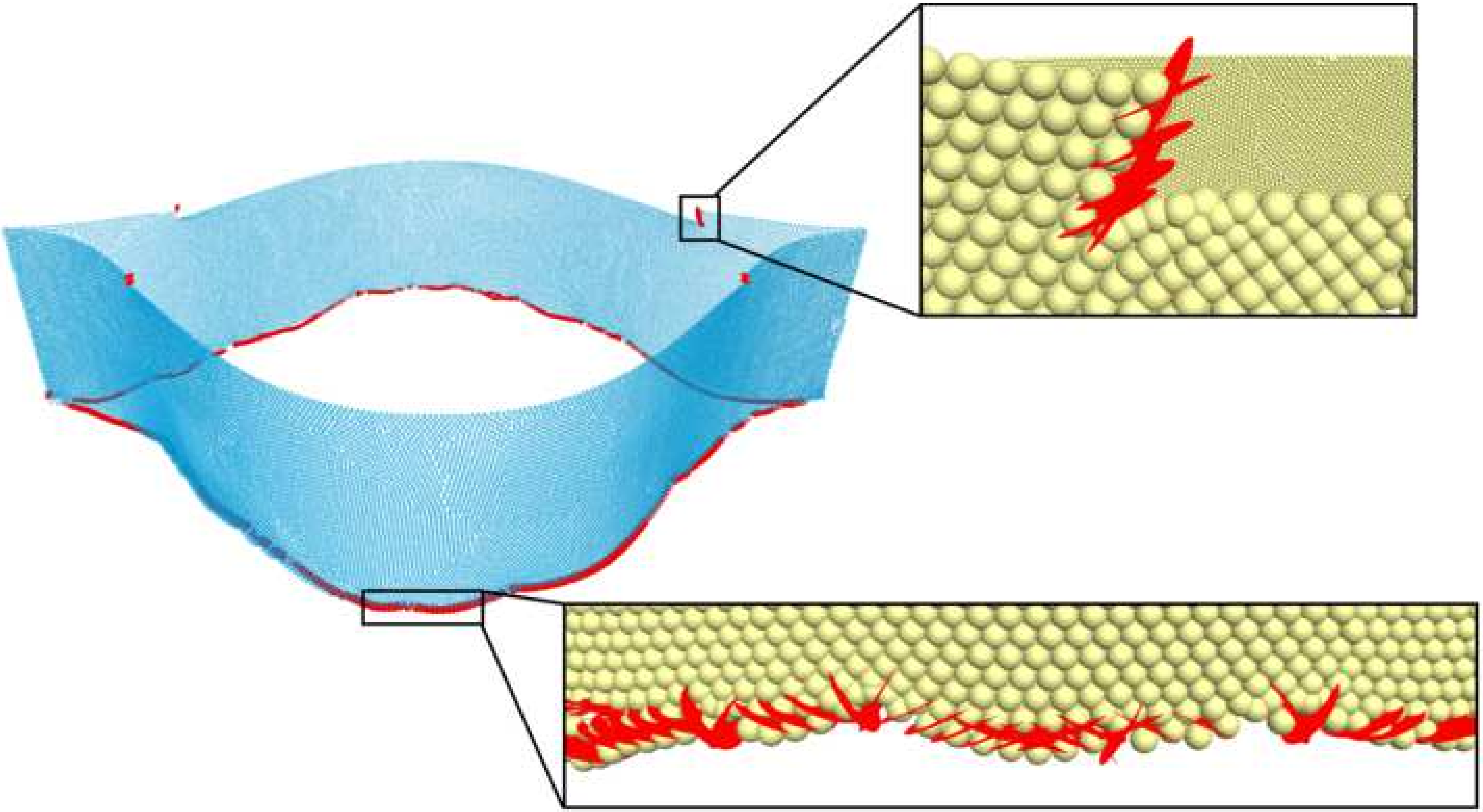

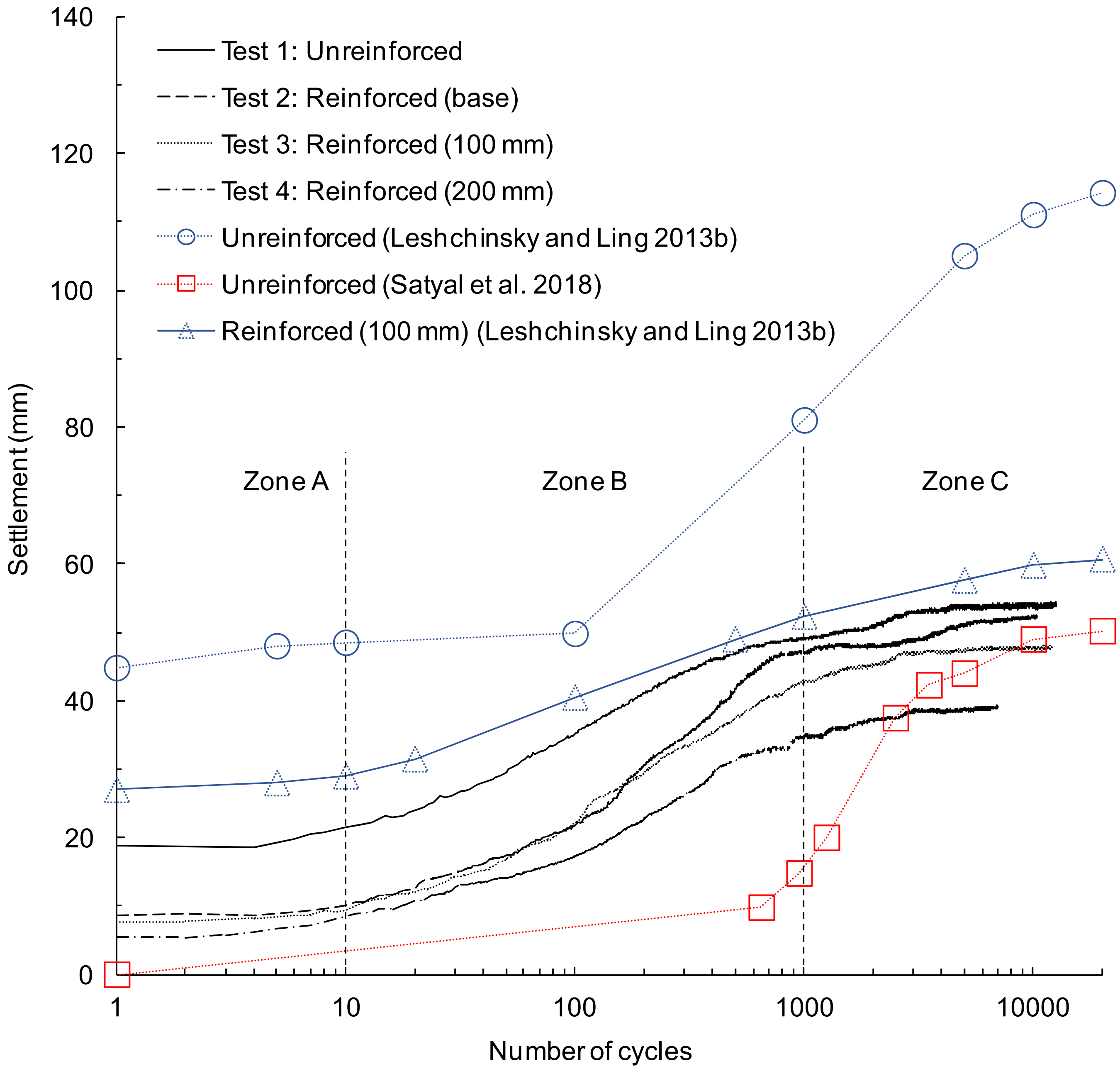

Settlement reduction
Zone A
Test 2: 53%
Test 3: 58%
Test 4: 65%
Zone B
Test 2: 28%
Test 3: 35%
Test 4: 44%
Zone C
Test 2: 3%
Test 3: 12%
Test 4: 27%

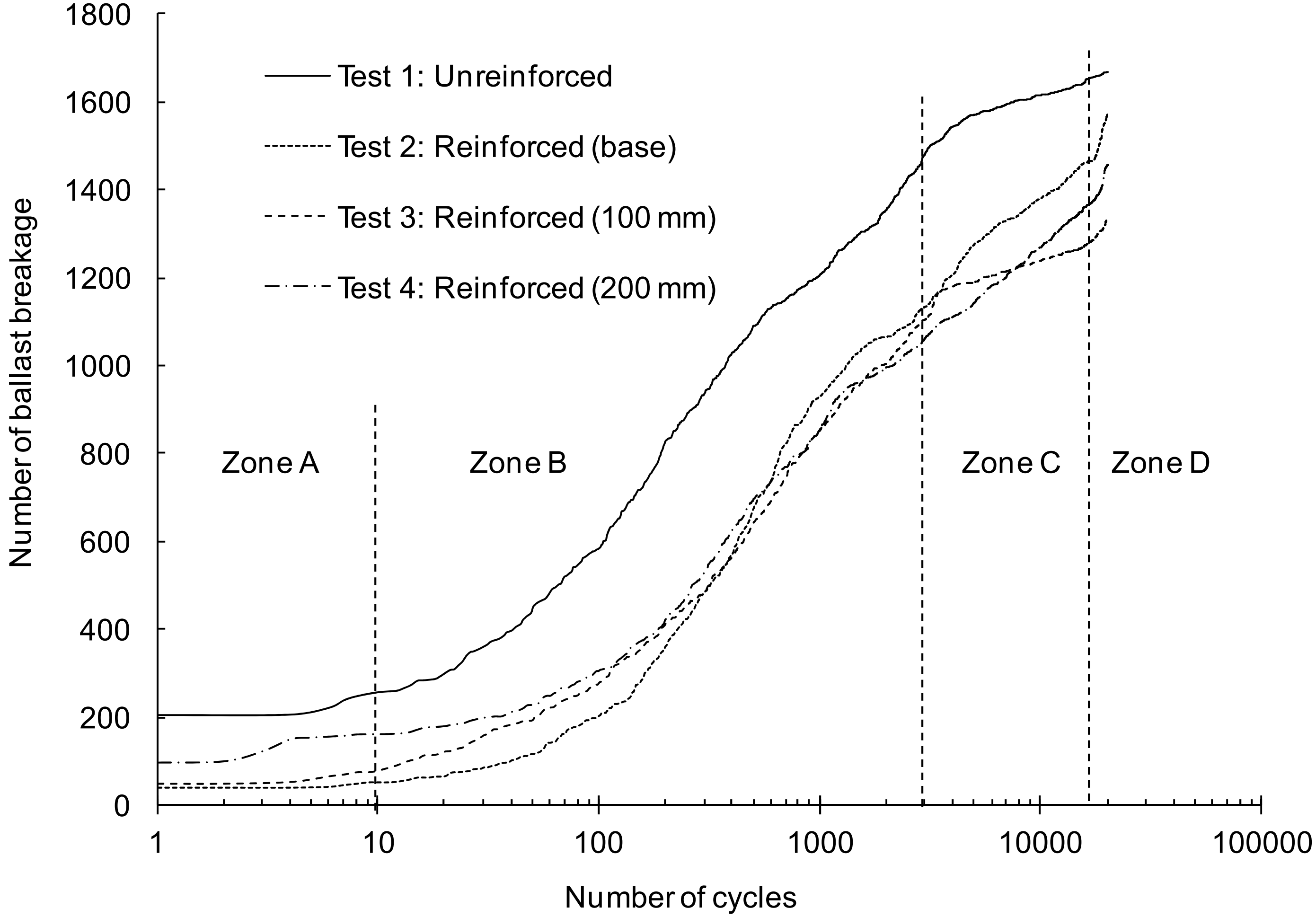

Number of ballast breakage
Number of cycles
0
200
400
600
800
1000
1200
1400
1600
1800
1
10
100
1000
10000
100000
Test 1: Unreinforced
Test 2: Reinforced (base)
Test 3: Reinforced (100 mm)
Test 4: Reinforced (200 mm)
Zone A
Zone B
Zone C
Zone D

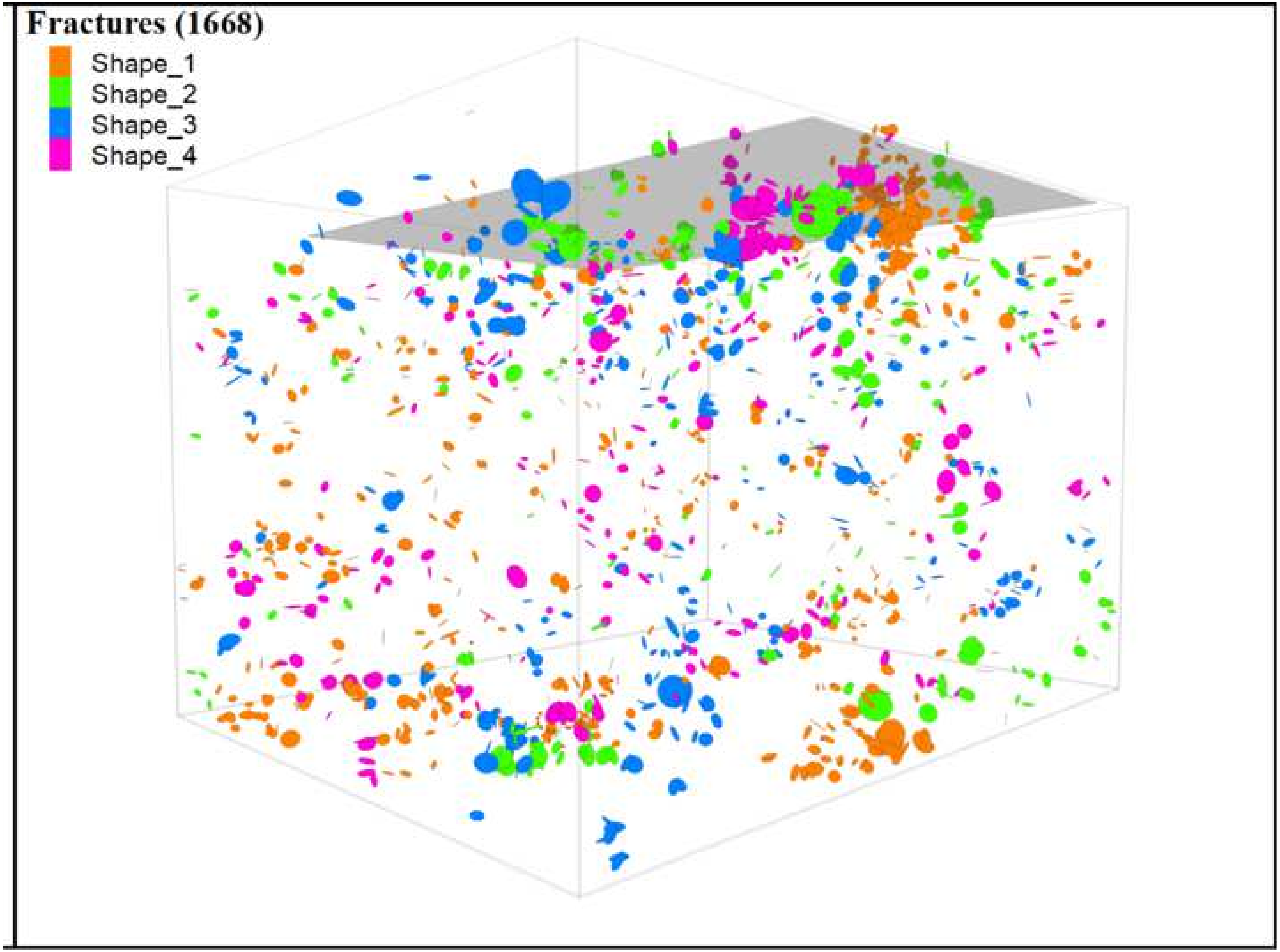
Fractures (1668)
Shape_1
Shape_2
Shape_3
Shape_4

Click here to access/download;Figure;Fig 24b.tiff

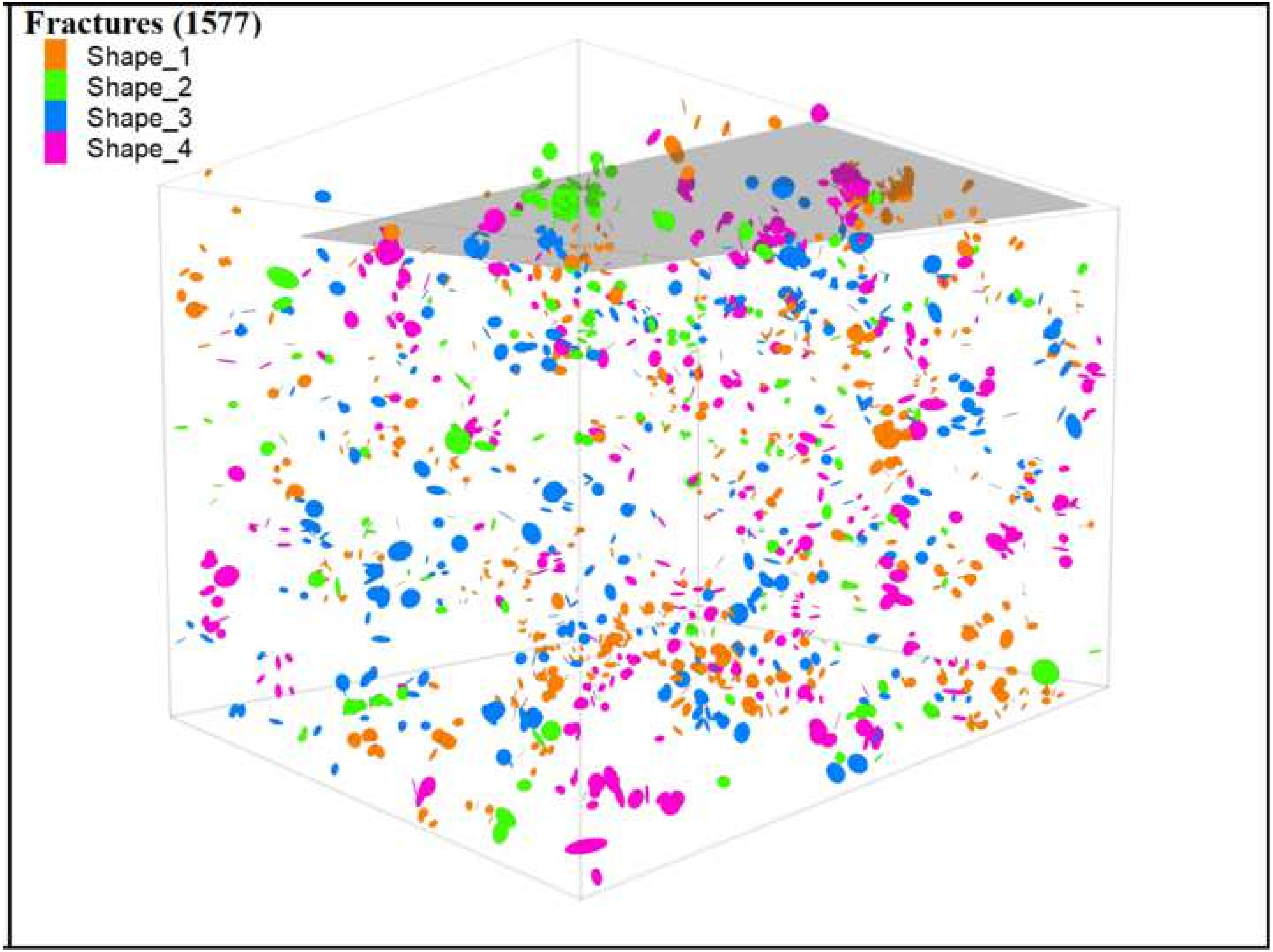

Click here to access/download;Figure;Fig 24c.tiff

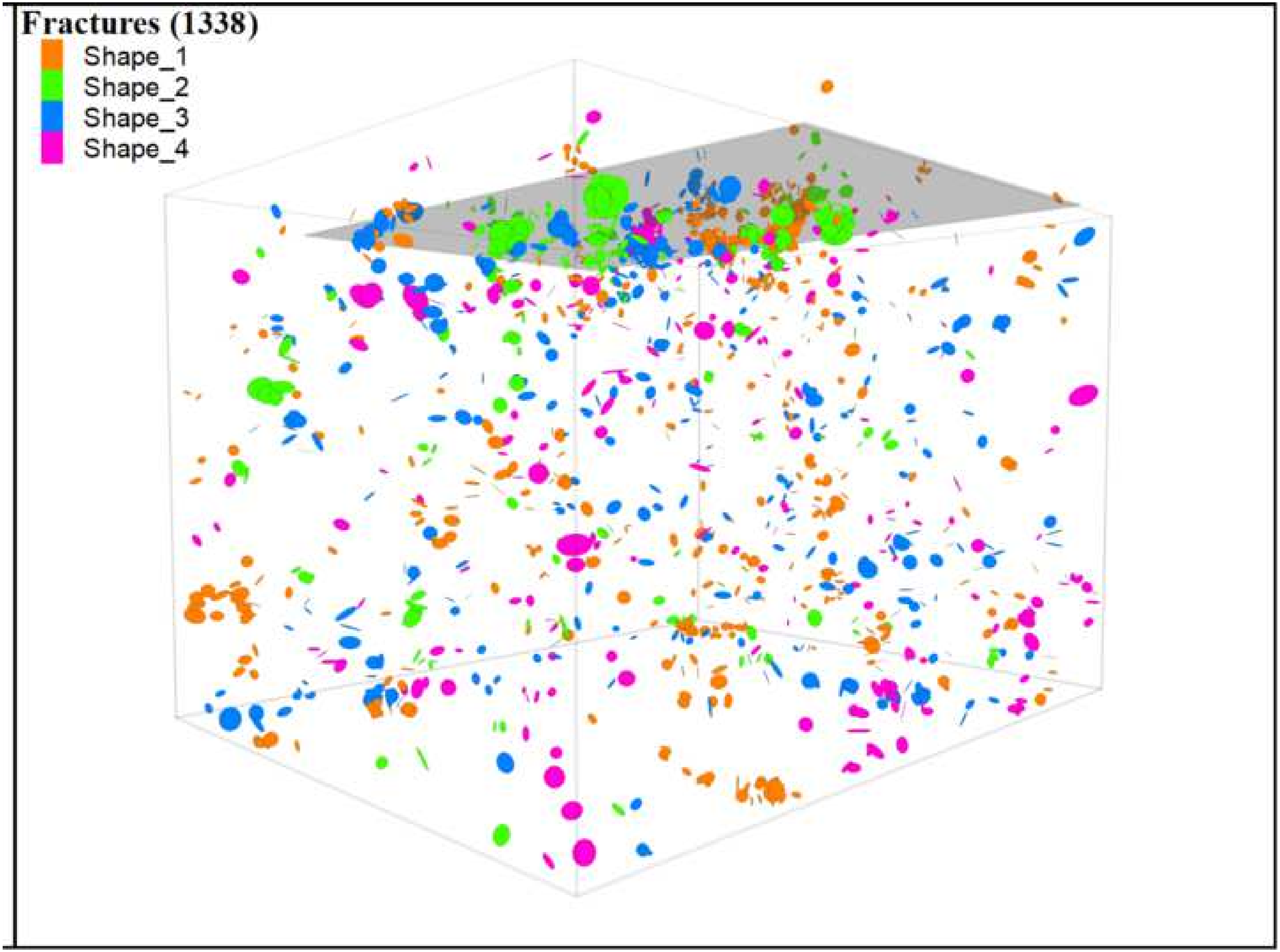

Click here to access/download;Figure;Fig 24d.tiff

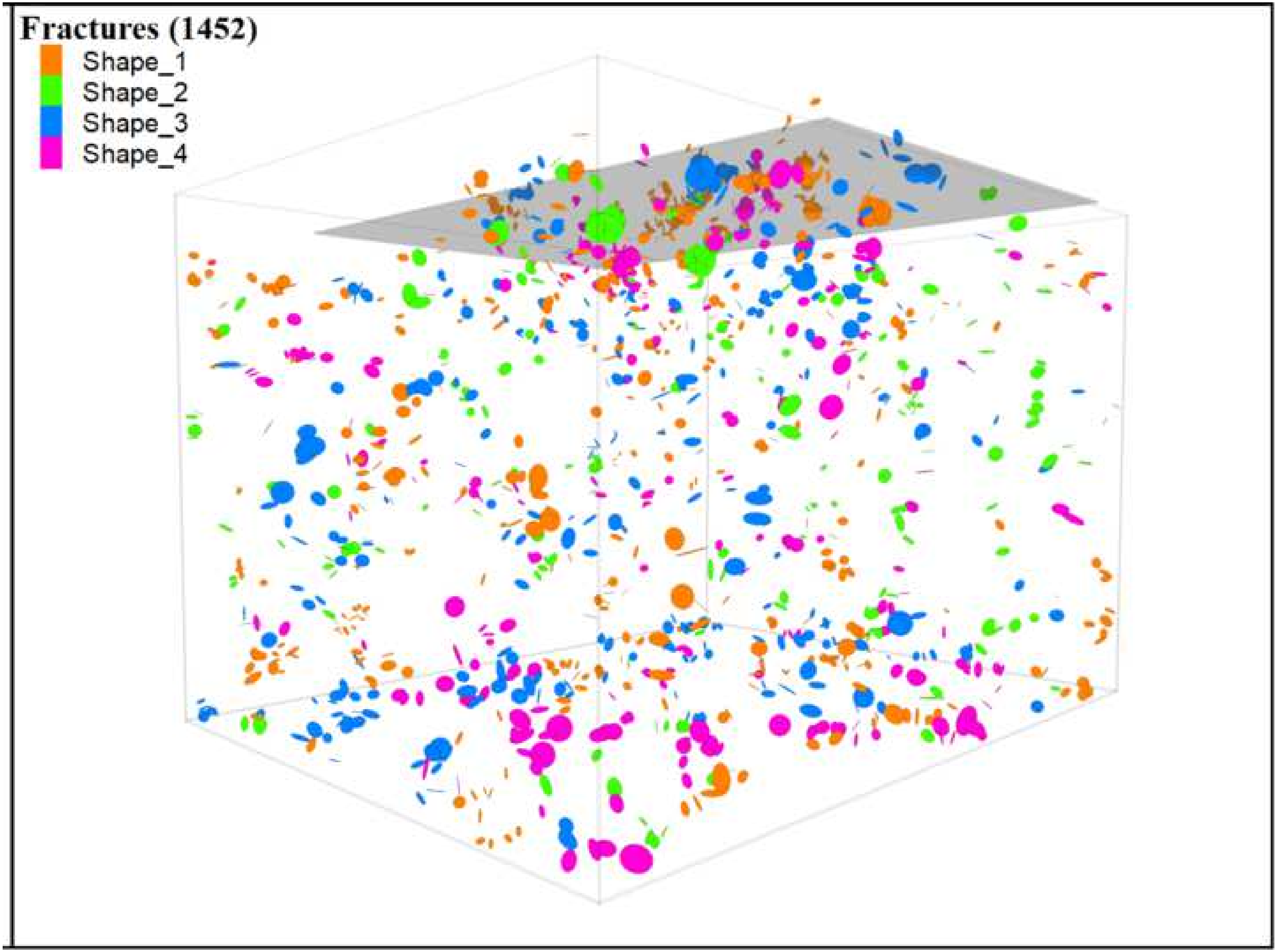

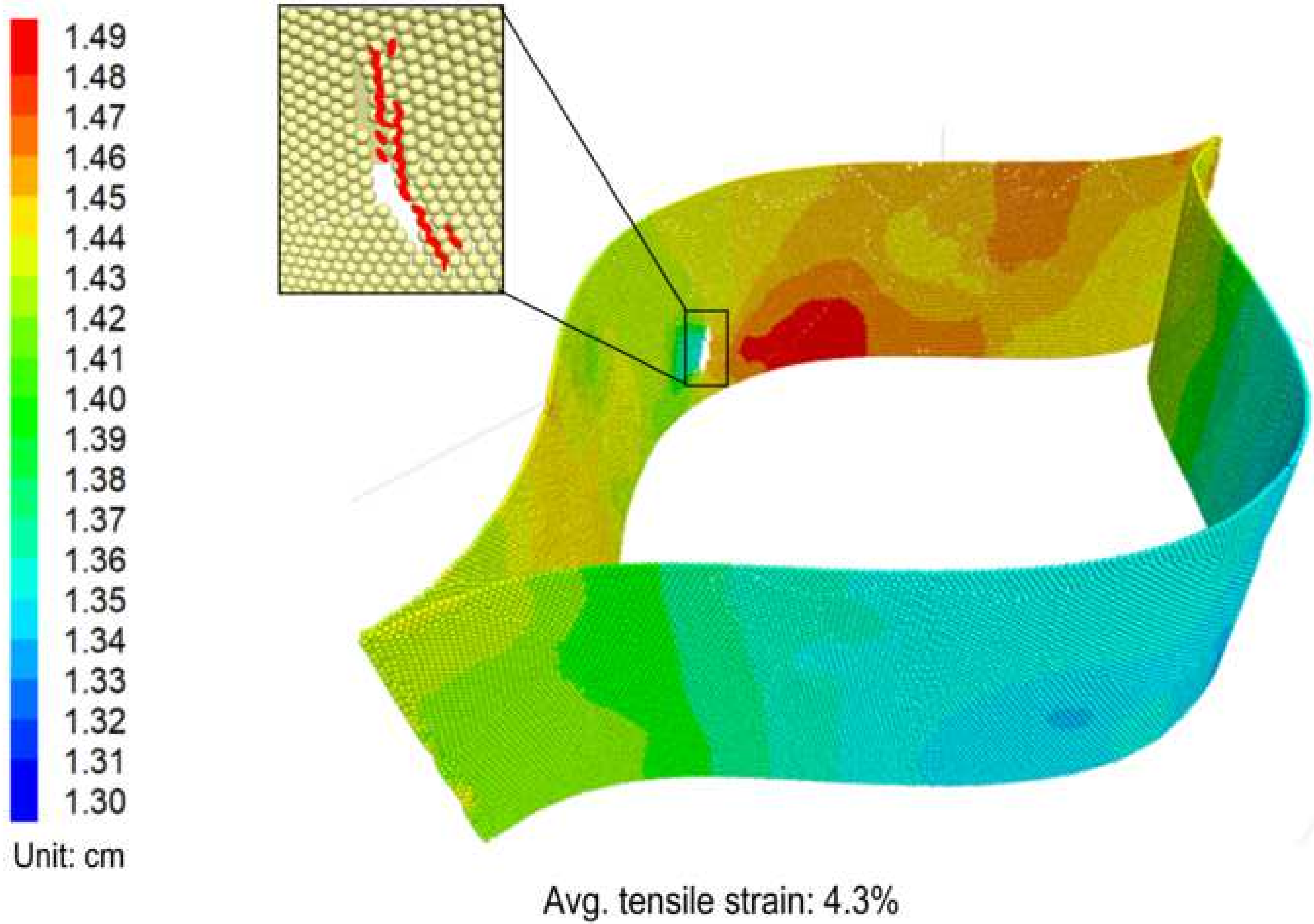
1.49
1.48
1.47
1.46
1.45
1.44
1.43
1.42
1.41
1.40
1.39
1.38
1.37
1.36
1.35
1.34
1.33
1.32
1.31
1.30
Unit: cm
Avg. tensile strain: 4.3%

Avg. tensile strain: 5.1%

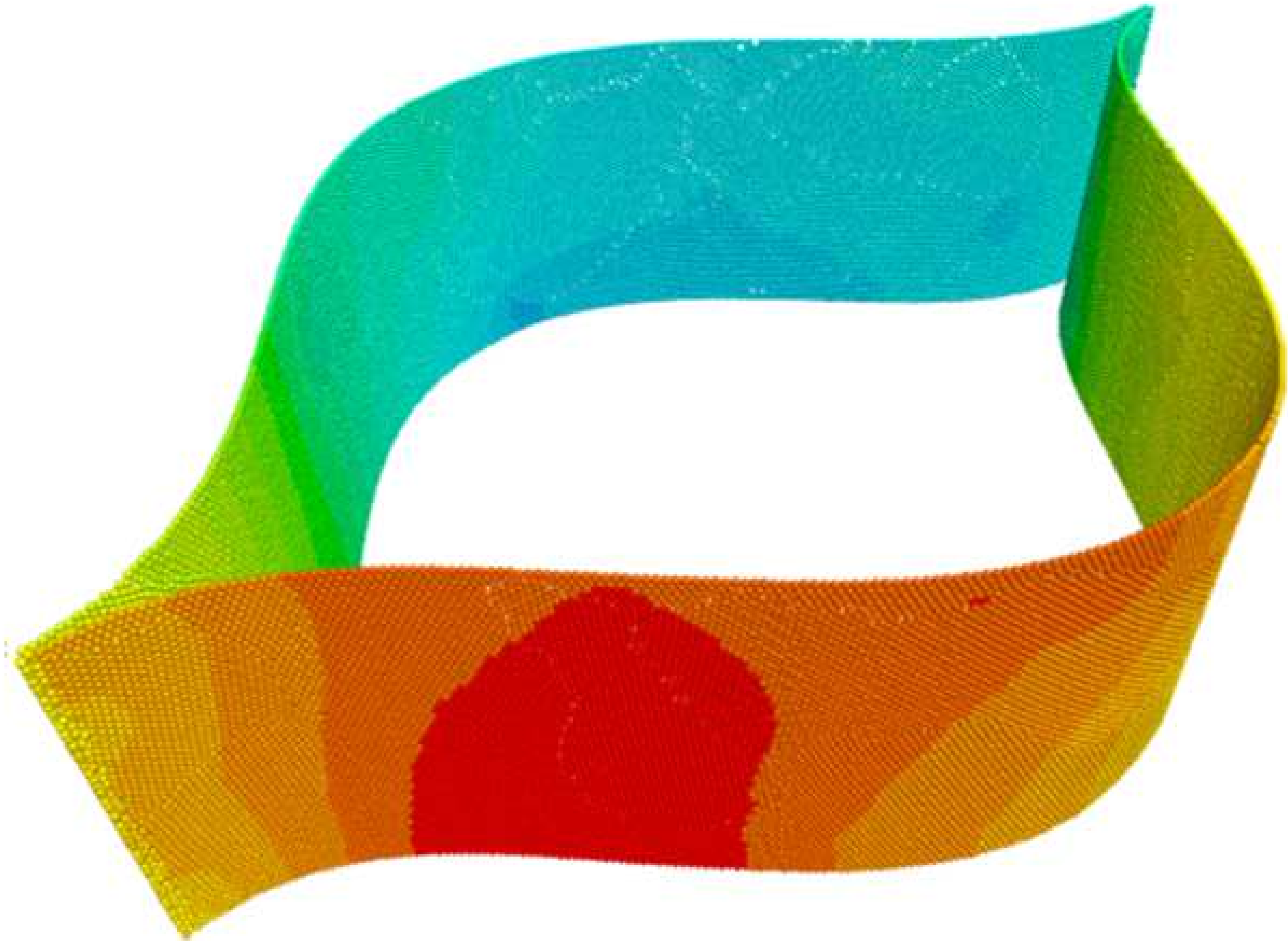

Avg. tensile strain: 6.2%

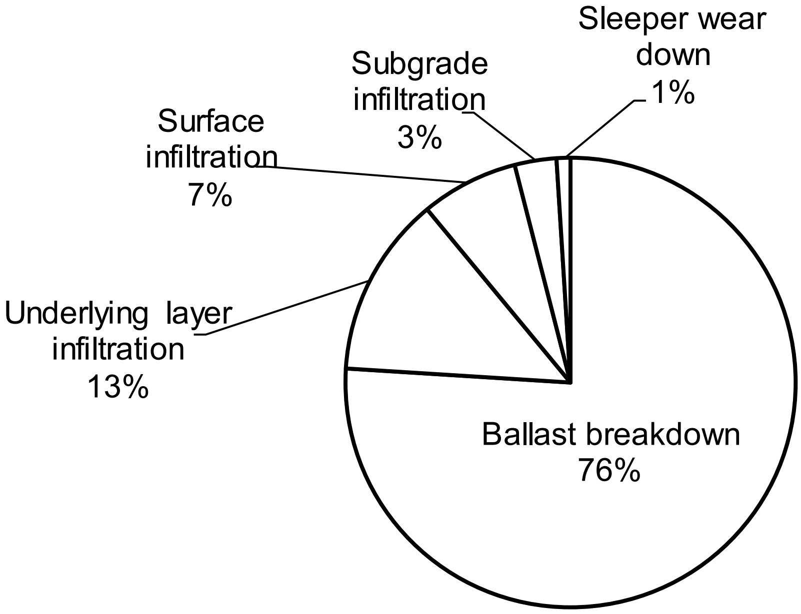
Sleeper wear down 1%
Subgrade infiltration 3%
Surface infiltration 7%
Underlying layer infiltration 13%
Ballast breakdown 76%

Fig. 1 Ballast shapes used in DEM simulation

Fig. 2. Sources of ballast fouling [adapted from Selig and Waters (1994)]

Fig. 3. Illustration of contact models: (a) linear contact model, (b) linear parallel-bond contact model [Adapted from Itasca (2009)]

Fig. 4. Particle size distribution of ballast assemblies in DEM simulation

Fig. 5. DEM model generation: (a) plan view of geocell pocket, (b) geocell-reinforced ballast model, (c) illustration of embedded and ballast filled geocell pocket

Fig. 6. Unconfined compressive strength test: (a) test setup, (b) trimmed specimen

Fig. 7. UCS modeling: (a) DEM model, (b) stress–strain relationship of test and simulation results

Fig. 8. Point load test: (a) laboratory test setup, (b) simulation setup illustration

Fig. 9. Schematics of the cell-wall and junction specimens and test setups: (a) cell-wall specimen, (b) cell-wall UTS test setup, (c) junction specimen, and (d) junction SS test setup

Fig. 10. DEM simulation of the UTS test for the cell-wall and junction specimens: (a) cell-wall specimen loaded by moving top loading spheres, and (b) junction specimen loaded by moving top loading spheres

Fig. 11. Calibration results of cell-wall and junction models: (a) cell-wall in the UTS test, and (b) junction in the SS test

Fig. 12. Ballast chamber model in the DEM simulation: (a) cross-sectional view, and (b) plan view.

Fig. 13. Ballast chamber models: (a) Test 1: unreinforced, (b) Test 2: reinforced model with geocell placed on the base, (c) Test 3: reinforced model with geocell placed 100 mm above the base, and (d) Test 4: reinforced model with geocell placed 200 mm above the base

Fig. 14. Contact pressure distribution between sleeper and ballast.

Fig. 15. Applied axial stress versus stress relationships of all model tests under monotonic loading

Fig. 16. Displacement vectors, drawn at the same scale, for ballast beneath the sleeper subjected to monotonic loading for different model tests: (a) Test 1: unreinforced, (b) Test 2: geocell on the base, (c) Test 2: enlarged view of the left-hand-side bottom displacement vectors, (d) Test 3: geocell placed 100 mm above the base, and (e) Test 4: geocell placed 200 mm above the base

Fig. 17. Number of ballast particle breakages versus settlement of all model tests under monotonic loading

Fig. 18. Contact force distribution on a cross-section beneath the sleeper centre: (a) Test 1: geocell unreinforced, (b) Test 2: geocell on the base, (d) Test 3: geocell placed 100 mm above the base, and (d) Test 4: geocell placed 200 mm above the base

Fig. 19. Distribution of ballast breakage under monotonic loading: (a) Test 1: unreinforced, (b) Test 2: geocell on the base, (d) Test 3: geocell placed 100 mm above the base, and (d) Test 4: geocell placed 200 mm above the base

Fig. 20. Deformation and displacement of geocell pocket under monotonic loading: (a) Test 2: geocell on the base, (b) Test 3: geocell placed 100 mm above the base, and (c) Test 4: geocell placed 200 mm above the base

Fig. 21. Locations of geocell rupture: (a) Test 2: geocell on the base, and (b) Test 4: geocell placed 200 mm above the base

Fig. 22. Settlement versus number of cycles relationships: (a) Test 1: unreinforced, (b) Test 2: geocell on the base, (d) Test 3: geocell placed 100 mm above the base, and (d) Test 4: geocell placed 200 mm above the base

Fig. 23. Number of breakages versus number of cycles.

Fig. 24. Distribution of ballast breakage under cyclic loading: (a) Test 1: unreinforced, (b) Test 2: geocell on the base, (d) Test 3: geocell placed 100 mm above the base, and (d) Test 4: geocell placed 200 mm above the base

Fig. 25. Geocell displacement and deformation contours under cyclic loading drawn at the same scale: (a) Test 1: unreinforced, (b) Test 2: geocell on the base, (d) Test 3: geocell placed 100 mm above the base, and (d) Test 4: geocell placed 200 mm above the base